AN ABSTRACT OF THE THESIS OF

Shiwei Zhao for the degree of Doctor of Philosophy in
Electrical and Computer Engineering presented on June 7, 2006.
Title: Pulsed Ultra-Wideband: Transmission, Detection, and Performance

Abstract approved: _____
Huaping Liu

Ultra-wideband (UWB) communication has emerged as a very promising technology for short-range wireless applications, including high-speed multimedia transmissions and sensor networks. UWB system designs involve many different aspects covering analog and digital processing, channel estimation and modeling, and modulation and demodulation. Although UWB still faces many challenges, significant progress has been made to commercialize UWB systems. This thesis focus on schemes to improve the performance and to lower the complexity of the UWB physical layer.

We first propose a frequency-hopped multi-band UWB system structure for higher throughput with better inter-symbol interference (ISI) immunity. This system is analyzed and compared to a single-band system. Pulse overlapping causes inter-pulse interference and may limit the system performance, especially in dense multipath environments. We then build a mathematical model with pulse overlapping considered and investigate the optimum linear RAKE receiver structure in such situation. The analysis is further is extended to systems that employ a prerake diversity combining scheme, in more realistic channel environments. The prerake scheme shifts RAKE receivers' related signal processing needs to the transmitter side and helps combat narrow-band interference.

To lower complexity, we develop a decision-directed autocorrelation (DDA) receiver, which offers more effective multipath energy capture at a lower complexity than the conventional RAKE receiver structures. Compared with transmit-reference receivers, the proposed DDA methods can considerably lower the noise level in the self-derived template waveform by operating in an adaptive decision-directed mode, thus improving the overall detection performance. There is little loss in energy efficiency since no reference pilots are required during adaptation.

Finally, we propose a hybrid modulation method that enables a heterogeneous network structure where users can flexibly choose a coherent RAKE receiver or a transmit-reference receiver structure. While neither type of receiver sacrifices performance loss by enabling the heterogeneous structure, the coherent RAKE receivers enjoy great performance advantages when further combined with forward error correction and iterative decoding methods.

Throughout the thesis, theoretical performance analysis is always presented along with corroborating simulations.

Pulsed Ultra-Wideband: Transmission, Detection, and Performance

by

Shiwei Zhao

A THESIS

submitted to

Oregon State University

in partial fulfillment of
the requirements for the
degree of

Doctor of Philosophy

Presented June 7, 2006
Commencement June 2007

Doctor of Philosophy thesis of Shiwei Zhao presented on June 7, 2006

APPROVED:

Major Professor, representing Electrical and Computer Engineering

---

Director of the School of Electrical Engineering and Computer Science

---

Dean of the Graduate School

I understand that my thesis will become part of the permanent collection of Oregon State University libraries. My signature below authorizes release of my thesis to any reader upon request.

Shiwei Zhao, Author

ACKNOWLEDGMENTS

When I first started my Ph.D journey four years ago, I was like a baby with a piece of white paper. The only thing I have in my hand is a pen. I started learning, drawing, and making tracks on my own map. Today, the roadmap is almost complete, and I hope it could be useful for other travelers, who may already have started their trips or will be on the way to their Ph.Ds soon. There are frustrations during the journey, but the path finally led to some new and useful discoveries, which motivate me to keep up on the journey over the years. Many individuals have played important roles during my journey and have extended me a helping hand when I was about to fall. I cannot make it without the help and support from these people.

First of all, I would like to express my sincere gratitude to my advisor, Prof. Huaping Liu who led me to this field and inspired my interest, for his support and inviable trust on my capabilities, especially at the difficult times. All the encouraging words will be always remembered in my heart. I am also very grateful to Dr Liu's pieces of advices and suggestions on my research and thesis. Without him, the goal could not have been achieved today.

I want to give my special thanks to the researchers we collaborated with, Prof. Zhi Tian, Dr. Shaomin Mo, Dr. Philip Orlik, Dr. Andreas F. Molisch, and Dr. Jinyun Zhang. I also want to express my appreciation for the time and advices from the professors on my Ph.D committee, Prof. David McIntyre, Prof. Larry Marple, Prof. Mario E. Magaña, and Prof. Luca Lucchese.

I gratefully acknowledge my former and present colleagues at the wireless communications group at OSU for creating such a pleasant research environment and for helping me on many research and technical problems. These include Yu Zhang, Liang Xian, Jie Gao, Orhan C. Ozdural, and more than I can name. I have always been in-

spired and impressed by their hard work and novel ideas. My appreciation also goes to the friends I met at Oregon State University. Thank you for sharing the wonderful time with me during these years.

I also owe my thanks to my dear parents, who gave me a great education and taught me positive attitudes. Your patience, encouragement, and support will always be in my heart.

Finally, but not the least, I would like to express my deepest gratitude and appreciation to my wife Yunzhu for her love and support; without her, I could not have successfully completed this dissertation.

To all of them, I express my sincere thanks!

TABLE OF CONTENTS

TABLE OF CONTENTS (Continued)

Page

TABLE OF CONTENTS (Continued)

Page

TABLE OF CONTENTS (Continued)

Page

LIST OF FIGURES

Figure Page

LIST OF TABLES

USED NOTATIONS, SYMBOLS, AND ACRONYMS

In this thesis, scalar variables are written as plain lower-case letters, vectors as bold-face lower-case letters, and matrices as bold-face upper-case letters. Some further used notations and commonly used acronyms are listed in the following:

$E\{\cdot\}$	Statistical expectation of a random variable
$\lvert\cdot\rvert$	Absolute magnitude
$\{\cdot\}^*$	Complex conjugate
$\{\cdot\}^T$	Transpose
$\{\cdot\}^H$	Hermitian transpose
$\lfloor\cdot\rfloor$	The integer part of a number
$\delta(\cdot)$	Dirac delta function
$Q(\cdot)$	The complementary error function
AWGN	Additive white Gaussian noise
BER	Bit error rate
CDMA	Code-division multiple-access
CSI	Channel state information
DS	Direct-sequence
EGC	Equal gain combining
EXIT	Extrinsic information transfer chart
FEC	Forward error correction
IPI	Inter-pulse interference
ISI	Inter-symbol interference
LOS	Line-of-sight

MAI	Multiple-access interference
MAP	Maximum *a posteriori* probability
ML	Maximum likelihood
MMSE	Minimum mean-square error
MRC	Maximal ratio combining
NBI	Narrowband interference
NLOS	Non-line-of-sight
PAM	Pulse-amplitude modulation
PPM	Pulse-position modulation
PSD	Power spectral density
PSK	Phase-shift keying
RMS	Root-mean-square
RRC	Root-raised-cosine
SISO	Soft-input soft-output
SIR	Signal-to-interference (power) ratio
SNR	Signal-to-noise (power) ratio
TH	Time-hopping
TR	Transmit-reference
UWB	Ultra-wideband
ZF	Zero-forcing

Pulsed Ultra-Wideband: Transmission, Detection, and Performance

1. INTRODUCTION

1.1. Background and Motivation

Ultra-wideband (UWB) communication has emerged as a very promising technology for short-range, high-speed wireless applications [1–6]. UWB signals have an instantaneous spectral bandwidth (10dB bandwidth) in excess of 500 MHz or a fractional bandwidth of more than 20% of its center frequency. Ultra-wideband signaling is commonly realized by transmitting very-short-duration pulses, often on the order of nanoseconds or less, whereby the occupied bandwidth goes to very large values. Such a large bandwidth allows it to deliver data rates in excess of 100 Mbit/s, while using a small amount of power and operating in the same bands as existing communications without causing significant interference.

UWB radios operate at extremely low transmitted power spectral density under Federal Communications Commission (FCC) spectral regulations, which open up a host of new wireless services capable of overlay with legacy narrowband systems. By conveying information over ultra-short pulses, pulsed UWB radios also provide very fine temporal resolution, which may lead to high-performance detector design when ample multipath diversity can be properly collected. UWB techniques may offer many potential merits including a simple radio that inherently leads to low-cost and low power design, covert operations, good immunity to narrow-band interference, large processing gain with fine multipath resolution, and fine time resolution for accurate position sensing.

UWB technology offers great opportunities for short-range wireless multimedia networking. The potential applications of UWB will not be, however, restricted to

high-quality multimedia. For example, its high-speed capabilities enable device synchronization via wireless, keeping one's contacts, calendars, music, and movies all in sync so quickly that users might not even realize that their contents are actually from separate devices. However, UWB receiver design also faces a number of challenges, such as multipath energy capture, inter-symbol interference, and the need for high-sampling-rate analog-to-digital converters.

Although often considered a recent breakthrough in wireless communications, UWB has actually experienced over 40 years of technological development. Due to technical limitations, narrow-band communications was preferred over UWB. Similar to spread spectrum or code-division multiple access (CDMA) systems, early UWB deployments were mainly for military covert radar and communication systems. In 1990, the U.S. Department of Defense (DoD) coined the term "ultra-wideband" for devices occupying at least 1.5 GHz or a -20 dB fractional bandwidth exceeding 25% [7]. After some of the research activities were unclassified in 1998 [1, 8], the research and development accelerated, though still was not very motivated due to the absence of a permit by spectrum regulatory authorities.

Announced in February 2002 and released in April of the same year [9], the US FCC (Federal Communications Commission) allowed the use of UWB systems for both indoor and outdoor communications in the 3.1-10.6 GHz band if certain restrictions with respect to bandwidth and spectral density are fulfilled [9]. Specifically, the UWB requirements mandated by the FCC are the fulfillment of a spectral mask that allows emission with a power of at most -41.3 dBm/MHz and transmission bandwidth of at least 500 MHz. This very low limit on power levels is to allow UWB wireless transmissions to overlay legacy narrowband services such as the IEEE 802.11 WLAN systems to coexist in the 3.1-10.6 GHz band. The FCC assigned emission limits on bandwidth and spectral mask are illustrated in Fig. 1.1 for indoor UWB systems and

outdoor UWB hand-held devices. Although currently the United States is the only country which permits commercial operation of UWB devices, regulatory efforts are underway both in Europe and in Japan.

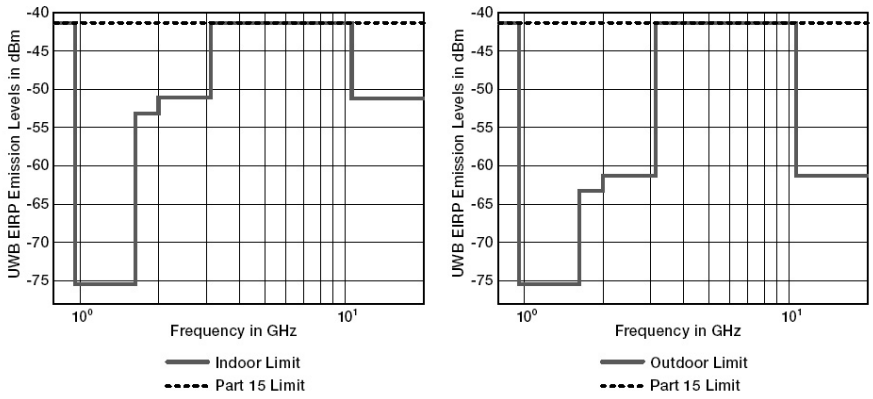

FIGURE 1.1. FCC regulated spectral mask for indoor and outdoor UWB systems.

The main limiting factor of UWB wireless systems is power spectral density rather than bandwidth. Thus, the initially targeted applications are very high data rates ($\geq$ 110 Mbps) over short distances (in the order of 10-20 meters), being standardized within the IEEE 802.15.3a Working Group (WG) for wireless personal area networks (WPAN) (also known as in-home networks). Due to implementation limitations to deliver high data rates and also its advantage on accurate ranging and ultra-low power hardware, UWB systems with moderate range (100-300m), low data rates (less than a few Mbps), but accurate locating capability (about 1m accuracy) have received significant attention since 2003 for wireless sensor networks [10], and is adopted in the baseline draft of IEEE 802.15.4a standards. In addition, UWB applications should also include safety/health monitoring, medical imaging, industrial inventory/process control/maintenance (including Radio Frequency Identification (RFID)), vehicular radar, etc.

1.2. Current Research and Challenges

Most of the published research to date on UWB has focused on single-band systems. The commonly used signaling scheme in a single-band UWB system employs short-duration, low-duty-cycle pulses to transmit information. The multi-band UWB concept has been introduced in more recent proposals [24–26]. The basic idea of the multi-band approach is to divide the 7.5GHz (3.1-10.6GHz) unlicensed UWB spectrum set by the FCC [9] into multiple sub-bands[1]. The multi-band architecture is expected to provide a more flexible and scalable usage of the spectrum, thus mitigating co-existence (e.g., with 802.11a) and many implementation issues. The achievable maximum data rate in a single-band UWB system is determined by the channel multipath delay that may cause inter-symbol interference (ISI). Given the same amount of bandwidth, a multi-band system might provide a higher throughput than a single-band system.

One of the key challenges for impulse radio is the construction of low-cost receivers that work well in multipath environments. Optimal energy capture is obtained by a coherent RAKE receiver that has enough fingers to collect all resolvable multipath components (MPCs) [27, 28]. However, the number of MPCs could be over tens or even hundreds in typical indoor environments (see [19–21] and references therein), which imposes technical hurdles as well as implementation difficulties. Although simplified RAKE structures were proposed before, e.g. [29], channel estimation, multipath tracking, and multipath combining contribute to the overall complexity of coherent RAKE receivers.

---

[1]The minimum bandwidth is 500MHz each sub-band.

With a RAKE structure, hardware complexity, power consumption, and system cost scale up significantly with the number of paths combined, which should be avoided for portable or mobile units. Most UWB networks have fixed access points, and it is very desirable if the RAKE processes can be shifted from the mobile receivers to the transmitter at a fixed access point. As such a shift usually requires channel state information (CSI) in the transmitter, this technique is attractive for systems with time-division duplexing (TDD), where CSI can be easily obtained at both the transmitter and the receiver since both the uplink and the downlink of TDD systems operate in the same frequency band.

For TDD code-division multiple-access (CDMA) systems, a transmit precoding technique was investigated in [59]. This scheme suggests a prerake structure in which pre-delayed signal transmission is employed in the transmitter. This scheme was shown to have comparable performance to the common RAKE receiver. The prerake scheme has recently been applied to pulsed UWB systems [60], in which the ideal case that received adjacent paths are separated in time by at least one pulse width is assumed. This assumption might be acceptable for communications in line-of-sight (LOS) environments. In non-LOS indoor environments, however, it becomes inappropriate. Besides IPI due to pulse overlapping, co-existing narrow-band radios will interfere with UWB systems. The effects of narrowband interference (NBI) to UWB systems with RAKE reception have been analyzed extensively [64, 65]. Prerake systems are expected to function differently from the conventional RAKE receiver in the presence of NBI. Therefore, the conclusions made in existing research on prerake UWB systems need to be re-examined and some optimizations might help to improve performance when pulse overlapping and NBI are taken into consideration.

In order to capture a considerable portion of the signal energy scattered in multipath components, a conventional RAKE-based digital receiver not only has to sample

and operate at a minimum of hundreds of MHz to even multi-GHz clock rates, but also requires an impractically large number of RAKE fingers. Realizing optimal RAKE reception performance requires accurate channel and timing knowledge, which is quite challenging to obtain as the number of resolvable paths grows. Moreover, the received pulse shapes of resolvable multipath might be distorted differently due to diffraction, which make it suboptimal to use line-of-sight signal waveform as the correlation template in RAKE reception.

For these reasons, transmitted-reference (TR) (also known as autocorrelation) receivers have drawn significant attention in recent years [38, 41, 39, 40]. TR encodes the data in the phase difference of the two pulses of a pulse pair, and offers better multipath capture capability at much lower hardware complexity than RAKE receivers [2]. In a slow fading environment, TR collects multipath energy efficiently without requiring multipath tracking or channel estimation. Analog autocorrelation also alleviates the burden on A-D converters, thus lowering the power consumption by interface circuits in the UWB regime. Nevertheless, TR autocorrelators entail several drawbacks: the use of reference pulses increases transmission overhead and reduces data rate, which results in reduced transmission power efficiency; the bit-error-rate (BER) performance is limited by the noise term in the reference signal [38, 41]. To compare, coherent RAKE receivers should be able to perform better in most cases provided that quite a lot work is needed to overcome those challenges. On the other hand, TR receivers offer a promising alternative with low hardware complexity and cost, though it faces perfor-

---

[2]Note that the scheme is different from the differential modulation, where data are encoded in the phase difference between successive *symbols*. Differential modulation is not practical for low-data-rate UWB signals, due to the long duration of the required delays.

mance limitations and its own technical difficulty on analog delay lines. As research advances, it is possible that it can approach or even outperform RAKE receivers.

1.3. In this thesis

In Chapter 2, we review the basics involved in the physical layer research of UWB systems. Basic signaling, modulations, receiver structures, and its special channel characteristics are covered. In Chapter 3, we introduce a frequency-hopped, multi-band UWB signaling scheme. We derive its analytical error performance in indoor log-normal fading channels and provide simulation results to validate some of the analytical results. Performance comparison is made between a single-band and a multi-band system.

In impulse radio ultra-wideband systems, multipath delay may cause received pulses to overlap with each other. Such a pulse overlapping causes inter-pulse interference (IPI) which may, especially in dense multipath environments, severely limit the system performance. Existing research has assumed that the received adjacent pulses are separated in time. In Chapter 4, we build a mathematical model with pulse overlapping considered and derive an optimum minimum mean-square error (MMSE) receiver. A simpler RAKE receiver is to take samples for each received pulse and perform maximal ratio combining (MRC) by ignoring the IPI. We then show, by an analytical approach, that the optimum linear MMSE receiver performs exactly the same as the simpler MRC receiver.

The need for effective capture of multipath energy presents a key challenge to receiver design for pulsed ultra-wideband (UWB) systems operating in non-line-of-sight propagation environments. Conventional RAKE receivers can capture only a small fraction of the received signal energy under practical implementation constraints,

and have to deal with stringent synchronization and channel estimation requirements. Transmit-reference and autocorrelation receivers can effectively collect energy from all the received multipath components without explicit channel estimation, but the detection performance is limited by noise enhancement effects and the data rate drops by 50% because of pilot symbol overhead. In Chapter 5, we develop decision-directed autocorrelation (DDA) receivers for effective multipath energy capture at low complexity. Operating in an adaptive decision-directed mode, the proposed DDA methods can considerably lower the noise level in the self-derived template waveform, thus improving overall detection performance. There is little loss in energy efficiency since no reference pilots are required during adaptation. Analytical performance analysis along with corroborating simulations is performed to evaluate the error performance of the proposed receivers in indoor lognormal fading channels.

Chapter 6 considers signaling schemes for heterogeneous ultra-wideband communications networks that contain both coherent (rake) and transmitted-reference (TR) receivers. Users in a UWB network often have different quality of service (QoS) requirements. It is thus very desirable to enable a heterogeneous network structure, where users can flexibly choose the type of receiver sufficient to achieve their specific QoS targets while minimizing cost. While coherent receivers are capable of receiving TR signals, they do so with a 3 dB penalty, because they cannot make use of the energy invested into the reference pulse. We propose a new signaling scheme that avoids this drawback, by encoding redundant information on the reference pulse. The resulting scheme does not affect the operation of a TR receiver, while recovering the 3 dB penalty and furthermore providing an additional 1.7 dB gain to a coherent receiver. This can be explained by interpreting the scheme as a trellis-coded modulation. We also provide an alternative implementation that can be viewed as a *recursive* systematic convolutional encoder. Combining this version further with a simple FEC encoder results in a con-

catenated code that can be decoded iteratively, providing a BER of 10^{-3} at 2.8 dB SNR in AWGN. The convergence behavior of this iterative code is analyzed by using EXIT charts. The proposed signaling scheme is applicable not only to pulsed UWB systems, but also to narrowband or conventional spread spectrum systems.

In Chapter 7, we analyze the prerake diversity combining schemes for pulsed ultra-wideband (UWB) systems to shift signal processing needs from the receiver to the transmitter. We consider the more realistic case that received pulses carrying the same transmitted symbol could overlap with one another in optimizing the prerake scheme based on zero-forcing and eigenanalysis techniques. We show that in the presence of inter-pulse interference caused by pulse overlapping, the optimum prerake combining scheme in the sense of maximizing the received signal-to-noise ratio derived by using the eigenanalysis technique performs the same as a conventional rake with maximal ratio combining. Since for UWB systems it is important to consider the effects of narrow-band interference (NBI), we also analyze the different behaviors of prerake and rake schemes in the presence of in-band modulated or tone interferer.

This thesis is concluded in Chapter 8. Most of the contents presented in this thesis have been published or submitted for publication in [11–18]. The hybrid IR methods proposed in [15, 16] have been filed for patents.

2. OVERVIEW

2.1. Impulse Radio: How It Works

UWB transmission usually refers to impulse based waveforms that can be used with different modulation schemes. The transmitted signal consists of a train of very narrow pulses at baseband, normally on the order of a nanosecond (denoted as pulse width T_p). Each transmitted pulse is referred to as a *monocycle*. The information can be carried by the position or amplitude of the pulses. In general, narrower pulses in the time domain correspond to electromagnetic radiation of wider spectrum in the frequency domain. Thus, the baseband train of nanosecond impulses can have a frequency spectrum of several GHz.

2.1.1. Monocycle waveform

The frequency-domain spectral content of a UWB signal depends on the pulse waveform shape and the pulse width. To satisfy the UWB emission constraint specified in FCC regulation and, in the meantime, to increase the maximum allowable transmission power for wider range, the desired frequency spectrum of the monocycle waveform should be flat over a target bandwidth.

The most popular pulse waveforms referred in the literature include Gaussian pulses, the derivatives of Gaussian pulses, or a combination of several derivatives of different orders. An important feature of these monocycles is that they do not have a DC component so that carrier modulation is not necessary, which makes the radiation of the monocycles more efficient. Other reasons behind their popularity include (a) the smallest possible time-bandwidth product of 0.5 and (b) the readily available simple signal generator.

As multi-band UWB schemes begin to be attract attention, carrier-modulated root-raised cosine (RRC) pulses come into the scene. It offers the desired availability of mature and even cheaper generators. Its frequency spectrum can be very flat and very flexible to adjust (with different roll-off factors).

2.1.2. Modulation and multiple access

For pulsed UWB systems, the widely used forms of modulation schemes include pulse amplitude modulation (PAM), on-off keying (OOK), and pulse position modulation (PPM). In fact, PPM was almost exclusively adopted in the early development of UWB radios because negating ultra-short pulses was difficult to implement. Because the nature that UWB transmission is mainly power limited instead of spectrum limited, binary modulation is usually adopted. For binary PPM signaling, bit “1” is represented by a pulse without any delay and bit “0” by a pulse with delay τ relative to the time reference. The most commonly used PPM scheme is the orthogonal signaling scheme for which the UWB pulse shape is orthogonal to its time-shifted version.

Another modulation scheme that does not require pulse negation is OOK, where symbol “1” is represented by transmitting a pulse, and “0” by transmitting nothing. The OOK scheme is less attractive than PAM or PPM because of its inferior error performance. However, if receiver complexity is the main design concern, a simple energy detection scheme can be applied with OOK signaling, resulting in a receiver of lowest achievable complexity.

OOK and PPM signals have discrete spectral lines, which could cause severe interference to existing narrowband radios. Various techniques such as random dithering could be applied in PPM to smooth the spectrum.

As pulse negation became easier to implement, PAM attracted more attention. For binary PAM signaling, information bits modulate the pulse polarity. PAM and PPM schemes have similar performance. Because of the random polarities of the information symbols, the PAM scheme inherently offers smooth PSD when averaged over a number of symbol intervals.

For better data rate or error performance, biorthogonal signaling by combing orthogonal PPM with binary PAM as well as orthogonal waveform and block orthogonal modulation schemes have also been reported. Transmitted-reference system is another method employing innovative modulation and detection methods to compromise the performance with receiver complexity.

To allow for multi-user access to the UWB channel, mainly two methods have been applied: time-hopping (TH) and direct-sequence (DS). Since pulsed UWB systems are inherently spread spectrum systems, the use of spreading codes in DS-UWB systems is solely for accommodating multiple users.

In a typical UWB system, each information-conveying symbol is represented by a number of (N_f) pulses, each transmitted per frame of duration $T_f \gg T_p$ [1]. As the pulse duty cycle is very small, the transmitter is gated off for the bulk of a symbol period. Time-hopping can be implemented by employing appropriately chosen hopping sequences for different users to minimize the probability of collisions due to multiple access. In TH UWB, each frame is subdivided into N_c chips of duration T_p. Each user (indexed by k) is assigned a unique pseudo-random time shift pattern $\{h_{k,n}\}$, $0 \leq h_{k,n} < N_c$, called a TH sequence, which provides an additional time shift to each pulse in the pulse train. The n^{th} pulse undergoes an additional time shift of $h_{k,n}T_p$,

---

[1] Having N_f frames per symbol period reverses the commonly used terminology where a frame consists of multiple symbols (here multiple frames comprise a symbol).

where chip duration T_p is also the addressable time delay bin. With binary signaling, the transmitted TH PAM or PPM signal of the k^{th} user can be written in a general mathematical form as

$$s_k(t) = \sum_{n=-\infty}^{\infty} \sqrt{E_p} b_{k,n}^0 p(t - nT_f - h_{k,n}T_p - \tau(1 - b_{k,n}^1)) \tag{2.1}$$

where E_p is the transmitted energy per pulse. For TH PPM, $b_{k,p}^0$ is set to 1 and $b_{k,n}^1 \in \{0, 1\}$ carries information. For TH PAM, $b_{k,n}^1$ is set to 1 and $b_{k,n}^0 \in \{\pm 1\}$ carries information (in non-return-to-zero form).

Direct-sequence codes can also be used with both PAM and PPM modulation for multiple access. For binary signaling, the transmitted signal of the k^{th} user can be written as

$$s_k(t) = \sum_{n=-\infty}^{\infty} \sqrt{E_p} b_{k,n}^0 a_{k,n} p(t - nT_f - \tau(1 - b_{k,n}^1)) \tag{2.2}$$

The pseudo-noise (PN) sequence $a_{k,n}$ is used to identify the k^{th} user, which can be a long sequence period over multiple bits (symbols) or a short sequence over only one bit (symbol) (each bit or symbol contains multiple frames). Common characteristics of DS codes are assumed here.

2.2. Channel model

To accurately appreciate and evaluate UWB system designs, it is important to firstly understand the propagation characteristics of the ultra-short UWB waveforms and accurately model the channel statistics. Given the wideband nature of UWB transmissions, the conventional channel models developed for narrowband transmissions are not adequate anymore. Here we examine the channel model recommended by the IEEE 802.15.3a and 4a working group [19, 20], which is extracted from a large amount of measurements in different communication environments such as residential, office,

industry, and outdoor, covering the frequency range from 2GHz to 10GHz. We will focus on indoor channels since more than 80% of the envisioned commercial UWB applications will be indoor communications.

The channel for pulsed UWB systems exhibits highly frequency-selective fading and can be modeled as a discrete linear filter [19, 20] with an impulse response expressed as

$$h(t) = \sum_{l=0}^{L-1} \alpha_l \delta(t - \tau_l) \tag{2.3}$$

where L is the total number of resolvable multipath components, each with path fading gain α_l and delay τ_l relative to the first path, and $\delta(t)$ is the Dirac delta function. The approach suggested in [19] models the fading coefficient α_l in (5.2) as $\alpha_l = \lambda_l \beta_l$, where $\lambda_l \in \{1, -1\}$ with equal probability accounts for the random pulse inversion that could occur due to reflections. The magnitude term β_l is modeled as having a lognormal distribution for indoor channels [22, 32]. The standard deviation of fading amplitudes is typically in the range of 3-5dB. The RMS delay spread could be from several to half a hundred nanoseconds, and the maximum excess delay spread is usually 3 to 5 times the RMS delay spread for an exponential decay power delay profile model. Upon synchronization, the receiver can adjust its timing according to the estimated first arrival time τ_0. By assuming perfect timing, the multipath delays with respect to the adjusted receiver timing could be set as $\tau_0 = 0$.

The distribution of the path arrival time sequence τ_l and power delay profile [73] of the channel are chosen to follow the modified Saleh-Valenzuela (S-V) model suggested in [19]. Because multipath components tend to arrive in clusters [19], τ_l in (5.2) is expressed as $\tau_l = \mu_c + \nu_{m,c}$, where μ_c is the delay of the c^{th} cluster that the l^{th} path falls in, $\nu_{m,c}$ is delay (relative to μ_c) of the m^{th} multipath component in the c^{th} cluster. The relative power of the l^{th} path to the first path can be expressed as $E\{|\alpha_l|^2\} = E\{|\alpha_0|^2\} e^{-\mu_c/\Gamma} e^{-\nu_m/\gamma}$, where $E\{\cdot\}$ denotes statistical expectation, Γ is the

cluster decay factor, and γ is the ray decay factor. Note that, different from common baseband models of narrow-band systems, α_l is real-valued in the UWB channel model.

Since UWB is targeted mostly for high-rate communications in slowly fading indoor environments, the channel can be reasonably assumed to be constant over a number of bit intervals [19]. Throughout this thesis fading is assumed to be quasistatic, allowing all channel coefficients α_l and relative delays τ_l to be constant over a block of data and change independently from one block to another. For example, if the channel is static over a $100\mu s$ data burst period, as suggested in [19], the size of a quasistatic block is 1000 bits for a data rate of 40Mbps employing binary signaling.

2.3. Receiver techniques

The most common UWB receiver designs include threshold/energy detectors, transmit-reference (TR) receivers, and RAKE (correlation) receivers. The threshold/energy detectors are simple to implement, with tradeoff on performance, and suitable for UWB radar systems. Rake correlation receivers coherently detect the received signal and can achieve the optimal performance *in theory*. Most of early receiver research focused on RAKE type of receivers. Recently due to the difficulty and complexity from stringent timing synchronization requirement and energy capture of multipaths, suboptimal TR (also called autocorrelation) receivers start to attract significant attentions. Next we will look into the ideas of the RAKE and the TR receiver structures, and compare their advantages/disadvantages.

2.3.1. Rake receiver

It is well known that the optimum receiver for AWGN channels is a correlator (i.e. matched filter) receiver. The receiver locally generated monocycle waveform

would be perfectly synchronized and correlated with the incoming monocycle train, which is only distorted by AWGN noise.

Conveying information with ultra-short pulses, UWB transmissions can resolve many paths and are thus rich in multipath diversity. A RAKE receiver can be used to exploit the diversity by constructively combining the separable received multipath components. It is so named because of its analogous function to a garden rake, consisting of "sub-receivers" each delayed accordingly to tune into the individual multipath components. Each branch is a correlator (matched filter), coherently collecting received signal energy independently, and, at a later stage, is combined in order to make the most use of the different transmission characteristics of each transmission path. This could very well result in higher signal-to-noise ratio (SNR, also known as Eb/No) in a multipath environment.

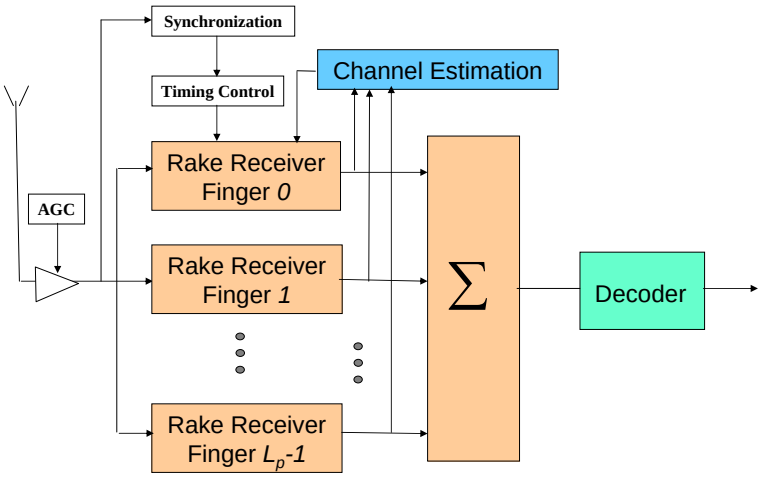

FIGURE 2.1. Block diagram of a typical RAKE receiver structure.

Fig. 2.1 shows the receiver block diagram, which consists of L_p correlators/fingers to collect the received signal energy from the L_p strongest paths having excess delays $\{\tau_l\}|_{l=0}^{L_p-1}$. The l^th correlator, $l = 0, 1, 2, ..., L_p - 1$, is to correlate the

received signal with the receiver locally generated reference signal delayed by τ_l. The output of the correlators can be linearly combined in different ways to form the decision variable. The maximal ratio combining (MRC) approach provides optimal performance, with the prerequisite of accurate channel information at the receiver. As accurate channel information are not available, equal gain combining (EGC) and some other methods could be choices.

2.3.2. Transmit-reference receiver

One of the key challenges for impulse radio is the construction of low-cost receivers that work well in multipath environments. From the previous section, we know that the coherent RAKE receiver offers optimal performance, relying on enough fingers to accurately capture all or a significant part of resolvable multipath components (MPCs) [27, 28]. However, a large discrepancy in performance exists between the implementations and the theoretically optimal receivers. In a pulse-based UWB system, the number of resolvable paths could reach tens to over a hundred in typical indoor propagation environments [19–21], which imposes technical hurdles as well as implementation difficulties. In order to capture a considerable portion of the signal energy scattered in multipath components, a conventional RAKE-based digital receiver not only has to sample and operate at a minimum of hundreds of MHz to even multi-GHz clock rates, but also requires an impractically large number of RAKE fingers. In addition, realizing optimal RAKE reception performance requires accurate channel and timing knowledge, which is quite challenging to obtain as the number of resolvable paths grows. The received pulse shapes of resolvable multipath are distorted differently due to diffraction, which make it suboptimal to use line-of-sight signal waveform as the correlation template in RAKE reception. Because of these issues unique to UWB

pulsed radios, an optimal RAKE receiver design becomes either ineffective or very complicated.

For these reasons, transmit-reference (TR) receivers (also called autocorrelation receivers) have drawn significant attention in recent years [38–42]. As a suboptimal, low-complexity alternative, TR receivers offer better multipath capture capability at much lower hardware complexity than RAKE receivers. TR encodes the data in the phase difference of the two pulses of a pulse pair. The first pulse in that pair does not carry information, but serves as a reference pulse; the second pulse is modulated by the data and is referred to as the data pulse. The two pulses are separated by a fixed delay. It can be easily shown that the receiver can demodulate this signal by simply multiplying the received signal with a delayed version of itself[2]. The simple TR transceiver structure is shown by the block diagram in Fig. 2.2.

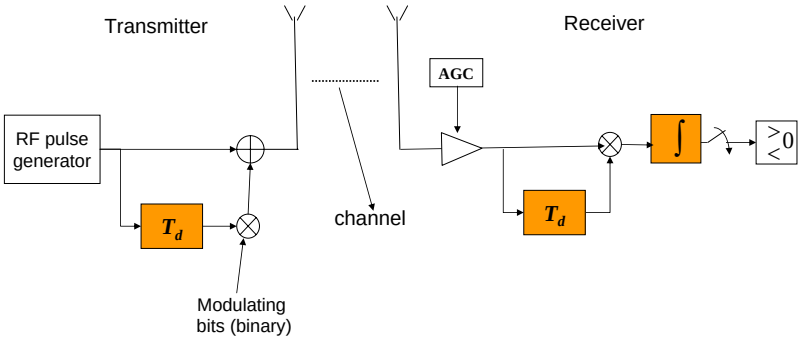

FIGURE 2.2. Block diagram of a transmit-reference system.

[2]Note that the scheme is different from the differential modulation, where data are encoded in the phase difference between successive *symbols*. Differential modulation is not practical for low-data-rate UWB signals, due to the long duration of the required delays.

In a slow fading environment, TR collects multipath energy efficiently without requiring multipath tracking or channel estimation. Analog autocorrelation also alleviates the burden on A-D converters, thus lowering the power consumption by interface circuits in the UWB regime. Nevertheless, TR autocorrelators entail several drawbacks and usually show worse performance than coherent RAKE receivers: the use of reference pulses increases transmission overhead and reduces data rate, which results in reduced transmission power efficiency; the bit-error-rate (BER) performance is limited by the noise term in the reference signal [38, 41]. Different methods have been proposed to improve the error performance either by modulation parameter selection [43], signal set selection [44], or receiver processing [41, 45–48]. Finally, the performance of TR receivers relies on the implementation of accurate analog delay lines which can save and delay the reference waveforms for up to tens of nanoseconds. This is still a big challenge to current circuit technology.

2.4. Multi-band design

Most of the published UWB research to date has focused on single-band systems. The multi-band UWB concept has been introduced in more recent proposals [24–26]. The basic idea of the multi-band approach is to divide the 7.5GHz (3.1-10.6GHz) unlicensed UWB spectrum set by the FCC [8] into multiple smaller sub-bands[3]. The multi-band architecture is expected to provide a more flexible and scalable usage of spectrum, thus mitigating co-existence (e.g. with 802.11a) and many implementation issues. Information on each of the sub-bands can be transmitted using either single-carrier (pulse-based) or multi-carrier (OFDM, stands for orthogonal frequency-

[3]The minimum bandwidth is 500MHz each sub-band, as regulated by the FCC.

division multiplexing) techniques. [3] offered very good comparison and overview on these two schemes, which are replicated here for completeness and for readers' convenience.

2.4.1. Multi-band pulsed scheme

The main disadvantage of narrow time domain pulses is the difficulty on building radio frequency (RF) and analog circuits as well as high-speed analog-to-digital converters (ADCs) to process signals of extremely wide bandwidth and its usually resulted high power consumption. Collection of sufficient energy in dense multipath environments requires a large number of RAKE fingers. The pulsed multi-band approach can eliminate the disadvantages associated with large front-end processing bandwidth by dividing the spectrum into several subbands. However, it is difficult to collect significant multipath energy using a single RF chain. There are also very stringent frequency switching time requirements at both transmitter and receiver.

2.4.2. Multi-band OFDM scheme

An OFDM carrier signal is the sum of a number of orthogonal sub-carriers (also called tones), with baseband data on each sub-carrier being independently modulated. The multi-band OFDM (MB-OFDM) system transmits information on each subband, using multiple sub-carriers with OFDM modulation. The transmitted OFDM symbols are time-interleaved across the subbands. It can efficiently capture multipath energy with a single RF chain. The drawbacks include that the transmitter is more complex due to the need of inverse fast Fourier transform (IFFT) operations, and the peak-to-average ratio (PAR) is usually higher than pulse-based approaches. Further details on OFDM and MB-OFDM can be found in [25, 26, 69].

3. PERFORMANCE OF A MULTI-BAND ULTRA-WIDEBAND SYSTEM IN INDOOR CHANNELS

3.1. Introduction

The achievable maximum data rate in a single-band UWB system is determined by the channel multipath delay that may cause inter-symbol interference (ISI). Given the same amount of bandwidth, a multi-band system might provide a higher throughput than a single-band system. In this chapter, we study the performance of a proposed multi-band UWB system that employs antipodal pulse amplitude modulation (PAM). We will first introduce a frequency-hopped, multi-band UWB signaling scheme. We then derive its analytical error performance in indoor lognormal fading channels. We will also provide simulation results to validate some of the analytical results and compare the performance of a signal-band system and a multi-band system.

3.2. System Model

3.2.1. Transmitter model

In a commonly used binary PAM UWB system, the amplitude of short-duration pulses are modulated by information bits. The typical width of these pulses is in the range of a fraction of a nanosecond to a few nanoseconds. To avoid severe ISI, adjacent pulses must be sufficiently separated, resulting in the transmitted signals with a low-duty cycle. For a single-user multi-band system, we assume that there are M adjacent sub-bands of equal bandwidth. Successive input pulses are frequency hopped to different sub-bands. To maximize the separation between adjacent pulses in the same sub-band, each pulse is hopped to a different sub-band and the period of the hop sequence equals M, the number of sub-bands. Hopping of a user's signal to different

sub-bands in the time domain helps to improve the system's narrowband interference immunity, combat frequency selective fading, lower the peak-to-average power ratio, and further smooth power spectrum of transmitted signals.

The transmitted UWB signal in a particular sub-band of a single-user, multi-band UWB system is expressed as

$$s(t) = \sum_{n=-\infty}^{\infty} \sqrt{E_b} b_i q_{f[i]}(t - iT_s) \tag{3.1}$$

where $q_{f[i]}(t)$ is the short-duration UWB pulse shape (e.g. a carrier-modulated Gaussian monocycle) of width T_m, E_b is the symbol energy, T_s is the symbol interval ($T_s \gg T_m$) in each sub-band, and $b_i \in \{1, -1\}$ is the i^{th} nonreturn-to-zero converted bit. The energy of the basic pulse $q(t)$ (before carrier modulation) is normalized to $E_p = \int_{-\infty}^{\infty} p^2(t)dt = 1$. To avoid partial correlation, we assume that $q(t)$ is non-zero only within the interval $0 \leq t \leq T_m$. The subscript $f[i]$ in (7.1) represents the sub-band in which the i^{th} pulse is transmitted. A band and time slot assignment scheme is illustrated in Fig. 3.1 where the modulating carriers for pulses of these sub-bands are not shown.

For a multi-user multi-band system, we restrict our analysis to the case where the number of users is less than or equal to the number of available sub-bands (M). This enables us to design appropriate hopping sequences for all users to avoid collision and to minimize inter-symbol interference caused by multipath delay. In this case, a simple time-division multiple-access scheme where all users are assigned to have an equal share of all possible time slots from all sub-bands can be designed. With such a condition, there will be no multiple-access interference (MAI) and the analysis and models for the multi-user system are the same as that of the single-user system.

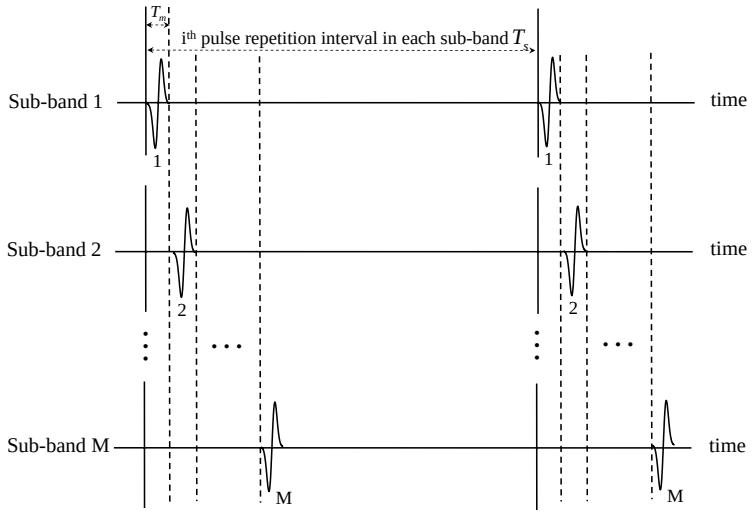

FIGURE 3.1. A band and time slot assignment scheme in a multi-band system.

3.2.2. Receiver model

We assume that there is no inter-band interference. After passing through the multipath fading channel, the transmitted signal $s(t)$ in a particular sub-band given in (7.1) is received in multiple independently faded copies at the receiver as

$$r(t) = \sum_{l=0}^{L-1} \alpha_l s(t - lT_m) + n(t) \tag{3.2}$$

where $n(t)$ is the white Gaussian noise process with a two-sided power spectral density (PSD) of $N_0/2$. The received signal is correlated with the pulse shape $q(t)$ and then sampled. The receiver combines L_p ($L_p < L$) resolvable paths for data detection. Due to its simplicity, the equal gain combining (EGC) technique will be applied in this chapter. This also makes the analytical performance analysis tractable.

Assuming perfect timing and channel estimation, we obtain the received signal for the l^{th} path as

$$r(l) = \int_0^{T_s} r(t)p(t - lT_m)dt. \tag{3.3}$$

Because the channel coefficient is expressed as $\alpha_l = \lambda_l \beta_l$ where $\lambda_l \in \{\pm 1\}$, the decision variable for the i^{th} bit is expressed as

$$\Delta_i = \sum_{l=0}^{L_p-1} r(l)\lambda_l = b_i\phi + \varphi + \psi \tag{3.4}$$

where

$$\phi = \sqrt{E_b} \sum_{l=0}^{L_p-1} |\alpha_l| \tag{3.5a}$$

$$\varphi = \sqrt{E_b} \sum_{n=1}^{N} \sum_{l=0}^{L_p-1} \alpha_{n\varepsilon+l} b_{i-n} \lambda_l \tag{3.5b}$$

$$\psi = \sum_{l=0}^{L_p-1} n(l)\lambda_l \tag{3.5c}$$

and N represents the number of previous symbols whose delayed copies interfere with the current symbol (causing ISI), $\varepsilon = MT_s/T_m$ and εT_m represents the time elapsed between two adjacent pulses transmitted in the same band.

It is easy to recognize that the right-hand side of (3.5a), (3.5b), and (3.5c) represent, respectively, the desired signal, the inter-symbol interference, and the noise term. The decision rule for the i^{th} bit is obtained as

$$\Delta_i > 0, \quad \text{decide } 1 \tag{3.6a}$$

$$\Delta_i < 0, \quad \text{decide } 0. \tag{3.6b}$$

3.3. Performance Analysis

Without loss of generality, we assume that the i^{th} transmitted bit b_i is a 1 and derive the conditional bit error rate (BER)[1]. With this assumption, the instantaneous received signal part simply equals to ϕ given in (3.5a).

The NL_p terms on the right-hand side of (3.5b) are independent zero-mean random variables (RVs). For a typical UWB channel, the power decay factor ρ is small enough so that these NL_p terms can be approximately treated as identically distributed. Thus, when the number of paths combined by the receiver (L_p) is large (e.g., greater than 3) and N (N depends on the data rate and the channel delay spread) is also large, the ISI term φ given in (3.5b) can be approximated as a single Gaussian RV, i.e., $\varphi \sim \mathcal{N}(0, \sigma_\varphi^2)$. The variance of this zero-mean interference term is obtained to be

$$\sigma_\varphi^2 = E\{\varphi\varphi^*\} = E_b \sum_{n=1}^{N} \sum_{l=0}^{L_p-1} E\left\{\alpha_{n\varepsilon+l}^2\right\} \tag{3.7}$$

where $E\{\cdot\}$ represents statistical expectation and $\{\cdot\}^*$ denotes complex conjugate.

The approximated Gaussian noise term φ is independent of the noise term ψ. Because $\lambda_l \in \{1, -1\}$ with equal probability to take on the value of 1 or -1, λ_l applied in the EGC process does not change the statistics of the noise term ψ. Thus, ψ is still a zero-mean Gaussian RV with a variance that is easily obtained to be $\sigma_\psi^2 = L_p \frac{N_0}{2}$. The combined noise term, $\varphi + \psi$, is approximated as a Gaussian distributed RV, i.e., $\varphi + \psi \sim N\left(0, \sigma_\psi^2 + \sigma_\varphi^2\right)$.

Obviously, ϕ given in (3.5a) is a random variable. In order to determine the analytical BER expression, we derive the conditional BER conditioned on a fixed set of

---

[1]When input bits have an equal probability to take on the value of 1 and 0, the conditional BER equals the average BER. This condition is assumed to be true in this thesis.

channel coefficients $\{\alpha_0, \cdots, \alpha_{L_p-1}\}$. The conditional BER can then be averaged over the probability density function of ϕ to compute the average BER. As mentioned in Chapter 2.2, channel coefficient α_l can be modeled as $\alpha_l = \lambda_l \beta_l,$ where $\lambda_l \in \{1, -1\}$ and $\beta_l = |\alpha_l|$ is a lognormal RV. Let

$$\beta_l = |\alpha_l| = e^{y_l} \tag{3.8a}$$

$$\phi_l = \sqrt{E_b}|\alpha_l| = e^{c_0/2+y_l} \tag{3.8b}$$

where $c_0 = \ln(E_b)$ and y_l is a normal RV, i.e. $y_l \sim \mathcal{N}(\mu_{y_l}, \sigma^2_{y_l})$. The k^{th} moment of the lognormal variable β_l is given as

$$E\{\beta_l^k\} = e^{k\mu_{y_l}+k^2\sigma^2_{y_l}}. \tag{3.9}$$

Because fading coefficients for different paths are independent from one another, ϕ is a sum of independent lognormal RVs. Although an exact closed-form expression for the probability density function of a sum of independent lognormal RVs does not exist, there are a number of methods to approximate it. One of these methods, the Wilkinson's method [34], will be applied in this paper to approximate the pdf. Let $\phi = e^z$ where z, $z \sim \mathcal{N}(\mu_z, \sigma_z^2)$, is a normal RV. In Wilkinson's method, the two parameters μ_z and σ_z are obtained by matching the first two moments of ϕ with the first two moments of $\sum_{l=0}^{L_p-1} \phi_l$. The mean and variance are obtained as $\mu_z = \ln(E_{L1}^2/\sqrt{E_{L2}})$ and $\sigma_z = \sqrt{\ln(E_{L2}/E_{L1}^2)}$. The two quantities, E_{L1} and E_{L2}, are related to μ_y and σ_y^2 as

$$E_{L1} = \sum_{l=0}^{L_p-1} e^{(c_0/2+\mu_{y_l}+\sigma^2_{y_l}/2)} \tag{3.10a}$$

$$E_{L2} = \sum_{l=0}^{L_p-1} e^{(c_0+2\mu_{y_l}+2\sigma^2_{y_l})} + 2\sum_{u=1}^{L_p-1}\sum_{v=0}^{u-1} e^{(c_0+\mu_{y_u}+\mu_{y_v}+\sigma^2_{y_u}/2+\sigma^2_{y_v}/2)} \tag{3.10b}$$

The approximated pdf of ϕ is obtained as

$$f(\phi) = \frac{1}{\phi\sqrt{2\pi\sigma_z^2}} exp\left[-\frac{(\ln(\phi) - \mu_z)^2}{2\sigma_z^2}\right]. \tag{3.11}$$

The bit error rate expression conditioned on a fixed set of channel coefficients $\{\alpha_0, \alpha_1, \cdots, \alpha_{L_p}\}$ is obtained as

$$\begin{aligned} p(\phi) &= \frac{1}{\sqrt{2\pi(\sigma_\psi^2 + \sigma_\varphi^2)}} \int_{-\infty}^{0} exp\left[-\frac{(\lambda - \phi)^2}{2(\sigma_\psi^2 + \sigma_\varphi^2)}\right] d\lambda \\ &= \frac{1}{2} erfc\left(\sqrt{\frac{\phi^2}{L_p N_0 + 2\sigma_\varphi^2}}\right). \end{aligned} \tag{3.12}$$

The average BER can be calculated by averaging the conditional BER $p(\phi)$ over $f(\phi)$ as

$$P_b = \int_0^\infty p(\phi) f(\phi) d\phi. \tag{3.13}$$

3.4. Numerical Results and Discussion

For all analytical and simulation results, the average signal-to-noise ratio (SNR) per bit is defined as $\overline{\gamma}_b = \frac{E_b}{N_0} \sum_{l=0}^{L_p-1} e^{-\rho l}$. Based on measurement results, it was reported in [19, 22] that the root-mean-square (RMS) delay spread τ_{rms} of indoor wireless channels is between 20 and 30ns for 5-30m antenna separations. In all simulations, $\tau_{rms} = 27ns$ is chosen.

Given the same data rate, an increased number of sub-bands results in a larger time separation between adjacent bits that will hop to the same sub-band. This helps to lower the potential ISI. With a fixed total bandwidth, a smaller sub-channel bandwidth results in a larger number of sub-bands. For these reasons, the $3.1-6.6GHz$ spectrum is divided into 7 sub-bands of $500MHz$ (the minimum bandwidth regulated by the FCC) each in our simulation for multi-band systems. The UWB pulse shapes for each sub-band is obtained by carrier modulating the same truncated Gaussian monocyle $q(t)$.

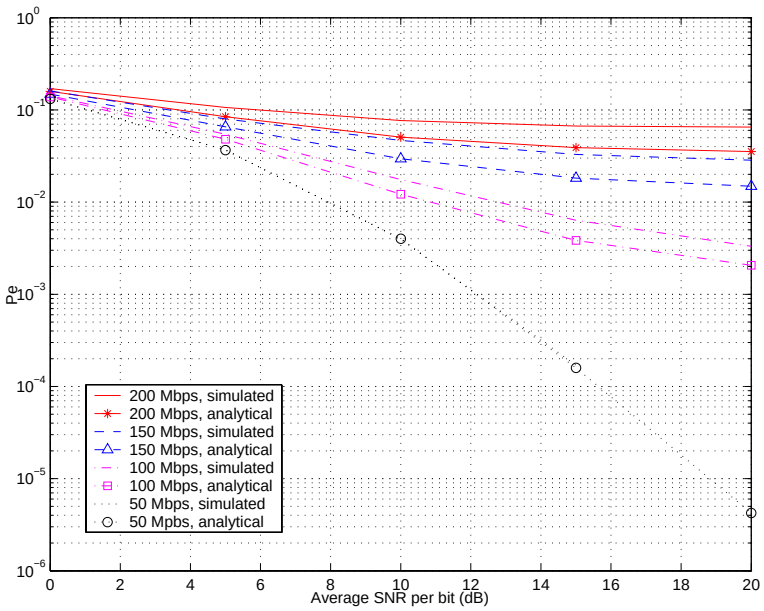

FIGURE 3.2. Theoretical and simulated BER versus SNR per bit ($L_p = 3$).

The truncated Gaussian monocycle has a $4ns$ pulse width and a $10dB$ bandwidth of $500MHz$.

Fig. 3.2 shows the analytical and simulated error performance of a multi-band system with different data rates. The standard deviation of the fading coefficients applied is $4.8dB$. Thus, the standard deviation of y_l introduced in (3.8a) is calculated as $\sigma_{y_l} = 4.8/(20log_{10}(2.71828) = 0.55$. A $27ns$ channel RMS delay spread is used. The number of resolvable multipath components within $20dB$ down from the strongest path is obtained to be 35 using the approach given in [32]. The power decay factor is thus calculated to be $\rho = 0.1316$. Simulation results match reasonably well with the analytical results for the set of system parameters chosen. The factors that caused the slight mismatch between the analytical and simulation results are the two approximations made in Section 3.3 of this chapter.

The number of paths combined (L_p) obviously affects the receiver performance. Fig. 3.3 shows the analytical and simulated BER versus L_p curves of the multi-band system. The average SNR per bit is fixed at $\overline{\gamma}_b = 15dB$ and aggregated data rates over all sub-bands are chosen to be 50, 100, and $150Mbps$. All channel-related parameters applied are the same as the simulation which generated Fig. 3.2. With the average SNR per bit $\overline{\gamma}_b$ adopted in this paper, it is found that the performance does not, as in any system with path diversity, improve linearly with the number of paths combined.

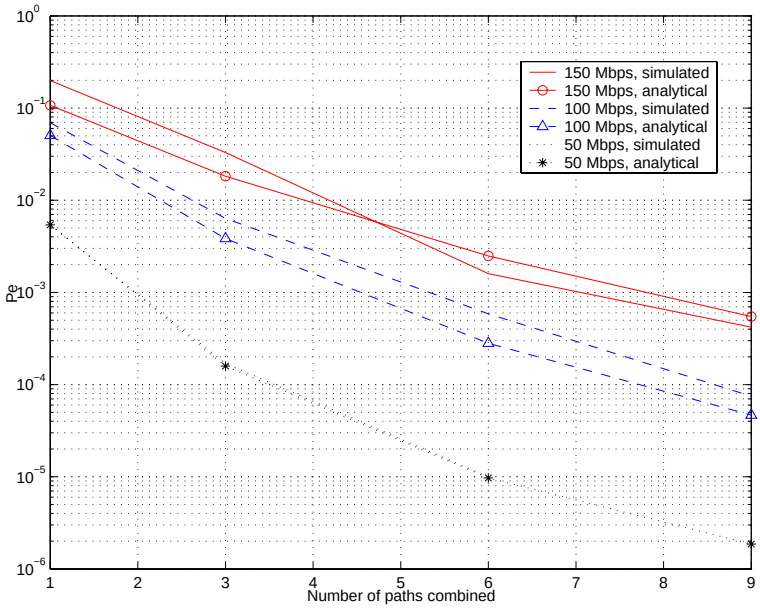

FIGURE 3.3. Theoretical and simulated BER versus number of paths combined by the receiver ($\overline{\gamma}_b = 15dB$).

For comparison purposes, the simulated performance of a single-user, single-band system with the same total bandwidth as the above two cases is shown in Fig. 3.4. The width of the pulse transmitted is $0.3ns$, which corresponds to a 3-dB bandwidth of $3.5GHz$ (3.1-6.6GHz). Given the same channel delay spread and σ_{y_l} as previous cases, the number of resolvable paths is calculated to be 465, which yields a power decay factor of $\rho = 0.01$. By comparing Figs. 3.2 and 3.4, it is observed that given the

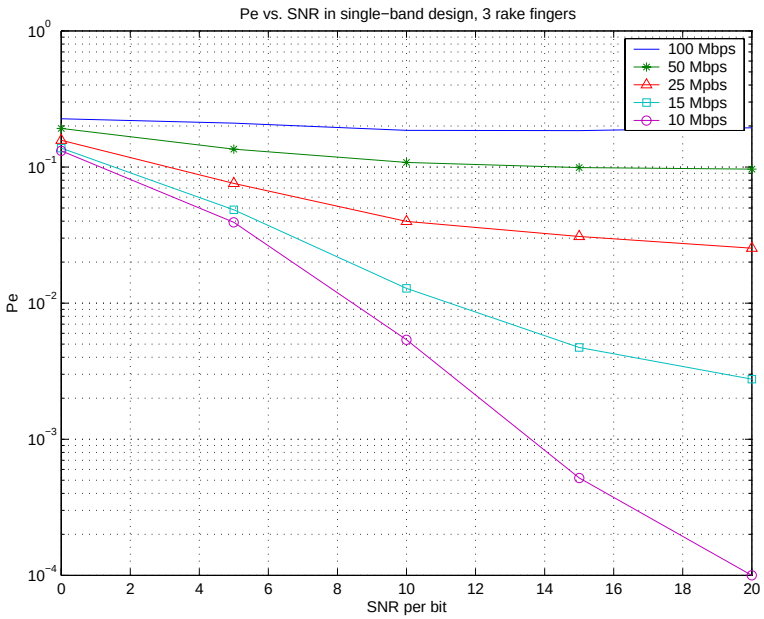

FIGURE 3.4. Simulated BER versus SNR per bit of a single-band UWB system ($L_p = 3$).

same BER, the multi-band system achieves almost M (number of sub-bands) times the throughput of a single-band system.

To assess the potential performance improvement that can be achieved by a multi-band system with maximal ratio combining (MRC) over an EGC system, we simulated their BER versus $\overline{\gamma}_b$ curves with the same set of parameters that were applied to obtain Fig. 3.2. These results are shown in Fig. 5.1. Although the MRC technique has a higher complexity, it does provide an observable performance improvement.

3.5. Conclusions

In this chapter, the analytical error performance of a multi-band UWB system in indoor lognormal fading channels has been derived. Simulation results validated the

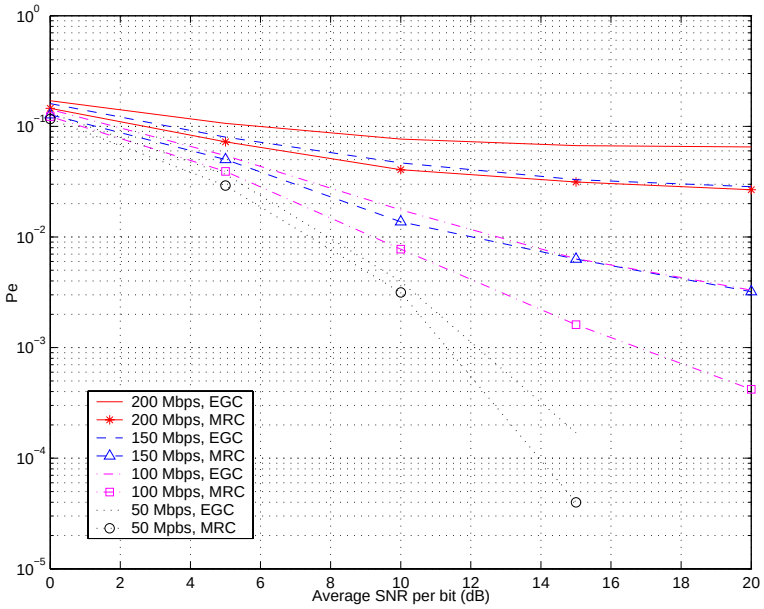

FIGURE 3.5. Simulated error performance of a multi-band UWB system with MRC and EGC techniques ($L_p = 3$).

accuracy of the analytical approach applied. The inter-symbol interference caused by channel multipath delay has been found to limit the achievable throughput in UWB systems. Performance of a single-band system and a multi-band system with the same total bandwidth has been compared. It has been found that the multi-band system could potentially provide a much higher throughput than the single-band system given the same total bandwidth and channel conditions.

4. ON THE OPTIMUM LINEAR RECEIVER FOR IMPULSE RADIO SYSTEMS IN THE PRESENCE OF PULSE OVERLAPPING

4.1. Introduction

One of the advantages of impulse radio UWB communications is its ability to resolve individual multipath components. This requires a RAKE receiver to gain path diversity and to capture multipath energy. Existing research on detection and performance analysis of pulse-based UWB systems has only addressed, to the authors' knowledge, the ideal case that received adjacent paths are separated in time by at least one pulse width. This assumption might be accurate enough for communications in line-of-sight (LOS) environments. In dense multipath non-LOS environments, however, there could be severe overlapping between adjacent received pulses, and pulse overlapping must be considered in performance analysis and receiver design. This is especially the case when a multi-band pulsed UWB [11, **?**, 24] is adopted. In a typical indoor environment, measurements [19, 23] have shown that the typical average multipath arrival rate is in the range of $0.5 - 2ns$. For an impulse radio UWB system using 500MHz-1GHz bandwidth (10dB bandwidth), which is common for multi-band UWB systems, the typical pulse width is in the range of $2 - 4ns$ [35]. In this situation, apparently the received multipath components will experience severe time overlap and the assumption of ideal multipath resolution becomes inappropriate.

It is well known that a RAKE receiver with maximal ratio combining (MRC) [72] is optimum when the desired signal is distorted only by the additive white Gaussian noise (AWGN). In the presence of inter-pulse interference (IPI) caused by pulse overlapping, a minimum mean-square error (MMSE) scheme [73] is expected to improve the receiver performance over the MRC scheme. The major purpose of this chapter is to derive the optimum MMSE scheme for pulsed UWB systems when pulse overlap-

ping is considered and compare the performance of the MMSE receiver with that of a generic MRC receiver in an indoor lognormal fading environment.

4.2. System Model

In a commonly used binary pulse amplitude modulated (PAM) UWB system, the amplitude of short-duration pulses are modulated by information bits. These pulses are then transmitted over a frequency-selective lognormal fading channel [19, 23] with additive white Gaussian noise. The transmitted signal is expressed as

$$s(t) = \sum_{i=-\infty}^{\infty} s_i(t) = \sum_{i=-\infty}^{\infty} \sqrt{E_b} b(i) p(t - iT_b) \tag{4.1}$$

where $p(t)$ is the short-duration UWB pulse shape of width T_m, E_b is the bit energy, T_b is the bit interval ($T_b \gg T_m$), and $b(i) \in \{1, -1\}$ is the i^{th} information bit. The energy of the basic pulse $p(t)$ is normalized to $E_p = \int_{-\infty}^{\infty} p^2(t)dt = 1$.

4.3. Optimum Detection in the Presence of Pulse Overlapping

We assume that the signaling rate is such that the received signal energy of a particular bit is contained within one pulse repetition interval (T_b) so that there is no inter-symbol interference (ISI). Thus, we can focus on a particular bit interval in the receiver modelling. After passing through the multipath fading channel described by (5.2), the transmitted signal $s_i(t)$ (for the i^{th} information bit) given in (7.1) is received in multiple independently faded copies as

$$r(t) = \sum_{l=0}^{L-1} \alpha_l s_i(t - \tau_l) + n(t) \tag{4.2}$$

where $n(t)$ is the zero-mean white Gaussian noise process with a two-sided power spectral density (PSD) of $N_0/2$.

In a generic RAKE receiver, the received signal is filtered by a matched filter that is matched to $p(t)$, delayed and sampled according to the relative delays of different paths, and then combined. The first L_p ($L_p \leq L$) received paths ($l = 0, \cdots, L_p - 1$) are statistically the strongest among all multipath components. For simplicity, these L_p paths will be linearly combined when a generic RAKE receiver is employed.

The sampled signal for the l^{th} path of the i^{th} information bit is expressed as

$$r_l = \sum_{k=0}^{L_p-1} \left(\alpha_k \sqrt{E_b} b(i) \int_{-\infty}^{\infty} p(t-\tau_k) p(t-\tau_l) dt \right) + n_l, \quad l = 0, 1, \ldots, L_p - 1 \quad (4.3)$$

where the zero-mean noise component is $n_l = \int_{-\infty}^{\infty} n(t) p(t-\tau_l) dt$ with variance $\sigma_{n_l}^2 = N_0/2$. Note that due to the pulse overlapping, noise components $n_l, l = 0, \cdots, L_p$, may not be mutually independent.

By defining the partial correlation between $p(t-\tau_k)$ and $p(t-\tau_l)$ as $\rho_{l,k} = \int_{-\infty}^{\infty} p(t-\tau_l) p(t-\tau_k) dt = \rho_{k,l}$, we can simplify Eq. (7.3) as

$$r_l = \sum_{k=0}^{L_p-1} \rho_{l,k} \alpha_k \sqrt{E_b} b(i) + n_l, \quad l = 0, 1, \ldots, L_p - 1. \quad (4.4)$$

Since the energy of $p(t)$ is normalized to unity, $\rho_{l,k} = 1$ for $l = k$ and $0 < \rho_{l,k} < 1$ for $l \neq k$, with the exception that $\rho_{l,k} = 0$ if $p(t-\tau_k)$ and $p(t-\tau_l)$ do not overlap with each other.

The received L_p samples per bit interval can be written in vector form as $\boldsymbol{r} = [r_0, \ r_1, \ \ldots, \ r_{L_p-1}]^T$, where $(\cdot)^T$ denotes transpose. This received signal vector is expressed as

$$\boldsymbol{r} = \sqrt{E_b} b(i) \boldsymbol{R} \boldsymbol{\alpha} + \boldsymbol{n} \quad (4.5)$$

where $\boldsymbol{\alpha} = [\alpha_0,\ \alpha_1,\ \cdots,\ \alpha_{L_p-1}]^T$ is the channel fading coefficient vector, $\boldsymbol{n} = [n_0,\ n_1,\ \cdots,\ n_{L_p-1}]^T$ is the noise vector, and

$$\boldsymbol{R} = \begin{bmatrix} 1 & \rho_{0,1} & \cdots & \rho_{0,L_p-1} \\ \rho_{1,0} & 1 & \cdots & \rho_{1,L_p-1} \\ \vdots & \vdots & \ddots & \vdots \\ \rho_{L_p-1,0} & \rho_{L_p-1,1} & \cdots & 1 \end{bmatrix} \tag{4.6}$$

is the partial correlation matrix, which can be calculated using the relative multipath delays τ_l and the pulse shape $p(t)$.

The covariance matrix of the zero-mean noise vector $\boldsymbol{n}$ given in (7.9) is obtained to be $E\{\boldsymbol{n}\boldsymbol{n}^H\} = \boldsymbol{R}\frac{N_0}{2}$, where $(\cdot)^H$ denotes conjugate transpose. The decision variable is obtained by combining the L_p elements of $\boldsymbol{r}$ using certain tap weights. Because the noise components of $r_l, l = 0, \cdots, L_p$, are identically distributed, the tap weights can be set to match the conjugates of the channel fading coefficients $\boldsymbol{\alpha}^* = [\alpha_0,\ \alpha_1,\ \ldots,\ \alpha_{L_p-1}]^H$, which results in the generic RAKE receiver with MRC. Mathematically, this approach is not optimum because of the IPI caused by pulse overlapping and noise correlation.

It is of interest to derive the optimum linear combining scheme and compare its performance with that of the MRC scheme. For the optimum linear MMSE receiver, we need to determine the optimum tap weight vector $\boldsymbol{w} = [w_0,\ w_1,\ \cdots,\ w_{L_p-1}]^T$ to form the decision variable $\Delta = \boldsymbol{w}^T\boldsymbol{r}$. For the typical target desired signal $y = \sqrt{E_b}b(i)$, the weight vector is chosen to be such that the mean-square value of error $e = y - \boldsymbol{w}^T\boldsymbol{r}$ is minimized. The mean-square error (MSE) is easily determined as

$$\begin{aligned} \varepsilon &= E\{ee^H\} \\ &= E\{yy^H\} + \boldsymbol{w}^T E\{\boldsymbol{r}\boldsymbol{r}^H\}\boldsymbol{w}^* - E\{y^H\boldsymbol{r}^T\}\boldsymbol{w} - E\{y\boldsymbol{r}^H\}\boldsymbol{w}^*. \end{aligned} \tag{4.7}$$

By letting the derivative of ε with respective to $\boldsymbol{w}$, $d\varepsilon/d\boldsymbol{w} = E\{\boldsymbol{r}\boldsymbol{r}^H\}\boldsymbol{w}^* - E\{y^H\boldsymbol{r}\}$, equal zero, we obtain the conjugate of the optimum MMSE weight vector as

$$\boldsymbol{w}^* = \boldsymbol{P}^{-1}\boldsymbol{q} \tag{4.8}$$

where

$$\boldsymbol{P} = E\{\boldsymbol{r}\boldsymbol{r}^H\} \tag{4.9a}$$

$$\boldsymbol{q} = E\{y^H\boldsymbol{r}\}. \tag{4.9b}$$

With the quasistatic slowly fading channel model adopted, the channel fading coefficients and relative path delays are static over a block of data. The *instantaneous* matrix given in (4.9a) and column vector given in (4.9b) are obtained as

$$\boldsymbol{P} = E_b\boldsymbol{R}\boldsymbol{\alpha}\boldsymbol{\alpha}^H\boldsymbol{R}^H + \boldsymbol{R}\frac{N_0}{2} \tag{4.10a}$$

$$\boldsymbol{q} = E_b\boldsymbol{R}\boldsymbol{\alpha}. \tag{4.10b}$$

It will be very interesting to find out the difference between the MRC scheme with the tap weight $\boldsymbol{\alpha}^*$, for which IPI caused by pulse overlapping and noise correlation have been ignored, and the optimum MMSE scheme whose tap weight is given in Eq. (4.8). To analyze this, we re-write $\boldsymbol{w}^*$ as

$$\begin{aligned}\boldsymbol{w}^* &= E_b\left[E_b\boldsymbol{R}\left(\boldsymbol{\alpha}\boldsymbol{\alpha}^H\boldsymbol{R}^H + \frac{N_0}{2E_b}\boldsymbol{I}_{L_p}\right)\right]^{-1}\boldsymbol{R}\boldsymbol{\alpha} \\ &= \left(\boldsymbol{\alpha}\boldsymbol{\alpha}^H\boldsymbol{R}^H + \frac{N_0}{2E_b}\boldsymbol{I}_{L_p}\right)^{-1}\boldsymbol{\alpha}\end{aligned} \tag{4.11}$$

where $\boldsymbol{I}_{L_p}$ is the $L_p \times L_p$ identity matrix.

It is easy to obtain that $\left(\boldsymbol{\alpha}\boldsymbol{\alpha}^H\boldsymbol{R}^H + \frac{N_0}{2E_b}\boldsymbol{I}_{L_p}\right)\boldsymbol{\alpha} = \left(\zeta + \frac{N_0}{2E_b}\right)\boldsymbol{\alpha}$, where $\zeta = \boldsymbol{\alpha}^H\boldsymbol{R}^H\boldsymbol{\alpha}$ is a scalar. Thus, Eq. (4.11) transforms to[1]

$$\boldsymbol{w}^* = \frac{1}{\zeta + \frac{N_0}{2E_b}}\boldsymbol{\alpha}. \tag{4.12}$$

Eqs. (4.11) and (4.12) indicate that $\boldsymbol{\alpha}$ is an eigen vector of matrix $\left[\boldsymbol{R}\left(\boldsymbol{\alpha}\boldsymbol{\alpha}^H\boldsymbol{R}^H + \frac{N_0}{2E_b}\boldsymbol{I}_{L_p}\right)\right]^{-1}\boldsymbol{R}$. This shows, interestingly, that the optimum MMSE tap weight $\boldsymbol{w}$ is essentially the same as the MRC tap weight $\boldsymbol{\alpha}^*$. We can therefore conclude that the generic MRC RAKE receiver performs the same as the linear optimum MMSE receiver when the unavoidable pulse overlapping in a pulsed UWB system is taken into consideration.

In a code-division multiple-access (CDMA) system, an MMSE receiver, when used as an equalizer in the presence of ISI and multiple-access interference (MAI) [36], should perform better than a generic RAKE receiver. In the pulsed UWB system, all L_p received paths given in Eq. (4.4) carry the same information bit, and the MMSE receiver derived in this chapter is designed to optimally combine these components in the presence of pulse overlapping. In a CDMA system, however, MAI and ISI are from other users or bits, and the MMSE receiver separates desired signals from interference. When there are both ISI and IPI in the pulsed UWB system, an MMSE receiver is expected to perform better than an MRC RAKE receiver.

---

[1]This relationship is obtained as follows. Let $\boldsymbol{M}\boldsymbol{\alpha} = m\boldsymbol{\alpha}$, where $\boldsymbol{M}$ is a positive definite matrix, m is a scalar, and $\boldsymbol{\alpha}$ is a vector. We can write $\boldsymbol{M}^{-1}\boldsymbol{M}\boldsymbol{\alpha} = \boldsymbol{\alpha} = \boldsymbol{M}^{-1}m\boldsymbol{\alpha}$, from which $\boldsymbol{M}^{-1}\boldsymbol{\alpha} = \frac{1}{m}\boldsymbol{\alpha}$ follows.

4.4. Simulation Results and Discussion

In obtaining simulation results, a carrier-modulated, truncated Gaussian pulse is applied as the UWB pulse shape $p(t)$. This pulse has a width of $T_m = 2ns$ and a 10dB bandwidth of 1GHz. We adopted the CM3 channel model [19] with a root-mean-square (RMS) delay spread of $15ns$, an average cluster arrival rate of 0.0667/ns, and an average path arrival rate of 2/ns. The cluster decay factor applied is $\Gamma = 14ns$, and the ray decay factor applied is $\gamma = 7.9ns$. The standard deviation of the fading coefficients chosen is 3.4dB. The average power of the first path is normalized as $E\{|\alpha_0|^2\} = 1$. It is assumed that the transmission rate is such that inter-symbol interference caused by channel excess delay is negligible. Also, the receiver is assumed to have perfect knowledge of the channel coefficients and delays.

Fig. 7.5 shows the simulated performance curves of a RAKE receiver with the MRC scheme (with markers) and with the MMSE scheme (smooth curves) when different number of paths (L_p) are exploited. For all cases simulated, the generic MRC scheme performs exactly the same as the optimum linear MMSE scheme.

Although perfect channel knowledge is assumed in simulations, the above conclusion still holds with an imperfect knowledge of channel coefficients and delays. When $\boldsymbol{\alpha}$ and $\boldsymbol{R}$ in Eqs. (4.11) and (4.12) are estimates (imperfect), the same conclusion can still be made from Eq. (4.12).

4.5. Conclusions

Inter-pulse interference caused by pulse overlapping could severely degrade the performance of impulse radio UWB systems in dense multipath environments. In this chapter, the optimum linear MMSE receiver in the presence of pulse overlapping has been investigated. It has been found, by an analytical approach, that the generic RAKE

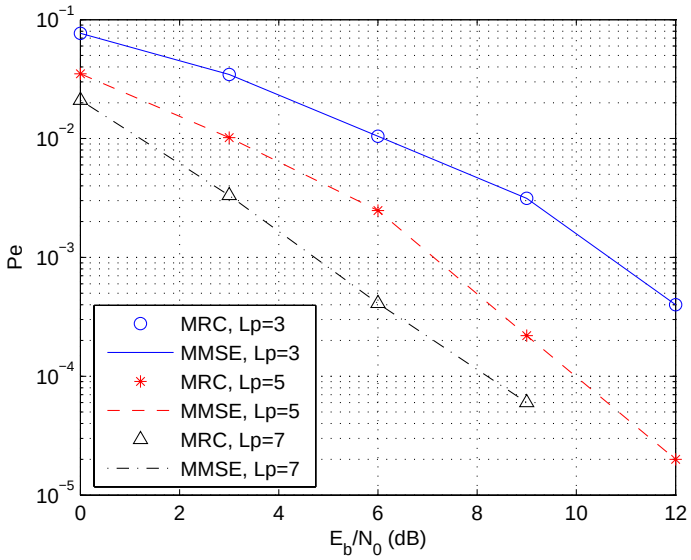

FIGURE 4.1. Simulated BER versus E_b/N_0 curves of the generic MRC receiver and the optimum MMSE receiver when IPI caused by pulse overlapping is taken into consideration.

receiver with MRC, which ignores IPI caused by pulse overlapping and noise correlation, performs the same as the optimum MMSE receiver. In simulations we have constructed the received signal waveforms and followed exactly the matched filtering process and the combining procedures. The waveform-based simulation results have validated this conclusion.

5. DECISION DIRECTED AUTOCORRELATION RECEIVERS FOR PULSED ULTRA-WIDEBAND SYSTEMS

5.1. Introduction

As that has been discussed previously in this thesis, Chapter 1 and 2, the popular traditional RAKE receiver method faces technical hurdles as well as implementation difficulties when it is applied in typical indoor propagation environments for pulsed UWB systems. As a suboptimal, low-complexity alternative, transmit-reference (TR) or autocorrelation receivers [38] – [48] have been investigated, which offer better multipath capture capability at much lower hardware complexity than RAKE receivers. Nevertheless, TR autocorrelators entail several drawbacks: the use of reference pulses increases transmission overhead and reduces data rate, which results in reduced transmission power efficiency; the bit-error-rate (BER) performance is limited by the noise term in the reference signal [38, 41].

In this chapter, we propose decision-directed autocorrelation (DDA) receivers that not only offer considerable performance improvement but also significantly reduce the signaling overhead (to zero asymptotically) compared with existing TR-type schemes. In DDA, a near-optimal correlation template is constructed directly from information-bearing received waveforms. Specifically, received symbol waveforms preceding the current symbol are delayed, multiplied by symbol decisions within the corresponding symbol window, and averaged to form the template waveform adaptively. This template is then used to correlate with the received signal to detect the current symbol. Because decision-directed (DD) symbol estimates are used in lieu of pilot symbols, the signaling overhead is reduced to zero asymptotically as the data length increases. Operating at the symbol rate, the DDA scheme does not require multipath tracking or channel estimation as is required in a RAKE receiver, and is still able

to capture energy from all received multipath components. It offers significant performance improvement over TR because noise in the self-derived template waveform is effectively alleviated through the decision-directed waveform averaging process. Provided that past symbol decisions are accurate, the resulting template is asymptotically optimal for correlation detection.

It is appropriate to compare the proposed DDA receiver with some existing schemes. In [41, 43, 45], the template waveform is formed by averaging over multiple previous reference pulses for autocorrelation operations. Unlike our scheme, these reference pulses result in signal power overheads and throughput penalties. In [47], a differential TR receiver was proposed to avoid reference pulses, but its error performance is limited by the noisy reference signal that is constructed without waveform averaging. The independent work [48] developed almost in parallel with this work [12] presented a decision-directed adaptive differential receiver, which is very similar to one of the recursive DDA detectors we will detail in Section 5.3.2. The focus of this chapter is to develop three different algorithms for obtaining the template waveforms based on the DDA principle. We not only establish the optimality of the three algorithms, but also compare their relative advantages and disadvantages. We also provide analytical error performance of these algorithms in practical lognormal fading environments.

5.2. System Model

In binary PAM UWB signaling, information bits $b[i] \in \{1, -1\}$ are transmitted over a train of ultra-short pulses $p(t)$ of pulse width T_p. The bit interval T_b is much larger than T_p, resulting in a low duty cycle transmission form. With energy E_b per bit,

the transmitted PAM UWB waveform is given by

$$s(t) = \sum_{i=-\infty}^{\infty} \sqrt{E_b} b[i] p(t - iT_b). \tag{5.1}$$

Pulsed UWB signaling gives rise to frequency selective channels, whose impulse responses can be modeled as tapped delay line filters. The aggregate channel after convolving with the transmitted pulse is given by [19]

$$h(t) = \sum_{l=0}^{L-1} \alpha_l p(t - \tau_l), \tag{5.2}$$

where L is the total number of multipath components, each with path fading gain α_l and delay τ_l relative to the first path. Perfect timing is assumed by setting $\tau_0 = 0$. The received waveform is thus given by

$$r(t) = \sum_{l=0}^{L-1} \alpha_l s(t - \tau_l) + n_o(t) = \sqrt{E_b} \sum_{i=-\infty}^{\infty} b[i] h(t - iT_b) + n_o(t), \tag{5.3}$$

where $n_o(t)$ is the ambient noise typically treated as a zero-mean white Gaussian process with power spectral density (PSD) $N_o/2$. To avoid channel-induced inter-symbol interference (ISI), the bit interval T_b is selected to be larger than the channel delay spread τ_{L-1}. In practice, the received signal $r(t)$ is first passed through an ideal band-pass filter with center frequency f_0 and double-sided bandwidth B which is chosen to be wide enough, larger than the signal's 10dB bandwidth, to avoid filter-induced ISI. It is also assumed that B is an integer multiple of $1/(2T_b)$. The filtered noise $n(t)$ is no longer white, but its autocorrelation in time can be very small due to the ultra-wide filter bandwidth B. The autocorrelation function of $n(t)$ is

$$R_n(\tau) = E\{n(t)n(t+\tau)\} = N_o B \frac{\sin(2\pi B\tau)}{2\pi B\tau} \cos(2\pi f_0 \tau). \tag{5.4}$$

Free of ISI, the received signal waveform can be described by the following one-shot model within each symbol period $t \in [iT_b, (i+1)T_b)$:

$$r_i(t) := r(t + iT_b) = \sqrt{E_b} b[i] h(t) + n_i(t), \quad t \in [0, T_b) \tag{5.5}$$

where $n_i(t) := n(t + iT_b)$, $t \in [0, T_b)$, is the corresponding T_b-long segment of the filtered noise $n(t)$.

Although our detector design will not rely on any specific channel model, the channel model measured by the IEEE 802.15.3a working group [19] will be used in our performance analysis.

5.3. Decision Directed Autocorrelation Receivers

For symbol-by-symbol correlation-based detection, the optimal correlation template is given by the aggregate channel waveform $h(t)$. Focusing on the one-shot model in (5.5), we first examine the optimal channel estimate of $h(t)$ given $\{r_i(t)\}_{i=0}^{\infty}$. When $h(t)$ is treated as deterministic but unknown, the optimal minimum mean square estimator of $h(t)$ (notwithstanding a scaling factor $\sqrt{E_b}$) conditioned on real-valued $\boldsymbol{v} := \{b[i]\}$ can be formulated as $\hat{h}(t) = argmin_{h(t)}\, E\{|r_i(t) - b[i]h(t)|^2\}$, which leads to

$$\hat{h}(t) = E\left\{b^{-1}[i]r_i(t)\right\}. \tag{5.6}$$

When it comes to binary PAM, we may equivalently replace $b^{-1}[i]$ by $b[i]$ for convenience. This channel estimator makes intuitive sense, because multiplying each received symbol waveform by the corresponding symbol takes out the symbol effect but retains the channel information. The remaining question is: how can we find $\hat{h}(t)$ in the absence of the knowledge of $\boldsymbol{v}$?

Our approach towards practical realizations of (5.6) in a slowly fading environment (channel remains static over a large number of bit intervals) is to employ DD operations. To this end, we construct a finite-sample implementation of (5.6) at the k-th symbol period as follows:

$$\hat{h}_k(t) = \frac{1}{k}\sum_{i=0}^{k-1} \hat{b}[i]r_i(t), \tag{5.7}$$

where $\hat{b}[i]$ are symbol decisions made in the past, and $\hat{h}_k(t)$ is the estimated template for detecting $b[k]$ (as well as future symbols, if needed). When past decisions are correct, $\hat{h}_k(t)$ approaches the optimal $\hat{h}(t)$ in (5.6) asymptotically as $k \to \infty$. The estimator in (5.7) does not require training overhead except during the initialization phase. A receiver using $\hat{h}(t)$ or $\hat{h}_k(t)$ as the correlation template is an autocorrelator, because the template is self-derived from the received signal $r(t)$.

An autocorrelation receiver can be viewed as a linear filter system to produce symbol decision statistic $y[k]$ from input waveform $r(t)$ via a filter $w(t) = \hat{h}(t)$. A binary decision can then be made according to $\hat{b}[k] = \text{sgn}\{y[k]\}$. It is thus natural to make connections with filter theory which may benefit our algorithm development and analysis. Let $x \cdot y := \int_0^{T_b} x(t)y(t)dt$ denote the inner product of two time-functions $x(t)$ and $y(t)$. Meanwhile, let $||x||^2 := \int_0^{T_b} x^2(t)dt$. Treating $w_k(t) = \hat{h}_k(t)$ as an adaptive filter, the following basic relations arise [70]:

$$\begin{aligned}
&\text{filter output:} && y[k] = \textstyle\int_0^{T_b} w_k(t)r_k(t)dt = w_k \cdot r_k \\
&\text{desired output:} && d[k] = b[k] \\
&\text{estimation error:} && e[k] = d[k] - y[k] \\
&\text{decision direction:} && d[k] = \text{sgn}\{y[k]\}.
\end{aligned}$$

Because of the decision direction $d[k] = \hat{b}[k]$ involved, we term the overall detector a decision directed autocorrelation (DDA) filter. The problem of estimating the correlation template $w(t)$ boils down to updating the adaptive filter weight $w_k(t)$. Implementation of the DDA detector in (5.7) can be accomplished either in batch operation or in an iterative manner. The former has faster convergence at the expense of higher complexity, while the latter is simpler to implement with an extra benefit of being capable of adapting to slow time-varying channels. Several implementation options will be presented next.

5.3.1. Sliding-window based DDA Detector

To implement (5.7) with a fixed filter memory length, we consider a sliding window approach in which the correlation-template filter $w_k(t)$ for detecting the k-th symbol is derived from the received symbol waveforms and the corresponding data decisions within a window of N symbol intervals preceding the current symbol. Specifically, $w_k(t)$ is constructed as

$$w_k(t) = \frac{1}{N} \sum_{j=1}^{N} \hat{b}[k-j] r_{k-j}(t). \tag{5.8}$$

This sliding-window DDA receiver is illustrated in Fig. 5.1. The data-demodulated (using symbol decisions) received signal from bits $k-N$ to $k-1$ are delayed and summed in an analog fashion. For initialization, a group of N pilot symbols are used at the beginning of the transmission to generate the initial template waveform and symbol decisions. Afterwards, the receiver is switched to the DD mode without using any pilot symbol.

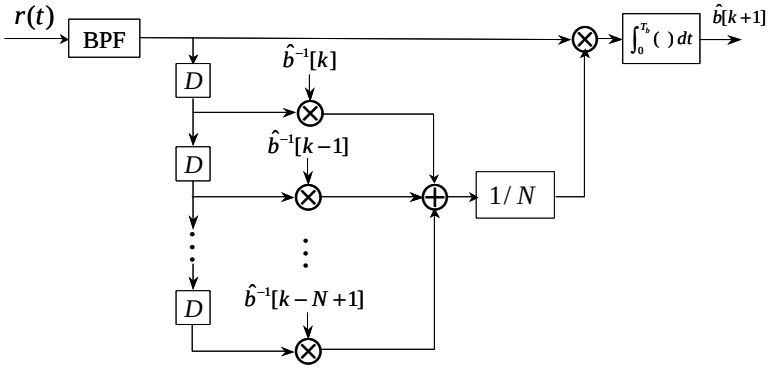

FIGURE 5.1. Sliding-window based DDA receiver.

In (5.8), the signal component of $w_k(t)$ is given by $\gamma_k \sqrt{E_b} h(t)$, which is exactly the ideal channel subject to scaling by $\sqrt{E_b}$ and an estimation efficiency factor $\gamma_k =$

$\left(\frac{1}{N}\sum_{j=1}^{N} b[k-j]\hat{b}[k-j]\right)$ in the range of $[0,1]$. When feedback decisions are correct, it holds that $\hat{b}[k-j] = b[k-j]$, $\forall k$, and $\gamma_k = 1$, which corresponds to maximum estimation efficiency equivalent to the training case. The correlation template can be equivalently written as

$$w_k(t) = \gamma_k \sqrt{E_b} h(t) + \xi_k(t). \tag{5.9}$$

where $\xi_k(t) = \frac{1}{N}\sum_{j=1}^{N} \hat{b}[k-j] n_{k-j}(t)$ is the noise component of the self-derived template. It can be shown that the PSD of $\xi_k(t)$ is $\sigma_k^2(N_o/2)$ with $\sigma_k^2 = 1/N$, $\forall k$. Obviously, $w_k(t)$ is very close to the optimal correlation template when N is large, as long as the channel remains static within the N symbol periods.

5.3.2. Recursive DDA Detector

The sliding window DDA detector requires N analog delay units, which can be expensive when N is large. To reduce hardware complexity, next we implement (5.7) in a recursive manner, where an update yielding the new template $w_{k+1}(t)$ relies only on the current template $w_k(t)$ and the newly received waveform $r_k(t)$. Common in adaptive filter designs, an alternative to (5.7) is given by the weighted time average $w_k(t) = \sum_{i=0}^{k-1} \mu^{k-1-i} \hat{b}[i] r_i(t)$, where μ is a positive exponential forgetting factor less than 1. This factor allows the template filter to accommodate possible non-stationarities in the input and gives adaptation capability in the presence of time-varying fading. In an iterative manner, the weighted-average expression leads to the following template estimate for a recursive DDA detector:

$$w_{k+1}(t) = \mu w_k(t) + \hat{b}[k] r_k(t). \tag{5.10}$$

The overall receiver structure is shown in Fig. 5.2, which only requires two delay units. Similar to (5.9), we can express the template estimate as $w_k(t) = \gamma_k \sqrt{E_b} h(t) + \xi_k(t)$.

Here γ_k is given by $\gamma_k = \sum_{i=0}^{k-1} \mu^{k-1-i}\hat{b}[i]b[i]$ which reduces to $\gamma_k = (1-\mu^k)/(1-\mu)$ under accurate past decisions. The noise PSD is given by $\sigma_k^2(N_o/2)$ with $\sigma_k^2 = (1-\mu^{2k})/(1-\mu^2)$.

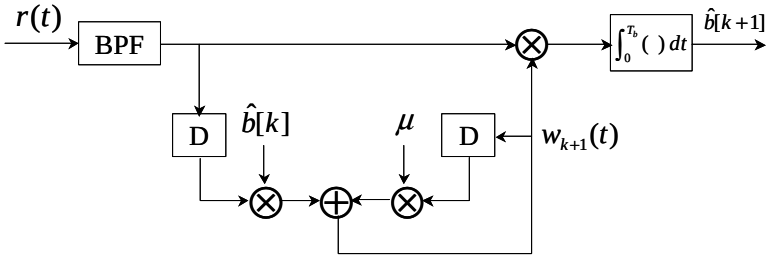

FIGURE 5.2. Low-complexity recursive decision directed autocorrelation structure.

5.3.3. LMS based DDA Detector

In Sections 5.3.1 and 5.3.2, decision direction is adopted to replace training symbols in the process of channel estimation. Alternatively, we may utilize decision direction as indication of the quality of past waveforms, which will in turn determine how these waveforms contribute to the updated correlation template. The goal is to detect $b[k]$ rather than estimating $h(t)$ per se. Next we present a least mean square (LMS) filter that provides a simple implementation of such an approach.

Consider the following least-square formulation for designing the template $w_k(t)$:

$$\min_{\hat{h}_k(t)} J(k) = \sum_{i=0}^{k} e^2[k] = \sum_{i=0}^{k} |d[k] - w_k \cdot r_k|^2 . \tag{5.11}$$

In the DD mode, the LMS solution to (5.11) yields the following adaptation steps:

$$\hat{b}[k] = \text{sgn}\{w_k \cdot r_k\} \tag{5.12a}$$

$$e[k] = \hat{b}[k] - w_k \cdot r_k \tag{5.12b}$$

$$w_{k+1}(t) = w_k(t) + \alpha r_k(t) e[k] \tag{5.12c}$$

where α is the step size that takes on a small value. Considering the fluctuation in the instantaneous received energy $||r_k||^2 := \int_0^{T_b} r_k^2(t)dt$, we may set $\alpha = \tilde{\alpha}/||r_k||^2$ or $\alpha = \tilde{\alpha}/(a + ||r_k||^2)$ with constants $a > 0$ and $0 < \tilde{\alpha} < 2$. These choices give rise to the normalized LMS algorithm, which is convergent in the mean square and potentially converges faster than a standard LMS algorithm.

To implement (5.12c), the same receiver structure in Fig. 5.2 applies. However, the input $r_k(t)$ in (5.12c) is not demodulated by $\hat{b}[k]$ before being added to the new filter update $w_{k+1}(t)$. Instead, it is adjusted by $\hat{b}[k]$ via the filter estimation error $e[k]$, which depends on the projected difference between $\hat{b}[k]$ and $r_k(t)$ rather than their cross-correlation as in (5.10). This operation reflects a different mechanism from that used in (5.8) and (5.10). In fact, LMS-based DDA filter corresponds to an adaptive implementation of the optimal Wiener filter $w_o(t) = arg\min \text{E}\{|b[i] - w_o \cdot r_i|^2\}$, whereas recursive DDA filter corresponds to an optimal matched filter $h(t)$. The template estimate in the LMS DDA filter can still be subsumed by $w_k(t) = \gamma_k^{(LMS)}\sqrt{E_b}h(t) + \xi_k^{(LMS)}(t)$, except that the noise term $\xi_k^{(LMS)}(t)$ has non-zero mean due to the bias between $w_o(t)$ and $h(t)$.

5.3.4. Implementations

All these DDA filters rely on decision direction, in which case initialization becomes an imminent issue. Similar to conventional DD methods, initialization is typically accomplished via training or other sub-optimal low-complexity processing. A training based initialization method has been discussed in Section 5.3.1, which can be

TABLE 5.1. Decision directed autocorrelation receivers.

Initialization	$w_1(t) = (1/N)\sum_{n=-(N-1)}^{0} b[n]r_n(t)$, with $\{b[1-N], \ldots, b[0]\}$ known.
Filter output	$y[k] = w_k \cdot r_k$
Bit decision	$\hat{b}[k] = \text{sgn}\{y[k]\}$
Weight updating	sliding-window DDA: $w_{k+1}(t) = \frac{1}{N}\sum_{i=0}^{N-1} \hat{b}[k-i]r_{k-i}(t)$
	recursive DDA: $w_{k+1}(t) = \mu w_k(t) + \hat{b}[k]r_k(t)$
	LMS DDA: $w_{k+1}(t) = w_k(t) + \alpha r_k(t)(\hat{b}[k] - y[k])$

used for other DDA algorithms as well. The adaptive procedures for all three DDA receivers are summarized in Table 5.1.

Among the three DDA receivers, sliding-window DDA has the highest implementation complexity in terms of the number of delay units required. The other two iterative filters have similar hardware complexity, while LMS-based DDA has slightly higher computational load than recursive DDA.

Compared with other UWB receivers, all of the proposed autocorrelators build upon analog delay-and-average units operating at the *symbol rate*. Asymptotically optimal correlation templates capable of sufficient energy capture are constructed without explicit channel estimation and multipath tracking of path gains and delays, nor do they require pilot symbol overhead. In contrast, constructing and implementing a proper correlation template for a RAKE receiver rely on digital operations at an impractical *sub-pulse rate*, as well as computationally-involved channel state information estimation.

5.4. Performance Analysis

In this section, we analyze the proposed adaptive DDA UWB receivers in terms of their steady-state BER performances and algorithm convergence rates. We will first assume that all past decisions are accurate. Such analysis is common for DD methods, and establishes tangible bounds for benchmarking performance in the high SNR region. BER performance in the low SNR region will also be discussed to take into account the effect of incorrect past decisions.

5.4.1. Convergence

Under accurate past decisions, both sliding-window and recursive DDA filters can be written in a unified form after normalization, as follows:

$$w_k(t) = \sqrt{E_b}h(t) + \sigma_\xi[k]\bar{\xi}(t), \tag{5.13}$$

where $\bar{\xi}(t) = \xi_k(t)/\sigma_k$ is the normalized noise term with a fixed PSD $N_o/2$, and $\sigma_\xi[k] = \sigma_k/\gamma_k$. The two filters differ only in $\sigma_\xi^2[k]$, which is given by

$$\sigma_\xi^2[k] = \begin{cases} \dfrac{1}{N}, & \text{sliding-window DDA;} \\ \dfrac{1+\mu^k}{1-\mu^k}\dfrac{1-\mu}{1+\mu}, & \text{recursive DDA.} \end{cases} \tag{5.14}$$

For the adaptive filter in (5.13), its rate of convergence can be evaluated by $\sigma_\epsilon^2[k] := \mathrm{E}\{\epsilon_k^2\}$, which is the mean square value of the filter estimation error $\epsilon_k(t) := w_k(t) - \sqrt{E_b}h(t)$. It is straightforward to show that

$$\sigma_\epsilon^2[k] = \sigma_\xi^2[k](N_o/2)BT_b, \qquad \text{when } 1/B \le T_b. \tag{5.15}$$

Based on (5.14), it is apparent that sliding-window DDA has a fixed error variance across k, which is determined by the sliding window size N. In contrast, the error

variance of recursive DDA drops as k increases, and has a convergence rate of $1/k$ when $\mu = 1$. At the steady state, the filter error variance is proportional to $\tilde{\sigma}_\xi^2 := \lim_{k\to\infty} \mathrm{E}\{\sigma_\xi^2[k]\}$, which equals $1/N$ for sliding-window DDA and $(1-\mu)/(1+\mu)$ for recursive DDA, provided that the channel is time invariant.

It is also possible to analyze the rate of convergence of the LMS DDA filter, and possibly its tracking capability in the presence of time-varying channels [70]. Unfortunately, there is no proper time-varying model for UWB propagation channels, which leaves this topic for future exploration.

5.4.2. BER Performance

To analyze the steady-state BER performance of the proposed adaptive receivers in UWB fading channels, we will use a practical channel model whose structure and parameters are explained in Section 3.2. To provide a general result, we allow the time-window of the correlator to have a flexible length $T_L \leq T_b$, which corresponds to collecting the first arrived L_p ($L_p \leq L$) paths. Correlating the filtered signal waveform $r(t)$ with the self-derived template waveform $w_k(t)$ in (5.13), the decision variable for the k^{th} bit is obtained as

$$y[k] = \int_{iT_b}^{iT_b+T_L} r_k(t) w_k(t) dt = b[k]\theta + z_1 + z_2 + z_3, \tag{5.16}$$

where the first term $b[k]\theta$ in (5.16) is the desired signal term, while z_1, z_2 and z_3 are noise terms, given respectively by

$$\theta = E_b \int_{iT_b}^{iT_b+T_L} h^2(t)dt, \tag{5.17a}$$

$$z_1 = \sqrt{E_b}\tilde{\sigma}_\xi \int_{iT_b}^{iT_b+T_L} h(t)\bar{\xi}(t)dt, \tag{5.17b}$$

$$z_2 = \sqrt{E_b} \int_{iT_b}^{iT_b+T_L} h(t)n(t)dt, \tag{5.17c}$$

$$z_3 = \tilde{\sigma}_\xi \int_{iT_b}^{iT_b+T_L} n(t)\bar{\xi}(t)dt. \tag{5.17d}$$

In order to determine the analytical BER expression for binary PAM signals, we will derive the conditional BER from (5.16) depending on a given realization of the random channel coefficients $\boldsymbol{\alpha} = \{\alpha_0, \cdots, \alpha_{L_{p^{-1}}}\}$. This instantaneous performance will then be integrated over the joint probability density function (pdf) of the random parameters to obtain the average BER.

5.4.2.1. Distribution of $z_1 + z_2 + z_3$

Evaluation of the distribution of the composite noise $z = z_1 + z_2 + z_3$ has been shown to be a complex procedure [41, 58, 71]. The DPSK performance analysis in [58, 71] is not applicable to the new characteristics in this DDA receiver. The performance evaluation in [41] analyzed a very similar scenario as that of this DDA receiver. However, it did not give an easy-to-use solution and its calculation complexity is high. Here we derive a BER expression which can approximately predict the performance reliably while keeping the complexity reasonable.

Because both $\bar{\xi}(t)$ and $n(t)$ are zero-mean Gaussian random processes independent of $h(t)$, the noise terms z_1 and z_2 can be regarded as zero-mean Gaussian random variables. When BT_b is large, the noise product term z_3 can also be well approximated

as a Gaussian random variable for SNR regions of practical interest [38, 41, 58, 71]. The mean value of z_3 is zero when the bandwidth B is an integer of $1/(2T_b)$, as we have assumed in Section 3.2. By using $R_n(T_b) = 0$, it is straightforward to show that all three noise terms are uncorrelated, i.e., $E\{z_1 z_2\} = E\{z_1 z_3\} = E\{z_2 z_3\} = 0$ [38, 41, 58, 71].

By using (5.4) and (5.17), and employing the assumption $B \gg 1/T_L$, the noise variance can be approximately evaluated as [71, 58]

$$\sigma_z^2 \cong \theta \frac{N_o}{2}(1 + \tilde{\sigma}_\xi^2) + BT_L \tilde{\sigma}_\xi^2 N_o^2. \tag{5.18}$$

5.4.2.2. Distribution of θ

Let $R_h(\tau) := \int_0^\tau h^2(t)dt$ denote the channel energy as a function of the integration window length τ. From (5.17a), the effective sample gain θ is given by $\theta = E_b R_h(T_L)$. Focusing on the UWB indoor channel model in [19], we suppose for simplicity that all channel paths arrive separately in time, i.e., there is no pulse overlapping. Under this assumption, the received sample gain θ can be simplified to $\theta = \sum_{l=0}^{L_p-1} E_b \alpha_l^2$. Apparently, it is the sum of squared multipath fading coefficients, which are independent lognormal random variables (RVs). To evaluate the pdf of θ, one needs to find the pdf of a sum of independent lognormal RVs. Although an exact closed-form expression does not exist, there are a number of methods to approximate this pdf. We will apply the Wilkinson's method [34] to approximate the desired pdf of θ.

As mentioned in Section 3.2, the channel coefficient α_l can be modeled as $\alpha_l = \lambda_l \beta_l$, where $\lambda_l \in \{1, -1\}$ and $\beta_l = |\alpha_l|$ is a lognormal RV. Let $\beta_l := |\alpha_l| = e^{u_l}$, where u_l is a normal RV obeying $u_l \sim \mathcal{N}(\mu_{u_l}, \sigma_{u_l}^2)$, and $\theta_l := E_b \alpha_l^2 = e^{c_0 + 2u_l}$, where

$c_0 = \ln(E_b)$. The k^{th} moment of the lognormal variable β_l is then given by

$$E\{\beta_l^k\} = e^{k\mu_{u_l} + k^2\sigma_{u_l}^2/2}. \tag{5.19}$$

According to Wilkinson's method, we let $\theta = \sum_{l=0}^{L_p-1} \theta_l$ be modeled as a lognormal RV, which implies that $\theta = e^x$ and $x \sim \mathcal{N}(\mu_x, \sigma_x^2)$ is a normal RV. The two parameters μ_x and σ_x can be obtained by matching the first two moments of θ with the first two moments of $\sum_{l=0}^{L_p-1} \theta_l$. Algebraic manipulations lead to the mean $\mu_x = \ln(E_{L1}^2/\sqrt{E_{L2}})$ and the variance $\sigma_x = \sqrt{\ln(E_{L2}/E_{L1}^2)}$, where the two scalars E_{L1} and E_{L2} are related to μ_{u_l} and $\sigma_{u_l}^2$ by

$$E_{L1} = \sum_{l=0}^{L_p-1} e^{(c_0 + 2\mu_{u_l} + 2\sigma_{u_l}^2)} \tag{5.20a}$$

$$E_{L2} = \sum_{l=0}^{L_p-1} e^{2(c_0 + 2\mu_{u_l} + 4\sigma_{u_l}^2)} + 2\sum_{l=1}^{L_p-1}\sum_{m=0}^{l-1} e^{2(c_0 + \mu_{u_l} + \mu_{u_m} + \sigma_{u_l}^2 + \sigma_{u_m}^2)}. \tag{5.20b}$$

Putting all together, the pdf of θ is approximated as

$$f(\theta) = \frac{1}{\theta\sqrt{2\pi\sigma_x^2}} exp\left[-\frac{(\ln(\theta) - \mu_x)^2}{2\sigma_x^2}\right]. \tag{5.21}$$

5.4.2.3. Error performance

Conditioned on θ, the BER expression of a binary PAM signal is given by

$$P(\theta) = \frac{1}{\sqrt{2\pi\sigma_z^2}} \int_{-\infty}^{0} exp\left[-\frac{(\lambda - \theta)^2}{2\sigma_z^2}\right] d\lambda = Q\left(\frac{\theta}{\sigma_z}\right) \tag{5.22}$$

where $Q(\cdot)$ is the complementary error function.

The average BER can be calculated by averaging the conditional BER $P(\theta)$ over the probability density function $f(\theta)$ in (7.27) as

$$P_b = \int_0^{\infty} P(\theta) f(\theta) d\theta. \tag{5.23}$$

This BER expression applies to any channel type without necessarily incurring the assumption of no pulse overlapping. In a general case, the pdf $f(\theta)$ should be replaced by the actual channel statistic and can be evaluated via Monte Carlo simulations. Numerical methods can be used to evaluate the BER in (5.23), which provides the performance lower bound under the assumption of perfect past decisions.

5.4.3. Error performance in low SNR region

Albeit fairly accurate at the high SNR region, the BER expression in (5.23) cannot precisely describe the receiver error performance for low SNRs, in which case the number of erroneous past decisions becomes non-trivial. Here we examine the low-SNR case to provide some insight on the receiver performance. Our approach relies on counting the probability of erroneous symbol decisions.

Recall the template estimate $w_k(t)$ in (5.8). When past decisions are in error, the noise term $\xi_k(t)$ in the template remains un-affected, but the estimation efficiency factor γ_k is lowered. Each wrong symbol decision will cause its corresponding waveform to counteract a correctly demodulated waveform. As a result, γ_k should be replaced by $\gamma_k' = (1 - 2P(\theta))\gamma_k$ to accommodate the effect of wrong decisions. It is reasonable to assume that $P(\theta)$ must be less than 50% for a meaningful transmission. Corresponding to (5.13), the low-SNR general expression for $w_k(t)$ can be written as

$$w_k(t) = (1 - 2P(\theta))\sqrt{E_b}h(t) + \sigma_\xi^2[k]\bar{\xi}(t). \tag{5.24}$$

The decision statistic $y[k]$ in (5.16) should be adjusted accordingly. The effective sample amplitude θ should be replaced by $\theta' = (1 - 2P(\theta))\theta$ and the second noise term in (5.17c) replaced by $z_2' = (1-2P(\theta))z_2$, while z_1 and z_3 remain the same. The composite noise variance is now $\sigma_z'^2 \cong \theta(1 - 2P(\theta) + \tilde{\sigma}_\xi^2)(N_o/2) + BT_L\tilde{\sigma}_\xi^2 N_o^2$. Substituting θ' and $\sigma_z'^2$ for θ and σ_z^2 in (5.22), we obtain an expression for $P(\theta)$ in the low SNR region:

$$P(\theta) = Q\left(\frac{\theta'}{\sigma'_z}\right) \tag{5.25}$$
$$= Q\left(\frac{(1-2P(\theta))\theta}{\sqrt{\theta(1-2P(\theta)+\tilde{\sigma}_\xi^2)N_o/2 + BT_L\tilde{\sigma}_\xi^2 N_o^2}}\right).$$

Eq. (5.25) does not immediately lead to a manageable closed-form solution to $P(\theta)$. Nevertheless, some one-dimensional numerical methods may be used to find an approximate solution to $P(\theta)$ given θ. In next section, we compute the BER performance based on the numerical solution to (5.25) and compare it with the analytical result in (5.22) as well as simulation results.

5.5. Numerical Results

In all simulation tests, we use the CM3 model from [19] to generate random UWB channel realizations. The root-mean-square (RMS) channel delay spread is set to 15ns, the average cluster arrival rate is 0.0667/ns, and the average path arrival rate is 2/ns. The cluster and ray decay factors are given by $\Gamma = 14$ns and $\gamma = 7.9$ns, respectively. The standard deviation of the fading coefficients is set to be 3.4dB. There are a total number of $L = 35$ resolvable paths, whose total energy is normalized by $E\{\sum_{l=0}^{L-1} |\alpha_l|^2\} = 1$. A carrier-modulated, truncated root-raised-cosine (RRC) pulse with a roll-off factor of 0.25 is applied as the UWB pulse shape $p(t)$ and the pulse width is set to $T_p = 0.5$ns. The transmission rate $1/T_b$ is selected to be such that channel excess delay does not cause ISI.

Three different receivers are considered: the RAKE receiver with maximum ratio combining (MRC), the transmit-reference (TR) receiver, and the proposed sliding-window DDA receiver with a pilot symbol block of size $N = 16$ for initialization. The DDA receiver may use the signal waveform collected from all paths or just collect part of the received signal energy from the first received L_p paths. In the RAKE receiver,

the number of fingers is set to be 5, which is a reasonable limit imposed by practical receiver cost constraints.

The BER curves of these receivers are plotted in Figs. 5.3, 5.4, and 5.5, with $L_p = 35, 20$ and 5, respectively. Analytical BER curves of the DDA receiver are also included to compare with the simulated curves. In all test cases, the proposed DDA receiver performs better than the TR receiver. The analytical performance of the DDA receiver matches well with its simulated results in high SNR region, except in Fig. 5.5 where $L_p = 5$ is not large enough for the Wilkinson's method [34] to achieve an accurate approximation of the pdf $f(\theta)$. In the low SNR region, as discussed in Section 5.4.3, because the analysis did not take into account erroneous symbol decisions, the analytical BER in (5.22) is lower than the actual value. To accommodate the effect of erroneous symbol decisions in DD, the low-SNR BER expression in (5.25) is evaluated numerically to solve for $P(\theta)$, which is then used in (5.23) to reach the average BER. This low-SNR analytical BER matches well with simulations, as shown in Fig. 5.6.

Due to the noise term in the template waveform, the DDA receiver and the TR receiver perform worse than the RAKE receiver when the same number ($L_p = 5$) of paths are collected, as shown in Fig. 5.5. However, the performance gap between the DDA and the RAKE receiver is small in high SNR region, since the noise effect has been mitigated by the averaging operation in the DDA receiver. As more paths are collected by the receiver (Figs. 5.3-5.4), both DDA and TR receivers outperform the 5-finger RAKE receiver. Note that collecting a large number of signal paths in DDA and TR does not raise implementation costs, as one can simply adjust the correlation time-window length T_L.

DDA receivers collecting different numbers of received paths are compared via simulations in Fig. 5.7. Apparently a receiver collecting more paths offers better BER performance, but the improvement does not increase proportionally because paths ar-

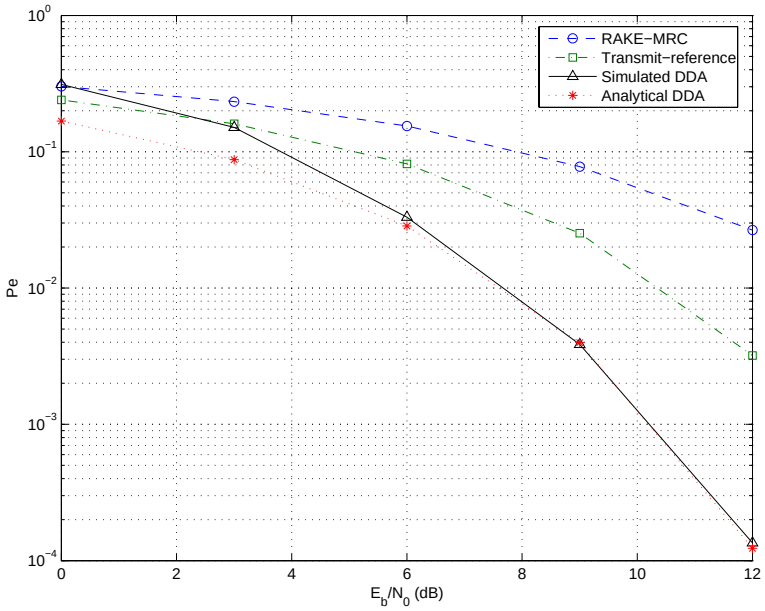

FIGURE 5.3. Analytical and simulated BER versus average received SNR curves using different receiver schemes. L_p is 35 for DDA and TR, 5 for RAKE.

riving earlier typically contain higher energy on average. The memory depth of the DD operation also affects the receiver performance, which is illustrated in Fig. 5.8. As expected, a larger N leads to a more significant reduction in the noise level of the constructed correlation template, which in turn improves the detection performance. In the high SNR region, it is noted that the BER performance can be effectively improved by increasing the number of collected paths L_p, while the improvement diminishes as the memory length N increases.

The sliding-window DDA receiver is compared with recursive DDA and LMS DDA receivers in Fig. 5.9. The latter two receivers are simpler to implement, yet exhibit BER performances comparable to that of sliding-window DDA. When the forgetting factor μ is selected to be larger than $(N-1)/(N+1)$ (based on the filter error variance factor $\tilde{\sigma}_\xi^2$ in (5.14) at the steady state), the recursive DDA has an effective filter memory

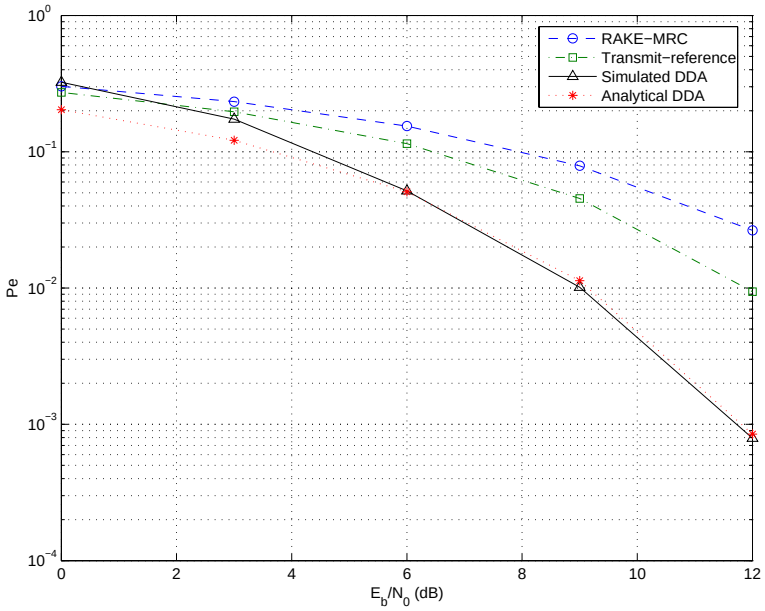

FIGURE 5.4. BER versus SNR for various receiver schemes: L_p is 20 for DDA and TR, 5 for RAKE.

length longer than N, leading to better BER performance than sliding-window DDA at the steady state. In general, a larger μ leads to better steady state performance, but slower convergence. The LMS DDA receiver has slightly worse performance, because it is an adaptive implementation of Wiener filter, which does not take into account the finite-alphabet constraint on symbols $\boldsymbol{v}$.

The analysis and simulations so far have assumed a single-user communication scenario. The DDA receivers are expected to outperform TR schemes in multi-user scenarios as well, since the adaptive template-updating process can also mitigate the effect of multiple-access interference (MAI) on the quality of the template waveform. However, the exact performance of the DDA receiver in a multi-user scenario depends on many factors such as the spreading schemes (time-hopping, direct-sequence, or others) and system parameters. The analytical performance analysis of the proposed schemes

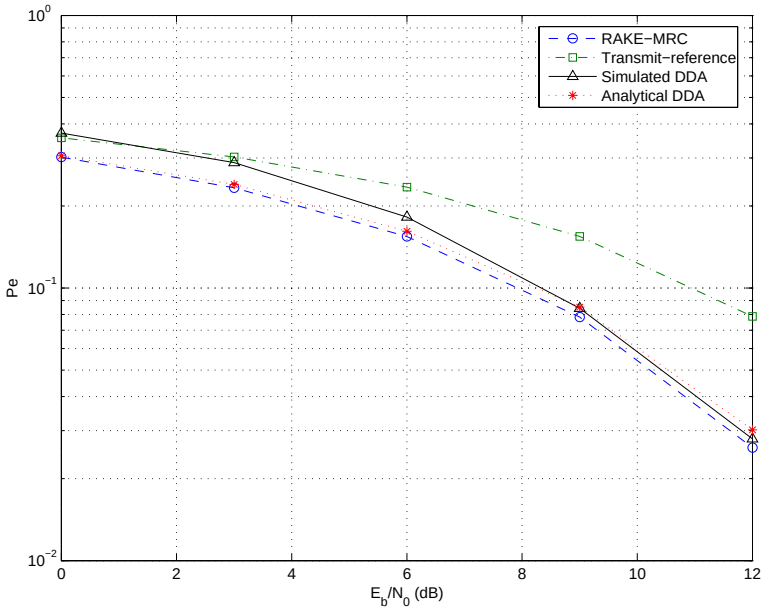

FIGURE 5.5. BER versus SNR for various receiver schemes: L_p = 5 for all schemes.

in a multi-user environment is beyond the scope of this thesis, and is thus left for further investigation. Instead, we provide simulation results to compare the DDA and the TR schemes in a multi-user scenario. Fig. 5.10 shows the BER versus the received signal-to-interference ratio (SIR) curves with different number of interferers. The bit rate is chosen to be 20Mbps and all other parameters are same as previous examples. Although in a multi-user environment an error floor is observed for both the DDA and the TR schemes, the performance advantage of former over the latter is found to be quite significant.

5.6. Algorithm Enhancement via Soft Decoding

The detection performances of DDA receivers depend not only on the noise effect, but also on potential error propagation effect when past decisions are in error.

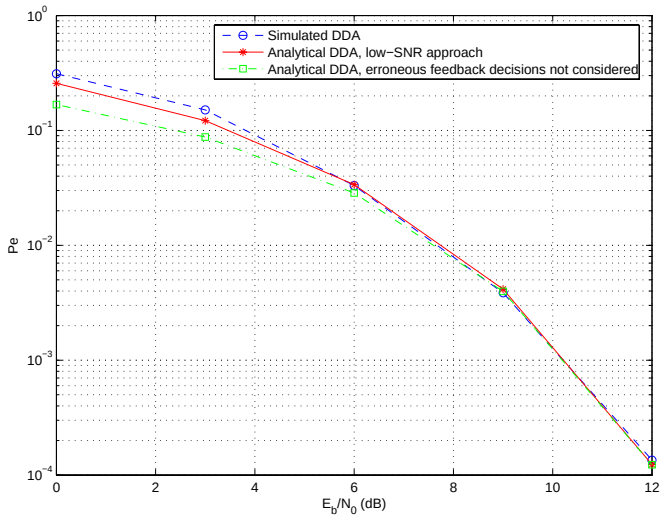

FIGURE 5.6. BER versus SNR curves using the analytical approach given in Sections 5.4.2 and 5.4.3: $L_p = 35$.

For the latter, we employ a soft decoding strategy to mitigate the destructive effect of wrong decisions on the self-derived templates.

Recall the decision process for a binary PAM symbol. The decision statistic $y[k]$ is compared with the threshold 0 to make a hard decision $\hat{b}[k]$ on the corresponding symbol $b[k]$. Replacing $b[k]$ by the binary $\hat{b}[k]$ is termed *hard-decoding* based DDA. The instantaneous decision quality is determined by $|y[k]|$, which is the distance from the observation to the threshold, and is determined by the channel fading and noise experienced. When $|y[k]|$ is closer to 0, the detector is less confident about the decision, indicating a larger chance of making a detection error. However, in a hard-decision scheme, all past decisions affect the template estimate in the same manner, regardless of their different qualities indicated by $|y[k]|$. This degrades the estimation performance when wrong bit decisions occur.

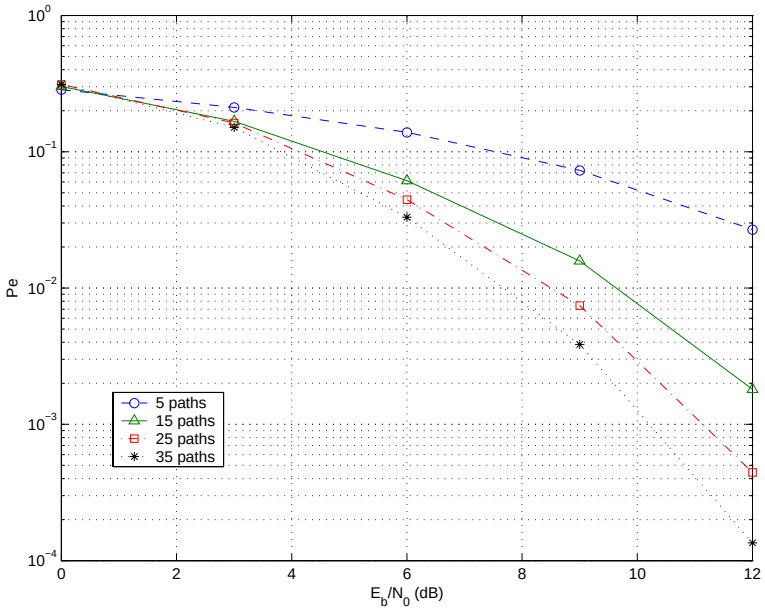

FIGURE 5.7. Simulated BER curves for DDA receiver with different number of collected paths L_p.

To take advantage of the error detection capability provided by $|y[k]|$, we propose a *soft decoding* DDA scheme that is capable of reducing the impact of error-prone symbol decisions. Depending on the confidence level the detector has on a past decision, the contribution of this past symbol to the template estimate will be weighted. The smaller $|y[k]|$ is, the smaller its corresponding weight. Based on this idea, we construct a weighting function $f(|y[k]|)$ that is monotonic in $|y[k]|$. A convenient choice is $f(x) = x$, which leads to a soft-decoding based DDA in the form of

$$w_k(t) = \frac{1}{k}\sum_{i=0}^{k-1} f(|y[i]|)\hat{b}[i]r_i(t) = \frac{1}{k}\sum_{i=0}^{k-1} y[i]r_i(t). \tag{5.26}$$

Because the hard decision $\hat{b}[i]$ is replaced by non-quantized correlator output $y[i]$, a strong and clean symbol waveform will contribute more to the self-derived template waveform than a weak and noisy waveform. Other choices for $f(\cdot)$ are also possible.

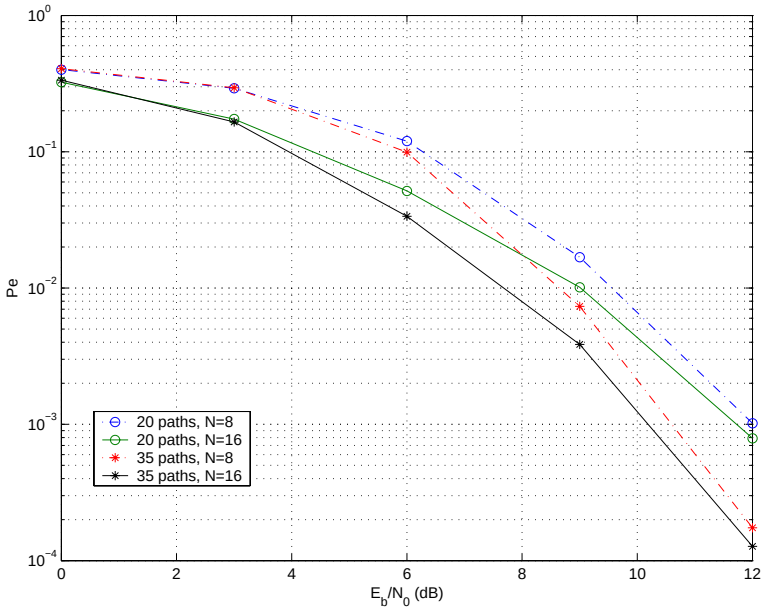

FIGURE 5.8. Simulated BER curves for DDA receiver with different window length N.

When $f(x) = 1, \forall x$, the weighting function is irrespective of the decision quality, and (5.26) reduces to the hard-decision scheme.

Sliding-window based soft-decoding DDA is compared with its hard-decision counterpart in Fig. 5.11, where the channel environment and transmission parameters are the same as those in Section 5.5. A SNR advantage of $0.5 \sim 1$ dB is achieved by employing soft decoding.

5.7. Conclusion

In this chapter, decision-directed autocorrelation receivers are proposed and analyzed for pulsed UWB systems. The advantages and disadvantages of different implementations of the DDA scheme are analyzed and compared. The DDA schemes are

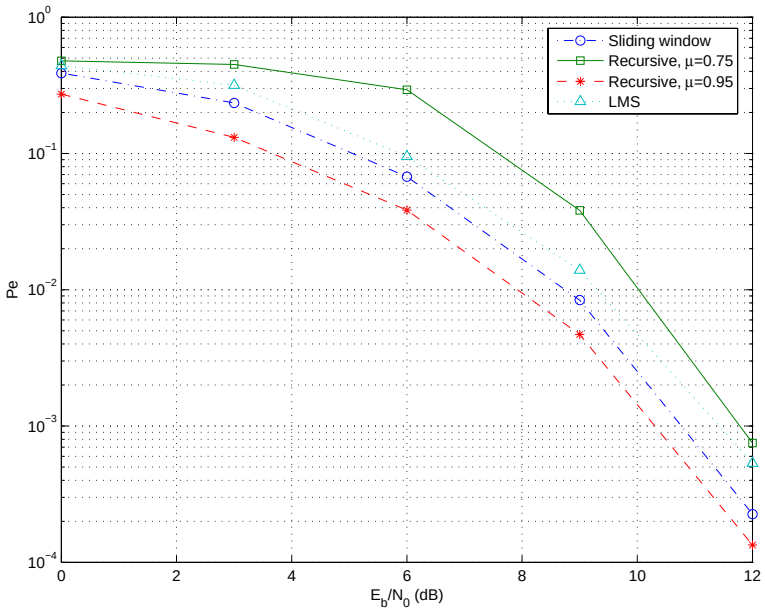

FIGURE 5.9. Performance comparison among all three DDA schemes.

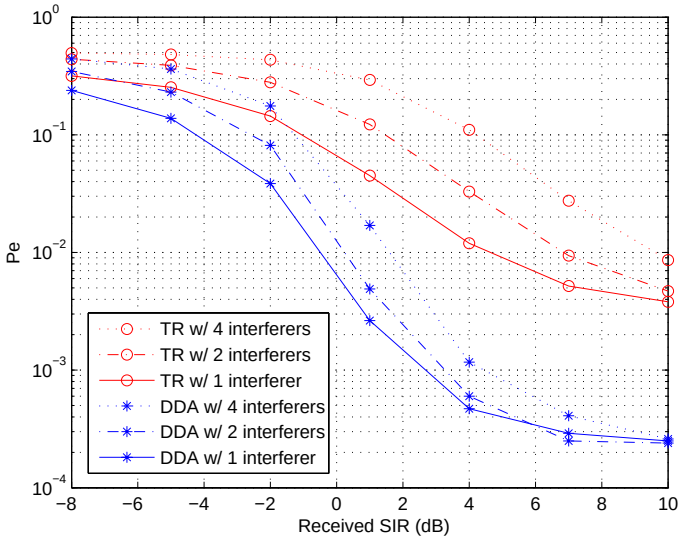

FIGURE 5.10. Performance of DDA and TR receivers in multi-user scenarios: $E_b/N_0 = 12dB$.

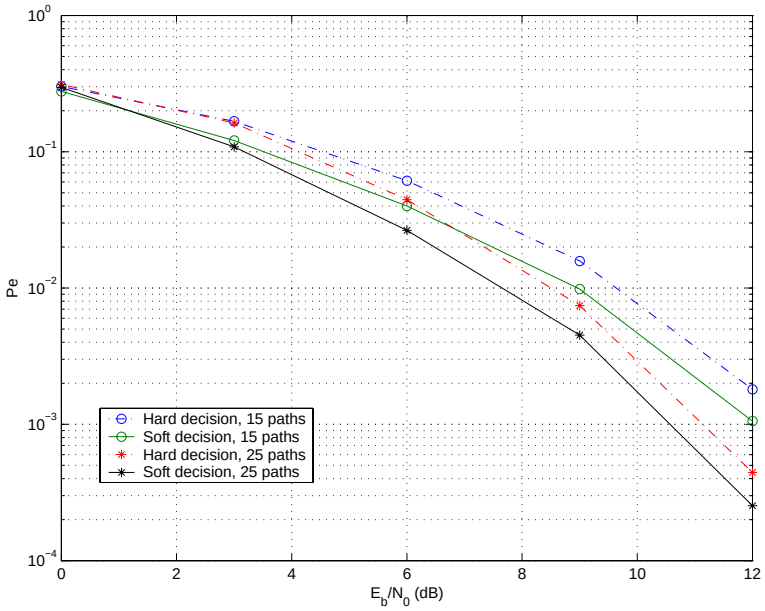

FIGURE 5.11. Performance comparison between the hard decoding and soft decoding DDA schemes.

simple to implement using delay and average units, and incur little training overhead for channel estimation. They are much more effective in capturing multipath energy than practical RAKE receivers, and effectively improve the power efficiency and suppress the noise enhancement effect in the correlation template compared with TR receivers. The detection performance is further improved by a soft decoding approach that takes advantage of the error quality indicator provided by correlator outputs. Confirmed by both analytical error performances and simulation results, the DDA receivers outperform other alternatives, especially in the high SNR region.

6. HYBRID ULTRAWIDEBAND MODULATIONS COMPATIBLE FOR BOTH COHERENT AND TRANSMIT-REFERENCE RECEIVERS

6.1. Introduction

As we have seen in previous chapters, the popular traditional RAKE receiver method faces very high hardware complexity to overcome those technical challenges and achieve the expected high performance when it is applied in typical indoor propagation environments for pulsed UWB systems. This implies a high cost to final products. On the other hand, though TR (autocorrelation) receivers could significantly reduce hardware complexity, they increase transmission overhead, which results in reduced transmission power efficiency; the bit-error-rate (BER) performance is limited by the noise term in the reference signal [38, 41].

Users in a UWB network often have different quality of service (QoS) requirements. It is thus very desirable to enable a heterogeneous network structure, where users can flexibly choose the type of receiver sufficient to achieve their specific QoS targets while minimizing cost. This requires a "universal" modulation method compatible with different types of receivers such as coherent rake and TR receivers. Technically, it is possible to demodulate TR signals with a coherent receiver, by simply "throwing away" the reference pulses. However, this implies a 3dB signal energy penalty compared to a system that is designed to use coherent receivers only. On the other hand, signals designed for coherent receivers (i.e., those without reference pulses) obviously cannot be demodulated by a TR receiver.

We propose a hybrid modulation method that enables coherent rake receivers and TR receivers in the same wireless network to simultaneously receive the signal with high quality. The key idea here is to make the reference pulse information bearing, without modifying the phase relationship between the reference pulse and data

pulse which is critical for the TR receiver operation. This makes sure that the energy in the reference pulse is not wasted for the coherent receiver, and recovers the 3 dB loss by normal TR signaling. Furthermore, we let the information in the reference pulse depend on the *previous* information symbol. Specifically, we let the absolute phase of the reference pulse in the current bit depend on the previous data bit, and the current data bit determines the phase/polarity difference between the reference pulse and the data pulse. This introduces memory into the modulation, which leads to a further performance gain: it is effectively a form of trellis coded modulation (TCM), which enables coherent receivers to achieve better performance than memoryless linear modulation techniques (e.g., bipolar) by taking advantage of this memory through detectors such as a maximum likelihood sequence detector (MLSD). It should be mentioned that the proposed signaling scheme is applicable not only to pulsed UWB systems, but also to narrowband or conventional spread spectrum systems.

The proposed hybrid modulation scheme also offers great advantages when combined further with forward error correction (FEC). The hybrid modulation scheme can be interpreted as a convolutional code with a short constraint length. By viewing FEC combined with hybrid modulation as a form of concatenated coding, this perspective allows us to apply iterative decoding techniques in the receiver, resulting in performance improvements comparable to serially or parallel concatenated coding schemes. A key advantage over serially/parallel concatenated codes is that it does not have the extra complexity or data rate loss caused by the additional FEC code. Still, the design methodology developed for traditional concatenated codes such as turbo codes can be conveniently applied to optimize the design of the constituent encoders [53, 55, 56]. For these purposes, we propose to transform the hybrid modulation, which can be viewed as a non-recursive systematic code, into a recursive code, which is favored by iterative decoding methods. We thus also propose a modified, recursive modulation format,

which will work better by employing iterative decoding and can still be demodulated by TR receivers.

6.2. A Hybrid UWB Transmission Scheme

6.2.1. Basic idea

In the proposed scheme, each bit or symbol is represented by N_f pulse pairs, where N_f is a positive integer. The two pulses in each pair are separated by a fixed unit time T_d. The symbol duration - the time it takes to transmit a bit/symbol - is T_s. Each symbol period is partitioned into N_f frames, each of duration T_f. Each frame is partitioned into N_c chips, each of duration T_c, which typically corresponds to a pulse period. The three quantities T_s, T_f, and T_c satisfy the following relationship:

$$T_s = N_f T_f = N_f N_c T_c. \tag{6.1}$$

Time-hopping (TH) and polarity scrambling are applied on each symbol to obtain processing gain, to combat multiple-access interference (MAI), and to smooth the signal spectrum. Specifically, each pulse pair is delayed by a pseudorandom time [50], and multiplied with a pseudorandom polarity scrambling that can take on the values ± 1 [51]; this can be easily undone at the receiver.

We now consider the mathematical formulation of an arbitrary signal that can be received by a TR receiver. We write this signal in a form that will turn out to be especially suitable for our later discussion:

$$s_{TX}(t) = \sqrt{\frac{E_s}{2N_f}} \sum_{j=-\infty}^{\infty} d_j [\beta_j p(t - jT_f - c_j T_c) + (\overline{\beta_j \oplus b_{\lfloor j/N_f \rfloor}}) p(t - jT_f - c_j T_c - T_d)] \tag{6.2}$$

where b_i is the i-th information bit, $i = \lfloor j/N_f \rfloor$ and $\lfloor \cdot \rfloor$ denotes the integer part. If the system uses an FEC, then $\{b_i\}$ are the outputs of the FEC encoder. An optional polarity

scrambling sequence $d_j \in \pm 1$ can be applied to each pulse pair in the transmitted signal to smooth the signal spectrum. The $c_j \in \{0, 1, ..., N_{TH}\}$ constitutes the j-th entry of the TH sequence for the user under consideration. The TH code must satisfy $N_{TH} < N_c$ and $N_c T_c = N_{TH} T_c + T_d + T_g$, where T_g is a guard time set to protect information signals from inter-frame interference. In order to provide the most general formulation, we have also introduced a polarity encoding β_j. To our knowledge all previous publications on TR set $\beta_j = 1$. E_s is the bit/symbol energy and $p(t)$ is the short-duration UWB pulse shape whose energy is normalized to $E_p = \int_{-\infty}^{\infty} p^2(t)dt = 1$.

As mentioned in the introduction, the key idea of our hybrid modulator is to transmit redundant information on the reference pulses, in other words, to make the β_j dependent on the information symbols:

$$\beta_j = b_{\lfloor j/N_f \rfloor - 1}. \tag{6.3}$$

Fig. 6.1(a) shows a block diagram of the transmitter that realizes the above waveform.

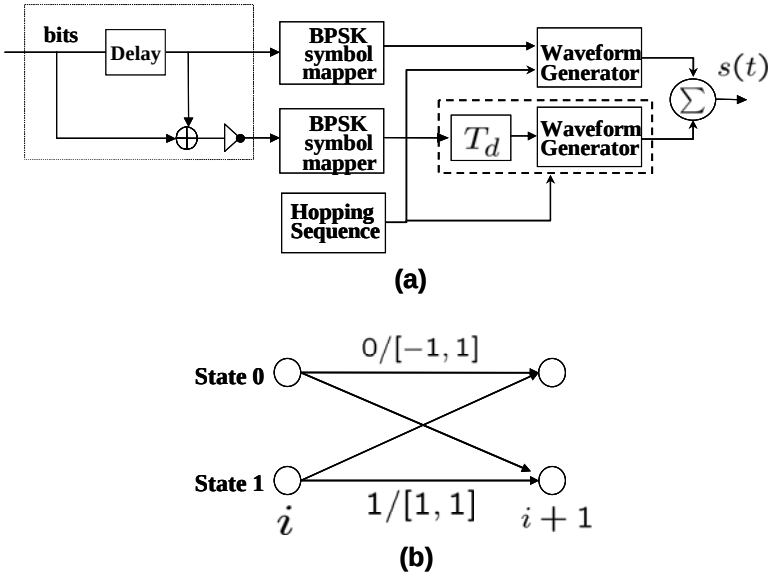

FIGURE 6.1. (a) Block diagram of the hybrid transmitter; (b) Trellis representation of the hybrid modulation.

Table 6.1 shows the four possible combinations of two consecutive bits, the corresponding values of the reference and data waveforms, and their phase differences or polarities. The phase difference between the reference pulse and the data pulse is identical to the conventional TR system.

TABLE 6.1. Input and output combinations of hybrid modulation

Previous bit	Current bit	Reference pulse modulation symbol $b_{\lfloor j/N_f \rfloor - 1}$	Data pulse modulation symbol $\overline{b_{\lfloor j/N_f \rfloor - 1} \oplus b_{\lfloor j/N_f \rfloor}}$	Phase difference between reference pulse and data pulse
0	0	-1	1	180^o
0	1	-1	-1	0^o
1	0	1	-1	180^o
1	1	1	1	0^o

If the current bit is 0, then the phase difference between the reference pulse and the data pulse is always 180^o, regardless of the value of the previous bit. If the current bit is 1, then the phase difference is 0^o. Additionally, the sequence of pairs also contains the information about the previous bit in the polarity of the reference pulse. Again, this is illustrated in Table 6.1, where the reference pulse in each pair has a $+/-$ polarity that indicates the value of the previously encoded bit.

Clearly, a TR receiver can demodulate this transmitted signal. The signal can also be demodulated by a coherent TH receiver with an improved performance compared to the coherent reception of conventional TR signals. The performance gain comes from the fact that information is encoded in both the reference pulses and the data pulses (see Table 6.1). Thus, the coherent TH receiver can take advantage of the memory encoded in the reference pulses to improve performance.

Therefore, this hybrid modulation enables the use of both coherent and TR receivers in the same network. The choice of receiver can be based on considerations such as performance target, implementation cost, and desired radio frequency (RF) coverage area.

6.2.2. Alternative interpretation and receiver structure

In the following, we give another interpretation of the modulation format, which also leads to the proposed receiver structure. During each symbol period, a sequence of N_f pulse pairs is transmitted. The pair in each frame consists of two pulses, each with a polarity depending on the current and previous bits transmitted. There are four possible combinations of pairs:

$$s_0(t) = \alpha(-1 \cdot p(t) + 1 \cdot p(t - T_d)) \tag{6.4a}$$

$$s_1(t) = \alpha(-1 \cdot p(t) - 1 \cdot p(t - T_d)) \tag{6.4b}$$

$$s_2(t) = \alpha(1 \cdot p(t) - 1 \cdot p(t - T_d)) \tag{6.4c}$$

$$s_3(t) = \alpha(1 \cdot p(t) + 1 \cdot p(t - T_d)) \tag{6.4d}$$

where the coefficient $\alpha = \frac{1}{\sqrt{2N_f E_p}}$ with E_p being the energy per pulse and N_f being the number of pulse pairs in a symbol normalizes the energy of the transmitted symbols. These signals can be represented by vectors as

$$s_0 = [-1 \quad 1] \tag{6.5a}$$

$$s_1 = [-1 \ \ -1] \tag{6.5b}$$

$$s_2 = [\ 1 \ \ -1] \tag{6.5c}$$

$$s_3 = [\ 1 \quad 1]. \tag{6.5d}$$

Therefore, the transmitted signal can also be described as follows. During each symbol period, the transmitter transmits a sequence of N_f pairs. The four possible pairs are

given by Eq. (6.4). Optional polarity scrambling could be applied to the pairs to smooth the spectrum.

The above interpretation leads to a new improved coherent receiver structure. It becomes clear that the hybrid scheme provides a modulation format with memory, which can normally be represented by using a trellis diagram. Additionally, the transmitted signals are two-dimensional because two orthogonal basis functions $\Psi_0(t) = \alpha p(t)$ and $\Psi_1(t) = \alpha p(t - T_d)$ are used to represent the pairs.

Fig. 6.1(b) shows the trellis diagram describing the modulation. The trellis has two states, where state '0' represents a previous bit '0', and state '1' represents a previous bit '1'. Branches of the trellis indicate possible transitions. The branches are labeled with the value of the current input bit and the vector representation of the transmitted pair. For example, if the current state is '0' and a bit '1' is to be transmitted, then a transition to state '1' occurs, and pair $s_1 = [-1\ -1]$ is transmitted. A MLSD detector determines the most probable path through the trellis for a given sequence of observations. Methods that approximate the MLSD detector, such as Viterbi decoding [72], can also be used.

Compared with an uncoded BPSK signal, there is a 3dB loss when a coherent receiver is used to demodulate a conventional TR signal, since the reference pulse is non-information bearing and has to be simply "thrown away". If we denote ε as the bit energy, a BPSK signal constellation $\{\pm\sqrt{\varepsilon}\}$ and a conventional TR signal constellation $\{\pm\sqrt{\varepsilon/2}\}$ (ignoring the reference pulse) have Euclidean distances of $d_0 = 2\sqrt{\varepsilon}$ and $d_1 = \sqrt{2\varepsilon}$, respectively. Now let us examine the free Euclidean distance of the trellis shown in Fig. 6.1(b). By viewing the hybrid trellis modulation as a systematic convolutional encoding or a TCM, the minimum Euclidean distance is $\sqrt{d_0^2 + d_1^2} = \sqrt{6\varepsilon}$ between any two signal paths that leave one state and re-enter the same state. This clearly indicates that this trellis modulation not only compensates the 3dB loss due to

reference pulses in TR signaling but also gives an additional coding gain of about 1.76 dB compared with uncoded BPSK signaling. The trellis decoding does not impose a significant complexity increase for demodulation since it is only a very simple two-state trellis.

6.3. Enhanced Hybrid Modulation with Iterative Decoding

6.3.1. Iterative decoding

In practical communication systems, FEC codes are often used before digital modulation. For many applications, one simple FEC encoder may not be powerful enough, and a serial or parallel concatenation of two or more FEC codes with iterative decoding could be used to further improve the error-correction capability at the cost of higher hardware complexity [68, 72].

With only one FEC encoder, the proposed new hybrid scheme allows the implementation of powerful iterative decoding. Because the proposed modulation format already has memory and can be illustrated as a form of TCM, the hybrid modulation itself acts as an inner encoder. By simply adding one FEC code as an outer encoder, we can implement the iterative decoding. Because only one FEC encoder is required, the additional encoding hardware cost is minimal and the effective inner encoding does not reduce the data rate further.

Fig. 6.2 shows the block diagram of the improved encoder and the iterative decoder. In Fig. 6.2(a), information bits are FEC encoded before signal modulation and then passed through an interleaver (e.g., a pseudo-random interleaver) to randomize burst errors in the decoding stage. The iterative decoder consists of an inner decoder and an outer decoder, both are soft-input soft-output (SISO) decoders. A SISO decoder [53] is a four-port device that accepts the reliability information, or the corresponding

probability distributions, of the information and encoded symbols as inputs, and outputs the updated reliability information based on the code constraints.

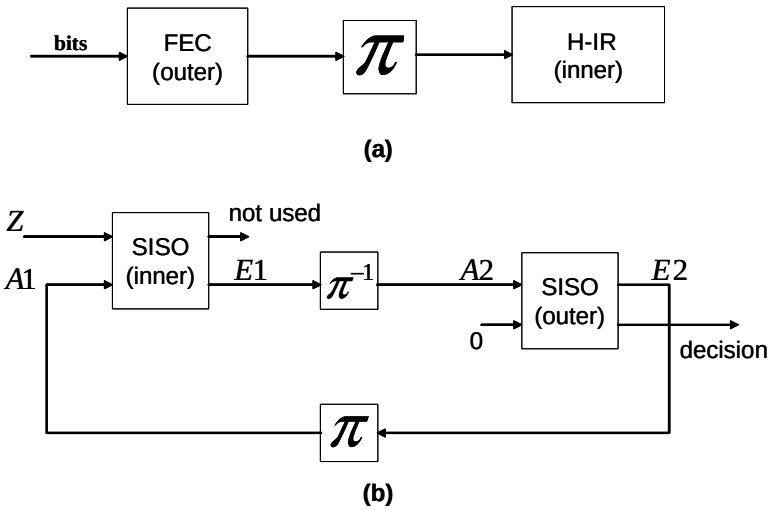

FIGURE 6.2. (a) Modified encoder structure; (b) Iterative decoding structure for hybrid modulation with FEC.

In Fig. 6.2(b), the inner SISO decoder is simply a maximum *a posteriori* probability (MAP) or maximum likelihood (ML) demodulator based on the trellis modulation, which incurs little extra complexity. The soft input of the coded symbol Z comes from the coherent rake detection, and the soft input of the information symbol $A1$ is the de-interleaved feedback from $E2$ at the outer decoder output. A natural reliability value in the binary case, to represent *a posteriori* probability, is the *logarithmic likelihood ratio* (LLR), defined as

$$L(\Delta) \doteq ln \frac{P\{\Delta = +1 | inputs\}}{P\{\Delta = -1 | inputs\}} \tag{6.6}$$

where Δ refers to the decoder output and the word ”inputs” refers to all the decoder inputs.

One example of algorithms for use in the decoders is the modified BCJR algorithm [52, 53]. The rest of the decoding procedure follows the conventional iterative

decoding algorithm of serially concatenated codes [53]. The outer FEC code can be selected according to the desired balance between complexity and performance.

6.3.2. A new recursive modulation

It is well known that recursive systematic convolutional (RSC) codes, when used as inner constituent code in concatenated coding along with iterative decoding, give far better error performance than their nonrecursive counterparts. From the output of the hybrid modulator and its associated trellis shown in Fig. 6.1, one can recognize this as a systematic convolutional encoding, i.e., the current bit/symbol is always present in the polarity of the reference pulse. However, the encoder is nonrecursive.

We therefore introduce a variant of the hybrid modulation of Sec. II that leads to a recursive systematic encoding, and is thus better suited to take advantage of the iterative decoding. This can be achieved by modifying the transmitter shown in Fig. 6.1(a) with the addition of a feedback line from the output of the delay element. The hybrid modulator and the recursive version are shown in Fig. 6.3. The corresponding mathematical formulation, similar to Eq. (6.2), becomes

$$s_{TX}(t) = \sqrt{\frac{E_s}{2N_f}} \sum_{j=-\infty}^{\infty} d_j [b_{\lfloor j/N_f \rfloor} p(t - jT_f - c_j T_c) + \gamma_{\lfloor j/N_f \rfloor} p(t - jT_f - c_j T_c - T_d)] \quad (6.7)$$

Due to the new recursive path, γ is in fact

$$\gamma_{\lfloor j/N_f \rfloor} = b_{\lfloor j/N_f \rfloor} \oplus \gamma_{\lfloor j/N_f \rfloor - 1} \quad (6.8)$$

The modulator shown in Fig. 6.3(b) may be viewed as a new $\frac{1}{2}$-rate convolution encoder described by the generator polynomial [1, $\frac{D}{1+D}$], where the denominator $1 + D$ represents the feedback line. The corresponding new trellis is shown in Fig. 6.4(a). If the two output bits are used to encode the reference and data pulses as described

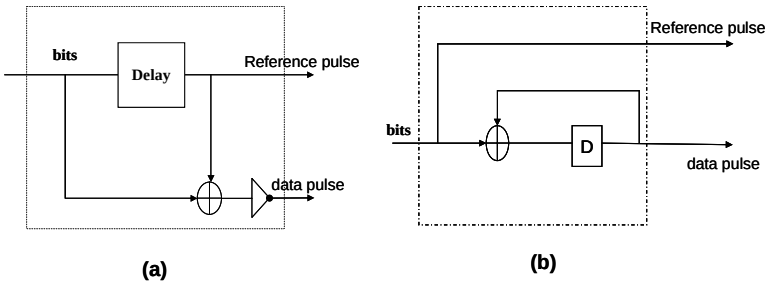

FIGURE 6.3. (a) The basic hybrid modulation; (b) The improved recursive hybrid modulation.

in Section 6.2, apparently a coherent receiver still works as before. Additionally, it achieves the performance gain by using a RSC code as the inner constituent code.

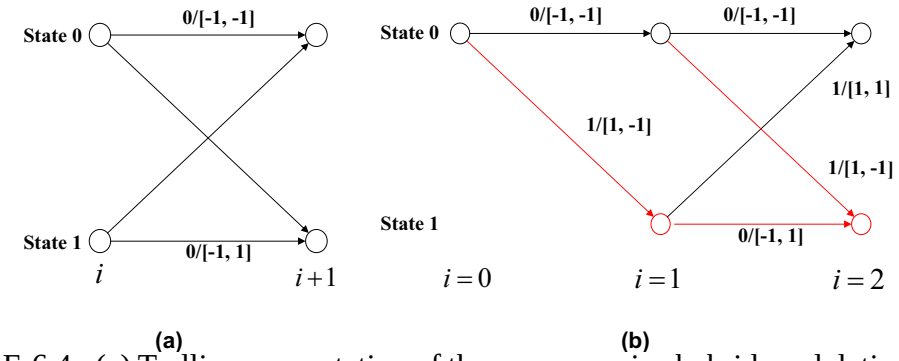

FIGURE 6.4. (a) Trellis representation of the new recursive hybrid modulation; (b) An example on decoding the recursive modulated signals by TR receiver.

When using the recursive version of the hybrid modulation, the phase difference in a pulse pair does not depend on the current input bit anymore. Instead, it only depends on the state transition. At first glance, one might have the impression that consequently, a trellis decoding is needed in the TR receiver. The increased complexity might be undesirable for simple TR receivers. After examining the new trellis in

Fig. 6.4(a), however, we find that we can implement a symbol-by-symbol detection procedure, which does not require a sequence detector.

Fig. 6.4(b) illustrates the decoding procedure. Without loss of generality, we assume that decoding always starts with state '0'. At time $i = 2$, looking at the both branches entering state '0', the phase difference between pulse pairs are found to be the same, indicating that the path selection up to time $i = 1$ solely depends on the phase difference detected at that step. The situation is the same if we look at the branches entering state '1' at time $i = 2$. Thus, there is no need for decoding path memory or trace back. For example, at time $i = 1$, we know the previous state is '0'. Then as long as the phase difference is known to be 0^o or 180^o at time $i = 1$, the transmitted bit can be demodulated as '0' or '1' and the state changes to '0' or '1'. After the state at $i = 1$ is known, then the same procedure is applied to demodulate the next bit, and so on. Although the demodulation depends on the trellis state besides the phase difference in the received pulse pair, a detected phase difference of 180^o always leads to the next state '1', regardless of the previous state. To summarize, there is no error propagation, which has been verified by using simulation, so that sequence detectors are not necessary for TR receivers. The state and pulse combinations are shown in Table 6.2.

Again, the choice of receiver structure can be based on considerations of performance, implementation cost, and the desired RF coverage area.

6.4. EXIT charts of the hybrid modulations

The heart of the iterative decoding procedure is the use of an algorithm, in each component decoder, that computes the *a posteriori* probability of the information symbols, or more generally a reliability value for each information symbol. By the exchange of these reliability information between decoders, each decoder takes redundant

TABLE 6.2. State and pulse combinations of recursive hybrid modulation

Trellis state	Phase difference between previously received pulse pair	Current bit	Phase difference between currently received pulse pair
0	0^o	0	0^o
0	0^o	1	180^o
1	180^o	0	180^o
1	180^o	1	0^o

information which does not originate from itself to improve the decoding correctness. In contrast to the priori channel observation, which is intrinsic to the iterative decoding process, [54] introduced the original concept of *extrinsic information* to identify the generated reliability value which depends on redundant information introduced by the considered constituent code.

Extrinsic information transfer (EXIT) charts provide a visual tool to study the convergence behavior of parallel or serially concatenated codes [55, 56]. The idea is to predict the behavior of the iterative decoder by solely looking at the input/output relations of individual constituent decoders. Mutual information, a quantity that measures the mutual dependence of two variables, is used to describe the flow of extrinsic information through the SISO decoder.

Fig. 6.5 compares the transfer characteristics of different outer FEC codes and inner coded modulation methods. I_{A1} and I_{E1} represent, respectively, the input and output mutual information of the inner modulation, while I_{A2} and I_{E2} represent those of the outer FEC code. For the inner constituent code in a serial concatenation, the output

mutual information I_{E1} can be viewed as a function of the input mutual information I_{A1} and the SNR E_b/N_0: $I_{E1} = F_1(I_{A1}, E_b/N_0)$. For the outer constituent code, I_{E2} only depends on I_{A2} and has no relation with E_b/N_0: $I_{E2} = F_2(I_{A2})$. During the decoding process as shown in Fig. 6.2(b), the extrinsic soft output $E1$ of the inner decoder becomes the *a priori* input $A2$ of the outer decoder, which then feeds back its output $E2$ as *a priori* input $A1$ of the inner decoder. So the axes are swapped for inner and outer codes: for inner modulation, I_{A1} is on the horizontal axis and I_{E1} is on the vertical axis; but for the outer code, the two axes are interchanged. The details about how to read an EXIT chart can be found in [55, 56].

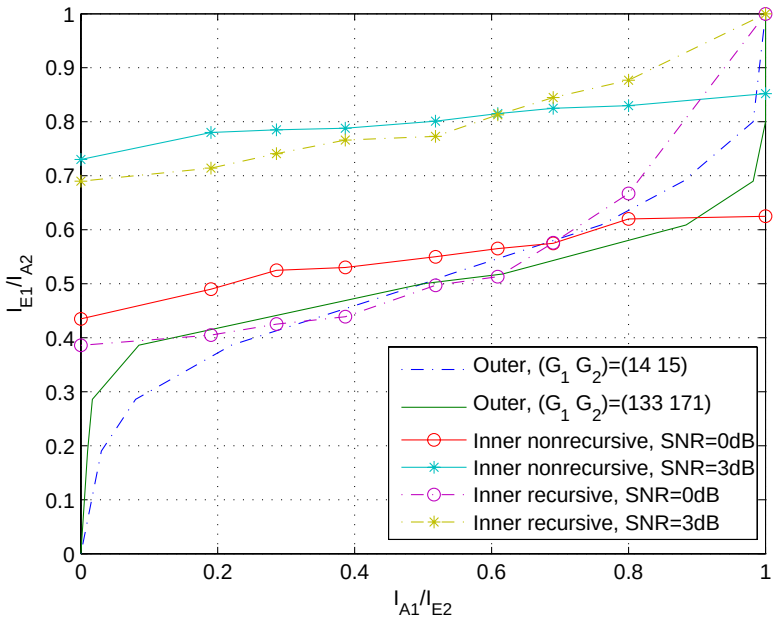

FIGURE 6.5. EXIT chart analysis of hybrid modulation schemes.

In the EXIT chart analysis of the hybrid modulation scheme shown Fig. 6.5, the curves of the outer FEC codes includes two $\frac{1}{2}$-rate convolutional codes of different constraint lengths (CL), which are represented by smooth lines (lines without marks).

One is $CL = 7$ with generator polynomial $(G_1\ G_2) = (133\ 171)$ in octal, and the other is $CL = 4$ with generator polynomial $(G_1\ G_2) = (14\ 15)$. A shorter code memory tends to result in a steeper curve.

On the other hand, the inner modulation methods apparently play a more important role on the iterative decoding performance. Their transfer characteristics at different E_b/N_0 values are shown by lines with marks in Fig. 6.5. The solid lines show the transfer characteristics of the nonrecursive hybrid modulation while the dashed lines show those of the recursive hybrid modulation.

Although the solid lines with marks have higher mutual information at $I_{A1} = 0$, which means better BER after the first round of decoding, they are very flat and do not reach the point $(I_{A1}, I_{E1}) \approx (1, 1)$, which causes convergence problems at low BER after multiple iterations. The flatness of the line also indicates that decoding converges after a few iterations so that many decoding iterations are unnecessary, which will be verified by using simulation results in the next section. At low E_b/N_0 values, the marked dashed line crosses with the curves of the outer codes very early so that the decoding only converges to a point where mutual information is low, resulting in a decoding performance of the recursive modulation that is worse than the solid lines of the nonrecursive modulation. However, at high E_b/N_0 values, the dashed line reaches the point $(I_{A1}, I_{E1}) \approx (1, 1)$ and crosses with the outer codes at a point showing almost perfect mutual information. This indicates a great convergence capability at low BER of the enhanced recursive hybrid modulation with iterative decoding.

6.5. Numerical Results

In this section, we obtain simulation results that compare the different modulation options proposed, as used alone or in combination with a convolutional FEC code.

For comparison, uncoded and convolutionally coded BPSK systems were also simulated under the same channel environment, processing gain, time hopping, and polarity scrambling sequences.

In all simulations, we used a carrier-modulated, truncated root-raised-cosine (RRC) pulse with a roll-off factor 0.25 as the UWB pulse shape $p(t)$ and the 10-dB signal bandwidth is 500MHz. Because signal modulation compatible to both the TR and the coherent rake receivers has attracted significant interests from IEEE 802.15.4a task group (TG), we adopt the channel model from this group [20], which is generated from a large amount of measurements in different communication environments such as residential, office, industry, and outdoor, covering the frequency range from 2GHz to 10GHz. In this chapter, for all simulations over multipath fading channels, the channel impulse response model in non-line-of-sight (NLOS) industrial environments (Channel model 8) from [20] is adopted, since it is the most challenging one due to its large multipath dispersion. Perfect channel knowledge is assumed at the receiver. The chip duration is set at $T_c = 4$ns, and the pulse pair spacing T_d and the guard time T_g are 20ns. The TH sequence is constructed from the algorithm proposed in [57] with $N_{TH} = N_f = 11$ and $T_f = 88$ns.

When a TR receiver is used with the proposed hybrid modulation scheme, the performance is the same as a conventional TR scheme with or without a single FEC code. Since performance of the conventional TR receivers have been analyzed extensively in literature [13, 38, 41, 43, 39, 40, 42], simulation results are presented only for the coherent rake receiver. The rake receiver has 10 fingers to combine 10 strongest paths for each received symbol, and maximal ratio combining (MRC) is employed to collect multipath components.

6.5.1. Hybrid modulation without coding

Firstly, we begin with a simple system which uses hybrid modulation without additional FEC coding. The data rate is set to be 1 Mbps. The rake MRC outputs are fed into a Viterbi detector and demodulated based on the trellis shown in Fig. 6.1(b).

Fig. 6.6 presents the system performance over AWGN channels and compares it with the theoretical performance of BPSK modulated system. The system performance over multipath fading channel is given in Fig. 6.7. For comparison, a BPSK modulated system is simulated with the same set of parameters (channel, processing gain, and time hopping and polarity scrambling sequences). The gain of hybrid modulation method over BPSK modulation is clearly observed.

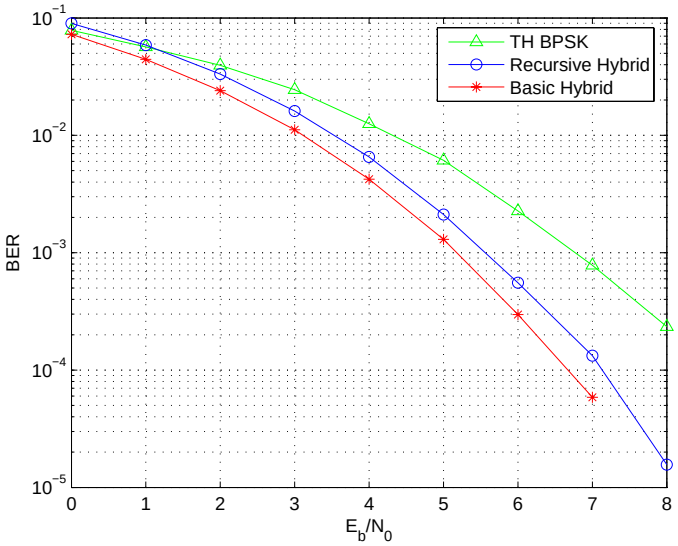

FIGURE 6.6. BER versus SNR curves of uncoded hybrid and BPSK modulation with coherent rake receiver over AWGN channels.

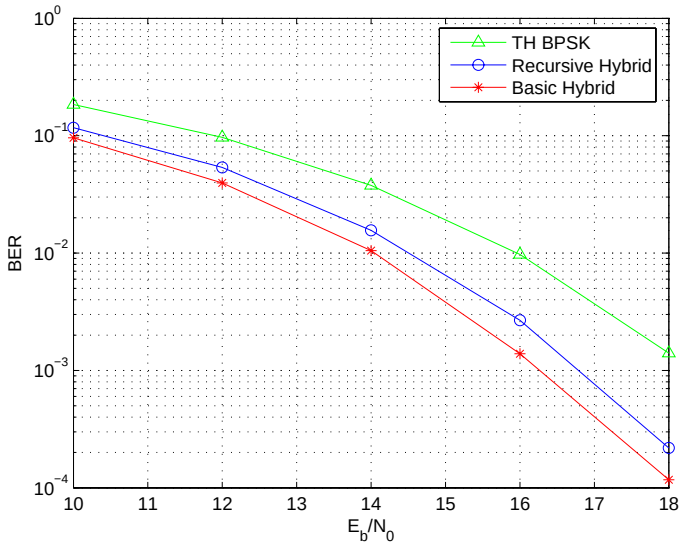

FIGURE 6.7. BER versus SNR curves of uncoded hybrid and BPSK modulation with coherent rake receiver over measured indoor industrial multipath fading channel.

6.5.2. Hybrid modulation concatenated with convolutional encoding

Now we compare different modulation options as they were used in combination with convolutional FEC codes. In these simulations, the data streams are encoded with the $\frac{1}{2}$-rate convolutional code $(G_1\ G_2) = (14\ 15)$, whose extrinsic information transfer characteristic has been shown in Fig. 6.5. The data rate is set to be 1 Mbps after FEC encoding, i.e., a user payload of 500 Kbps, which is a data rate of interest to the 802.15.4a TG. After encoding and random interleaving, the data are fed into the hybrid transmitter.

In this scheme, the rake MRC outputs are fed into the SISO decoder. In the adopted 802.15.4a channel model [20], 100 different channel realizations are given for each channel environment. As suggested by the 802.15.4a task group, in the simulation for each channel environment, 10 data packets of 256 bits/packet were simulated for

each channel realization. Thus the interleaver size between the inner and outer codes is 512 bits.

Error performance curves of the nonrecursive and the recursive hybrid modulation schemes in AWGN environments are shown in Fig. 6.8 and Fig. 6.9, respectively, whereas the corresponding performances in multipath fading environments are shown in Figs. 6.10 and 6.11. We observed that the basic nonrecursive hybrid modulation performs slightly better at the low-SNR region. At the high-SNR (low-BER) region, however, although the nonrecursive hybrid modulation gives better BER after the first round of decoding, the enhanced recursive hybrid modulation improves the system performance drastically after several decoding iterations. Because the interleaver size is limited, the system does not perform exactly as predicted from the EXIT chart shown in Fig. 6.5, which requires a very large interleaver size to achieve its potential. But the basic trend seen from the EXIT chart on decoding performance related to different inner/outer codes and different E_b/N_0 values matches well with the simulation results. Again, a BPSK modulated system and a system using conventional TR signaling are also simulated for comparison, with same FEC encoding, same channel, same processing gain, same time hopping and polarity scrambling sequences. The performance difference between the BPSK system and the hybrid system with no iterative decoding (i.e., after the first iteration) is not as big as the simple systems with no FEC. This is because BPSK demodulation gives more accurate soft output for further FEC decoding than hybrid modulation. However, BPSK systems cannot take advantage of the great power of iterative decoding. The system using conventional TR signaling suffers another 3 dB loss compared to the BPSK system.

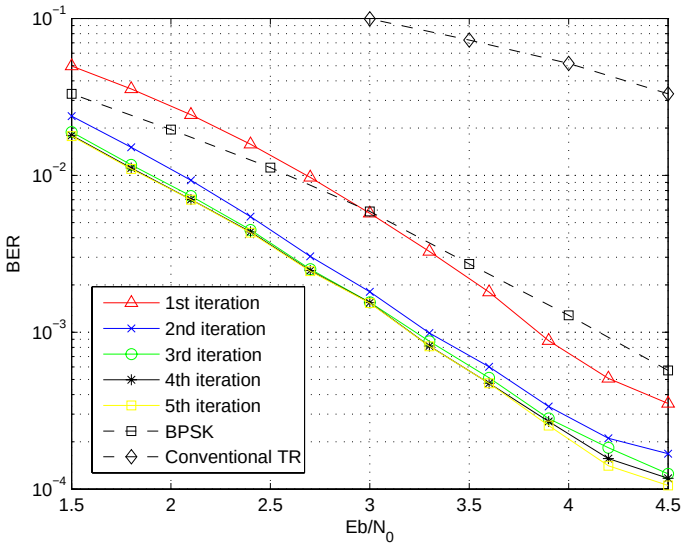

FIGURE 6.8. BER versus SNR curves of the basic hybrid modulation scheme over AWGN channels: coherent receiver with iterative decoding.

6.6. Conclusion

In this chapter, we have proposed a hybrid UWB modulation scheme that allows reception with good quality by both coherent and TR receivers. The key idea is to transmit information about previous information bits on the reference pulses of a TR modulation scheme, thus exploiting the energy contained in the reference pulses for coherent receivers, as well as introducing memory into the system. We then presented an enhanced version by concatenating the hybrid modulation with an FEC code for performance improvements through iterative decoding. Since only one additional FEC encoder is needed for the enhanced hybrid scheme, it adds very little extra hardware complexity to the encoder. We have analyzed the convergence behavior of the proposed enhanced hybrid scheme using the EXIT chart technique, which can also be used to optimize the choices of the constituent codes. Simulation results have shown

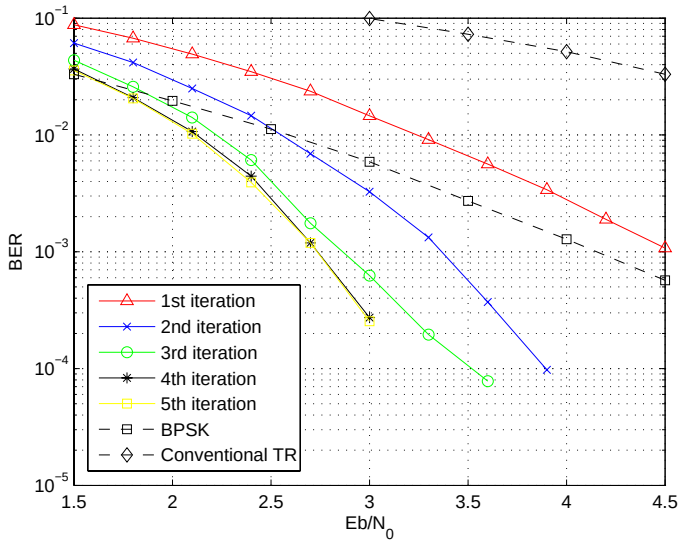

FIGURE 6.9. BER versus SNR curves of the recursive hybrid modulation scheme over AWGN channels: coherent receiver with iterative decoding.

a significant performance improvement by using iterative decoding and the proposed recursive hybrid modulation.

There are three options for receiver designs that work with our basic and recursive schemes, allowing flexible tradeoffs between performance and complexity. The simplest TR receiver can be used for both modulation schemes in the usual way; an FEC encoding provides additional performance improvements. Coherent receivers with iterative decoding are favored for best performance. A compromise between performance and cost might be to use coherent receivers but not to implement iterative decoding. Such design flexibility is highly desirable for heterogenous networks like the ones envisioned for the IEEE 802.15.4a standard; for this reason, our modulation scheme is currently under consideration by this standardization body.

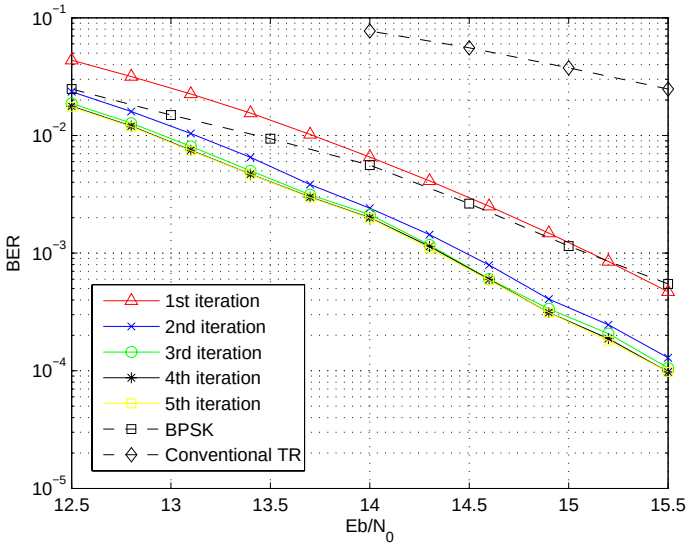

FIGURE 6.10. BER versus SNR curves of the basic hybrid modulation scheme over measured indoor industrial multipath fading channels: coherent receiver with iterative decoding.

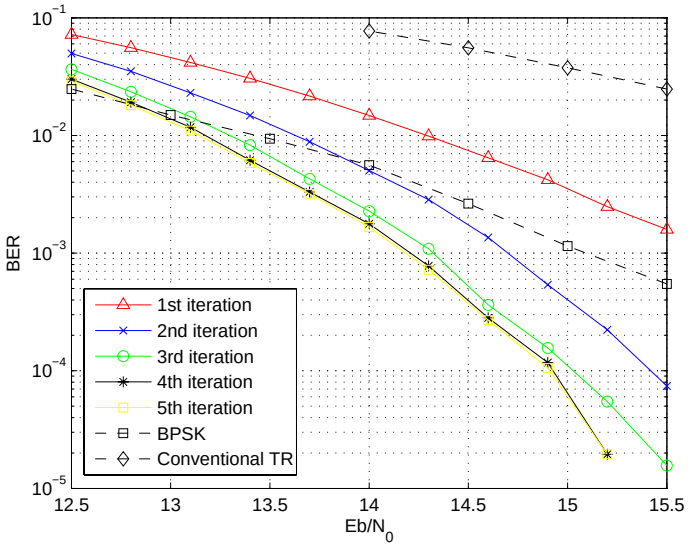

FIGURE 6.11. BER versus SNR curves of the recursive hybrid modulation scheme over measured indoor industrial multipath fading channels: coherent receiver with iterative decoding.

7. TRANSMITTER-SIDE MULTIPATH PREPROCESSING FOR PULSED UWB SYSTEMS CONSIDERING PULSE OVERLAPPING AND NARROW-BAND INTERFERENCE

7.1. Introduction

One of the advantages of pulsed UWB communications is its ability to resolve individual multipath components. This requires a rake receiver to gain path diversity and to capture multipath energy. Multipath combining through a rake [27, 28] requires multipath tracking and channel estimation. However, hardware complexity, power consumption, and system cost scale up significantly with the number of paths combined, which should be avoided for portable or mobile units. Most UWB networks have fixed access points, and it is very desirable if the rake processes can be shifted from the mobile receivers to the transmitter at a fixed access point. As such a shift usually requires channel state information (CSI) in the transmitter, this technique is attractive for systems with time-division duplexing (TDD), where CSI can be easily obtained at both the transmitter and the receiver since both the uplink and the downlink of TDD systems operate in the same frequency band.

For TDD code-division multiple-access (CDMA) systems, a transmit precoding technique was investigated in [59]. This scheme suggests a prerake structure in which pre-delayed signal transmission is employed in the transmitter. This scheme was shown to have comparable performances with the common rake receivers. The prerake scheme has recently been applied to pulsed UWB systems [60], in which the ideal case that received adjacent paths are separated in time by at least one pulse width is assumed. This assumption might be acceptable for communications in line-of-sight (LOS) environments. In non-LOS indoor environments, however, it becomes inappropriate. For example, the typical average multipath arrival rate is in the range of 0.5-2ns [19, 21]

and the typical pulse duration could be as large as 1-4ns [35] for pulses with a 10-dB bandwidth of 500MHz-2GHz. Apparently, for this case severe inter-pulse interference (IPI) could occur. Detection and performance in the presence of IPI were studied in [14, 62, 63]. Besides IPI due to pulse overlapping, co-existing narrow-band radios will interfere with UWB systems. The effects of narrowband interference (NBI) to UWB systems with rake reception have been analyzed extensively [64, 65]. Prerake systems are expected to function differently from the conventional rake receiver in the presence of NBI. Therefore, the conclusions made in existing research on prerake UWB systems need to be re-examined and some optimizations might help to improve performance when pulse overlapping and NBI are taken into consideration. It is worth to note that the time-reversal technique [61] was applied to UWB communications with a very similar idea, though it has a different origin from wideband transmission in underwater acoustic and ultrasound. However, neither IPI nor NBI was considered in [61].

In this chapter we study the structure, optimization, and performance of prerake UWB systems when pulse overlapping and NBI are taken into consideration. Since timing jitter's effect is also often a concern, it is worth to point out that the performance degradation it caused to prerake systems is the same as that to rake systems. Although prerake systems shift the channel estimation to the transmitter side and preprocess the signals there, in the same environment the same level of timing offset will be experienced no matter the timing estimation is done at the transmitter side or the receiver side.

7.2. Transmitter side diversity combining: prerake method

In pulsed UWB systems with binary pulse amplitude modulation, the transmitted signal without prerake processing is expressed as

$$s(t) = \sum_{i=-\infty}^{\infty} s_i(t) = \sum_{i=-\infty}^{\infty} \sqrt{E_b} b(i) p(t - iT_b) \tag{7.1}$$

where $p(t)$ is the short-duration UWB pulse shape of width T_p, E_b is the bit energy, T_b is the bit interval ($T_b \gg T_p$), and $b(i) \in \{1, -1\}$ is the i-th information bit. The energy of the basic pulse $p(t)$ is normalized to $E_p = \int_{-\infty}^{\infty} p^2(t)dt = 1$. $s(t)$ is then transmitted through a frequency-selective lognormal fading channel [19] with additive white Gaussian noise (AWGN).

7.2.1. Prerake model

The concept of prerake diversity combining has been illustrated in [59, 60]. For completeness and for readers' convenience, we summarize the prerake model in this section. We assume that the signaling rate is such that the received signal energy of a particular bit is contained within one pulse repetition interval (T_b) so that there is no inter-symbol interference (ISI). Thus, we can focus on a particular bit interval in the receiver modeling. Corresponding to signal $s_i(t)$ that carries the i-th information bit given in (7.1), the received signal is expressed as

$$r(t) = \sum_{l=0}^{L-1} \alpha_l s_i(t - \tau_l) + n(t) \tag{7.2}$$

where $n(t)$ is the white Gaussian noise process with a two-sided power spectral density of $N_0/2$.

Assuming perfect timing and perfect estimates of channel coefficients and multipath delays, the correlator output of the l-th finger in a generic rake receiver that combines the first L_p ($L_p < L$) paths is expressed as

$$r_l = \sum_{k=0}^{L_p-1} \left(\alpha_k \sqrt{E_b} b(i) \int_{-\infty}^{\infty} p(t - iT_b - \tau_k) p(t - iT_b - \tau_l) dt \right) + n_l, \quad l = 0, 1, \ldots, L_p - 1 \quad (7.3)$$

where the zero-mean noise component is $n_l = \int_{-\infty}^{\infty} n(t) p(t - iT_b - \tau_l) dt$ with variance $\sigma_{n_l}^2 = N_0/2$. When $|\tau_j - \tau_i| < T_p$, $i, j \in \{0, 1, \ldots, L-1\}$, the i-th and the j-th received pulses overlap with each other and IPI occurs. For the ideal (nonrealistic) case when $|\tau_j - \tau_i| > T_p$, $i, j \in \{0, 1, \ldots, L-1\}$, received pulses do not overlap. Thus, all terms with $k \neq l$ in Eq. (7.3) equal zero, and r_l simplifies to

$$r_l = \alpha_l \sqrt{E_b} b(i) + n_l, \;\; l = 0, 1, \ldots, L_p - 1 \quad (7.4)$$

where noise components $n_l, l = 0, \cdots, L_p - 1$, are mutually independent.

In rake systems with linear combining, the decision variable is derived based on the outputs of the L_p rake fingers. Let $\boldsymbol{r} = [r_0, \; r_1, \; \ldots, \; r_{L_p-1}]^T$ (where $(\cdot)^T$ denotes transpose), $\boldsymbol{\alpha} = [\alpha_0, \; \alpha_1, \; \ldots, \; \alpha_{L_p-1}]^T$, and $\boldsymbol{\omega} = [\omega_0, \; \omega_1, \; \cdots, \; \omega_{L_p-1}]^T$ be the tap weight vector for linear combining. The decision variable is expressed as $\Delta = \boldsymbol{\omega}^T \boldsymbol{r}$. It is well known that maximal ratio combining (MRC) is optimum when the desired signal is distorted only by AWGN. The MRC weights that maximize the output signal-to-noise ratio (SNR) are written as $\boldsymbol{\omega} = \boldsymbol{\alpha}^* = [\alpha_0, \; \alpha_1, \; \ldots, \; \alpha_{L_p-1}]^H$, where $(\cdot)^*$ denotes complex conjugate and $(\cdot)^H$ denotes Hermitian transpose.

In prerake systems, L_p pulses each scaled and delayed based on the multipath coefficients and delays are transmitted in each bit interval. The channel acts as a filter and convolves with the transmitted pulses. The scaling coefficients and relative delays are controlled such that the output peak of the correlator in the receiver is equivalent to the output of a conventional rake with MRC. This scheme is illustrated in Fig 7.1. Note that in the prerake system, the receiver requires only one correlator and does not need to perform channel estimation and multipath tracking.

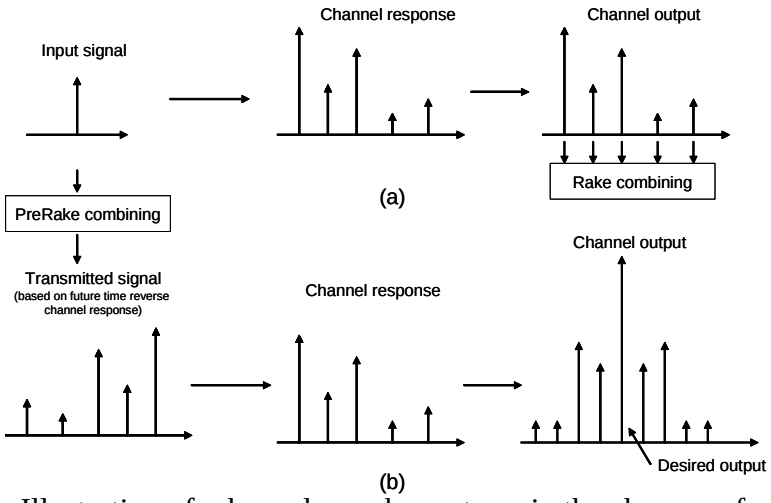

FIGURE 7.1. Illustration of rake and prerake systems in the absence of pulse overlapping: (a) rake diversity combining; (b) prerake diversity combining.

Different from Eq. (7.1) for conventional rake systems, the transmitted signal (again, only the signal in the i-th bit interval is modeled) in a prerake system is expressed as

$$s_i^{'}(t) = \sqrt{\frac{1}{\kappa}} \sum_{l=0}^{L_p-1} \alpha_{L_p-1-l}^{*} s_i(t-\tau_l) \tag{7.5}$$

where $\kappa = \boldsymbol{\alpha}^H \boldsymbol{\alpha}$ is a power normalization factor. After passing through the frequency-selective fading channel described by (5.2), $s_i^{'}(t)$ arrives at the receiver as

$$r'(t) = \sqrt{\frac{E_b}{\kappa}} b(i) \sum_{l=0}^{L_p-1} \alpha_{L_p-1-l}^{*} \sum_{k=0}^{L-1} \alpha_k p(t - iT_b - \tau_l - \tau_k) + n(t). \tag{7.6}$$

The receiver uses only the strongest path[1] to detect the i-th bit. The correlator output is expressed as

$$\Delta^{'} = \int_{-\infty}^{\infty} r'(t) p(t - iT_b - \tau_{L_p-1}) dt. \tag{7.7}$$

---

[1]The L_p-th path whose delay relative to the first-arriving path is τ_{L_p-1}.

In the absence of pulse overlapping, $\Delta^{'}$ simplifies to

$$\Delta^{'} = \sqrt{\frac{E_b}{\kappa}} b(i) \sum_{l=0}^{L_p-1} \alpha_l^* \alpha_l + n^{'} \tag{7.8}$$

where the zero-mean noise component $n^{'} = \int_{-\infty}^{\infty} n(t)p(t-iT_b-\tau_{L_p-1})dt$ has a variance of $N_0/2$.

Let us examine the output SNR of the rake and prerake systems. For the conventional rake system, let $\boldsymbol{n} = [n_0, n_1, \cdots, n_{L_p-1}]^T$ be the noise vector. The instantaneous output SNR of the rake combiner is $\psi_{rake} = \frac{(\boldsymbol{\alpha}^H\boldsymbol{\alpha})^2 E_b}{2E\{(\boldsymbol{\alpha}^H\boldsymbol{n})^H(\boldsymbol{\alpha}^H\boldsymbol{n})\}}$, where $E\{(\boldsymbol{\alpha}^H\boldsymbol{n})^H(\boldsymbol{\alpha}^H\boldsymbol{n})\} = \boldsymbol{\alpha}^H\boldsymbol{\alpha}E\{\boldsymbol{n}^H\boldsymbol{n}\} = \boldsymbol{\alpha}^H\boldsymbol{\alpha}N_0/2$. In the receiver of the prerake system, the output signal energy is $\frac{(\boldsymbol{\alpha}^H\boldsymbol{\alpha})^2 E_b}{\kappa} = (\boldsymbol{\alpha}^H\boldsymbol{\alpha})E_b$. Because there is no such a multipath combining process like a rake system, $E\{n'^* n'\} = N_0/2$. Although not all the signal energy in the received multipath components are collected (only the strongest path is collected), the total noise energy also scales down accordingly. The output SNR of prerake systems is $\psi = \frac{E_b(\boldsymbol{\alpha}^H\boldsymbol{\alpha})}{N_0}$, which is equal to ψ_{rake}. Moreover, the diversity orders of the rake and prerake systems are the same. Consequently, both schemes have the same performance, which will be verified by simulation in Section 7.6.

7.3. Prerake optimization in the presence of pulse overlapping

Since pulse overlapping causes inter-pulse interference, Eqs. (7.4) and (7.8) do not hold true anymore. Following the notation used in [14], we define the partial correlation between $p(t-\tau_k)$ and $p(t-\tau_l)$ as $\rho_{l,k} = \int_{-\infty}^{\infty} p(t-\tau_l)p(t-\tau_k)dt = \rho_{k,l}$. Since the energy of $p(t)$ is normalized to unity, $\rho_{l,k} = 1$ for $l = k$ and $0 \leq |\rho_{l,k}| < 1$ for $l \neq k$. Note that $\rho_{l,k} = 0$ if $p(t-\tau_k)$ and $p(t-\tau_l)$ are mutually orthogonal or do not overlap with each other.

For rake receivers derived from the signal model given in (7.3), the received signal vector becomes

$$\boldsymbol{r} = \sqrt{E_b} b(i) \boldsymbol{R} \boldsymbol{\alpha} + \boldsymbol{n} \tag{7.9}$$

where

$$\boldsymbol{R} = \begin{bmatrix} 1 & \rho_{0,1} & \cdots & \rho_{0,L_p-1} \\ \rho_{1,0} & 1 & \cdots & \rho_{1,L_p-1} \\ \vdots & \vdots & \ddots & \vdots \\ \rho_{L_p-1,0} & \rho_{L_p-1,1} & \cdots & 1 \end{bmatrix} \tag{7.10}$$

is the partial correlation matrix, which can be calculated using the relative multipath delays τ_l and the pulse shape $p(t)$. Thus, the zero-mean noise components at the output of different receiver fingers are not independent anymore, and the covariance matrix of $\boldsymbol{n}$ (zero mean) is obtained to be $E\{\boldsymbol{n}\boldsymbol{n}^H\} = \boldsymbol{R}\frac{N_0}{2}$. The decision variable is still $\Delta = \boldsymbol{\omega}^T \boldsymbol{r}$, where the optimum selection of $\boldsymbol{\omega}$ has been discussed in [14]. Note that in the model given by Eqs. (7.9) and (7.10), the effect due to the potential overlap from statistically weaker paths $L_p, \cdots, L$ has been neglected.

In the absence of pulse overlapping, it should be mentioned that the ideal case shown in Fig. 7.1 must be modified accordingly. Due to IPI and the non-uniform time intervals between different multipath components, the appearance of the channel outputs at the receiver frontend as shown in Fig. 7.2 is very different from that shown in Fig. 7.1. However, the desired output signal components at the correlation peak are the same for both cases.

Because of the noise correlation and the additional distortion to received signals caused by IPI besides AWGN, prerake schemes designed according to the MRC rule may not be optimum. For prerake systems, we define the scaling factor for pulses

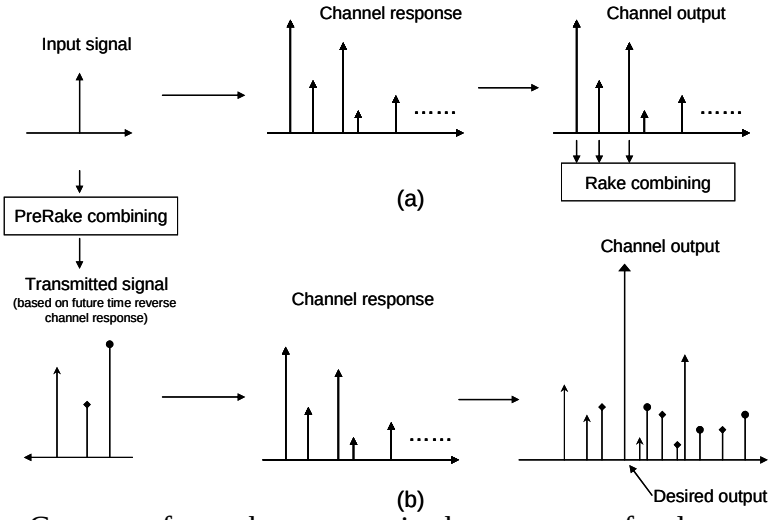

FIGURE 7.2. Concept of prerake systems in the presence of pulse overlapping: (a) rake diversity combining; (b) prerake diversity combining.

constituting $s'_i(t)$ as $\boldsymbol{w} = [w_0,\ w_1,\ \cdots,\ w_{L_p-1}]^T$. Thus $s'_i(t)$ is re-written as

$$s_i^{'}(t) = \sqrt{\frac{1}{\kappa}} \sum_{l=0}^{L_p-1} \boldsymbol{w}_{L_p-1-l} s_i(t-\tau_l) \tag{7.11}$$

where the power normalization factor becomes $\kappa = \boldsymbol{w}^H \boldsymbol{R} \boldsymbol{w}$. Correspondingly, Eq. (7.8) becomes

$$\Delta^{'} = \sqrt{\frac{E_b}{\kappa}} b(i) \boldsymbol{w}^T \boldsymbol{R} \boldsymbol{\alpha} + n^{'}. \tag{7.12}$$

7.3.1. Zero-forcing optimization

From (7.12), a natural choice of the prerake weight vector $\boldsymbol{w}$ to overcome the effect of IPI is to apply the zero forcing (ZF) scheme, which yields a weight vector

$$\boldsymbol{w}^T = \boldsymbol{\alpha}^H \boldsymbol{R}^{-1} \tag{7.13}$$

where the matrix inversion always exists since $\boldsymbol{R}$ is a positive definite Hermitian matrix. With the ZF prerake combining weight, $\boldsymbol{w}^T\boldsymbol{R}\boldsymbol{\alpha} = \boldsymbol{\alpha}^H\boldsymbol{\alpha}$, and IPI is completely removed in the received signal.

It is well known that applying a ZF filter to remove interference in a rake receiver will enhance the additive noise. For prerake combining, since the ZF filtering is done at the transmitter, there is no noise enhancement. However, applying the ZF combining weight $\boldsymbol{w}$ in prerake systems increases the power normalization factor κ, except when $\boldsymbol{R}$ is an identity matrix (no pulse overlapping). This will effectively lower the received SNR as the average transmitted signal power is kept constant.

7.3.2. Maximization of the received SNR based on eigenanalysis

The optimum diversity combining in the sense of maximizing the received SNR in a prerake system is to find $\boldsymbol{w}$ that maximizes ψ. We assume a quasi-static fading model for which the channel fading coefficients and relative path delays are static over a block of data. Next, we apply the eigenanalysis method to maximize the instantaneous SNR in each block to achieve optimum system performance.

As easily seen from Eq. (7.12), now the correlator output SNR of a prerake system in the presence of IPI becomes $\psi = \frac{E_b\boldsymbol{w}^T\boldsymbol{R}\boldsymbol{\alpha}\boldsymbol{\alpha}^H\boldsymbol{R}^H\boldsymbol{w}^*}{\kappa N_0}$. Maximizing ψ is equivalent to maximizing $\psi' = \frac{\boldsymbol{w}^T\boldsymbol{R}\boldsymbol{\alpha}\boldsymbol{\alpha}^H\boldsymbol{R}^H\boldsymbol{w}^*}{\kappa} = \frac{\boldsymbol{w}^T\boldsymbol{R}\boldsymbol{\alpha}\boldsymbol{\alpha}^H\boldsymbol{R}^H\boldsymbol{w}^*}{\boldsymbol{w}^T\boldsymbol{R}\boldsymbol{w}^*}$. From Eq. (7.10), we know that matrix $\boldsymbol{R}$ is Hermitian and positive definite. By using Cholesky factorization, $\boldsymbol{R}$ can be expressed as $\boldsymbol{R} = \boldsymbol{M}^H\boldsymbol{M}$. If we define a new vector $\boldsymbol{u} = \boldsymbol{M}\boldsymbol{w}^*$, ψ' can be re-written as $\frac{\boldsymbol{u}^H\boldsymbol{M}\boldsymbol{\alpha}\boldsymbol{\alpha}^H\boldsymbol{M}^H\boldsymbol{u}}{\boldsymbol{u}^H\boldsymbol{u}}$. From the minimax theorem in eigenanalysis [70], the optimum prerake combining vector

$$\boldsymbol{u} = \underset{\boldsymbol{u}}{argmax}\left\{\frac{\boldsymbol{u}^H\boldsymbol{M}\boldsymbol{\alpha}\boldsymbol{\alpha}^H\boldsymbol{M}^H\boldsymbol{u}}{\boldsymbol{u}^H\boldsymbol{u}}\right\} \tag{7.14}$$

is the principal eigen vector (the eigen vector corresponding to the largest eigen value) of $\boldsymbol{M}\boldsymbol{\alpha}\boldsymbol{\alpha}^H\boldsymbol{M}^H$. Because $\boldsymbol{M}\boldsymbol{\alpha}\boldsymbol{\alpha}^H\boldsymbol{M}^H = \boldsymbol{M}\boldsymbol{\alpha}(\boldsymbol{M}\boldsymbol{\alpha})^H$ is formed from a single column vector $\boldsymbol{M}\boldsymbol{\alpha}$, it is of only rank 1 with only one non-zero eigen value corresponding to the principal eigen vector $\boldsymbol{v} = \boldsymbol{M}\boldsymbol{\alpha}$. We let $\boldsymbol{u} = \boldsymbol{v}$, which apparently leads to the conclusion that $\boldsymbol{w} = \boldsymbol{\alpha}^*$. This implies that, interesting although unexpected, even in the presence of IPI, MRC is still the optimum linear prerake diversity combining scheme. This choice of the prerake combining weight results in the same error performance as a conventional rake receiver with MRC when IPI is present.

7.4. The Effects of Narrow-Band Interference

Prerake and rake systems may perform differently in the presence of narrow-band interference. This is because the receiver of a prerake system takes only one sample per bit for detection whereas the receiver of a rake system needs L_p samples. For simplicity, we consider the case that there is only one NBI source. The observations drawn from this case are applicable to the scenario of multiple independent NBI sources. Let $I(t)$ represent the interference signal. The correlator output for the i-th information bit of a prerake system when NBI is present is modified as

$$\Delta' = \sqrt{\frac{E_b}{\kappa}} b(i)\boldsymbol{w}^T\boldsymbol{R}\boldsymbol{\alpha} + n' + I' = \Delta'_S + \Delta'_N + \Delta'_I \tag{7.15}$$

where $I' = \int_{-\infty}^{\infty} I(t)p(t - iT_b - \tau_{L_p-1})dt$.

The narrowband interference does not change the weight selection for prerake diversity combining. For the ZF optimization, noises are not taken into consideration. For the eigenanalysis-based SNR maximization, the instantaneous SNR must be modified as $\psi = \frac{E_b\boldsymbol{w}^T\boldsymbol{R}\boldsymbol{\alpha}\boldsymbol{\alpha}^H\boldsymbol{R}^H\boldsymbol{w}^*}{\kappa(N_0+E_I)}$, where E_I is the instantaneous NBI energy collected by the receiver. Since E_I is independent of the weight vector $\boldsymbol{w}$, NBI does not change the weight optimization process for prerake multipath diversity combining.

As concluded in Section 7.3, rake and prerake systems with MRC have the same error performance when only AWGN is present. However, the NBI terms in the decision variables of rake and prerake receivers have different distributions, which may result in different error performances for the two schemes. Let us examine the NBI terms in the decision variables for rake and prerake schemes. When NBI is present, the combiner output of a common rake receiver given in (7.15) must be modified as

$$\Delta = \sqrt{E_b} b(i) \boldsymbol{w}^T \boldsymbol{R} \boldsymbol{\alpha} + \sum_{l=0}^{L_p-1} w_l n_l + \sum_{l=0}^{L_p-1} w_l I_l = \Delta_S + \Delta_N + \Delta_I \tag{7.16}$$

where $I_l = \int_{-\infty}^{\infty} I(t) p(t - iT_b - \tau_l) dt$. To make the comparison fair, fading, AWGN, and NBI experienced by both the rake and prerake systems must be kept the same. For all practical scenarios, the time-span of the L_p paths is much shorter than the coherence time of the narrowband interference waveforms. It is thus reasonable to assume that $I_l \approx I',\ l = 0, \cdots, L_p - 1$. For prerake systems, NBI experienced by the receiver only depends on NBI $I(t)$ and UWB pulse shape $p(t)$, as clearly seen from I' defined in (7.15). For rake systems, the elements of the multipath combining $\boldsymbol{\omega}$ (equals $\boldsymbol{\alpha}^*$ if MRC is adopted) are random variables. Therefore, as clearly seen from (7.16), besides $I(t)$ and $p(t)$, the distribution of NBI experienced by the receiver also depends on the distribution of $\sum_{l=0}^{L_p-1} \omega_l$.

These differences are illustrated via simulations where NBI is generated following the specification given in [66, 67]. In this paper two kinds of narrow-band interferers are considered: one is a generic in-band modulated interferer which uses BPSK modulation and uses root raised cosine (RRC) baseband waveform of 5 MHz with roll factor of 0.25; the other one is a generic in-band tone interferer. For simplicity and without loss of generality, the multipath channel is normalized as $E\left\{\sum_{l=0}^{L_p-1} |\alpha_l|^2\right\} = 1$ so that E_b/N_0 equals to the average received SNR. Fig. 7.3 shows the distribution of NBI experienced by a rake and a prerake system as a tone interferer is present. The case with

a modulated interferer is shown in Fig. 7.4. In both cases the NBI signal power is set as 6 dB stronger than the data signal in the received power. The details on the data signal generation will be given in Section 7.6. In the both figures we can see that the NBI experienced by the rake and prerake systems show different distribution characteristics and apparently the difference will lead to different performances of these schemes in the presence of NBI. Nevertheless, it is hard to anticipate how the performance will be different by only looking at the distribution. Performance analysis and system simulations were carried out to evaluate and will be discussed in next two sections.

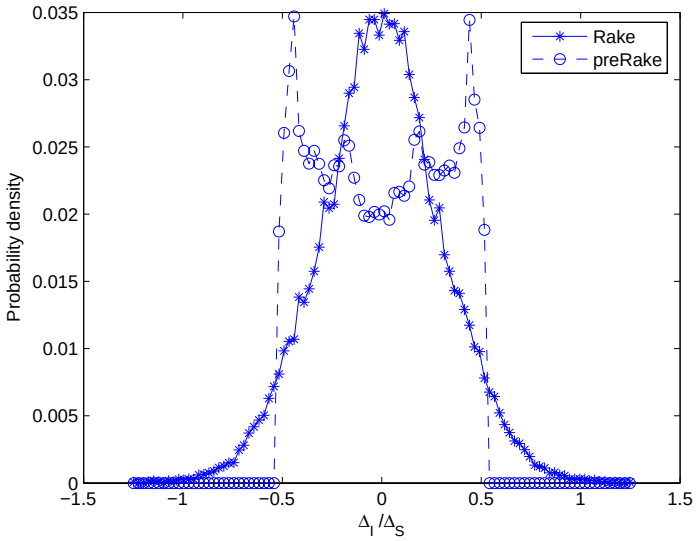

FIGURE 7.3. Distributions of NBI experienced by prerake and rake systems as in-band tone interferer is present.

7.5. Performance Analysis

In this section, we analyze the BER performances of both rake and prerake systems in the scenario of NBI. Due to the complexity as IPI is involved, we only derive an lower bound of the BER which is the optimum case where no IPI happens.

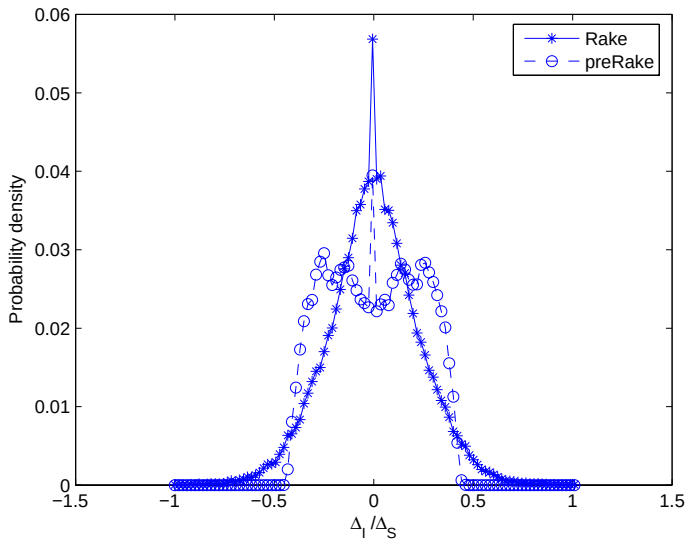

FIGURE 7.4. Distributions of NBI experienced by prerake and rake systems as in-band modulated interferer is present.

Without loss of generality, we assume that the i^{th} transmitted bit is a 1 and derive the conditional BER[2].

7.5.1. MRC Rake Receiver

With perfect path resolution (no IPI) and $b(i) = 1$, Eq. (7.16) can be simplified as

$$\Delta = \Delta_S + \Delta_N + \Delta_I \tag{7.17}$$

---

[2]When input bits have an equal probability to take on the value of 1 and 0, the conditional BER equals to the average BER. This is assumed true in this paper.

where

$$\Delta_S = \sqrt{E_b} \sum_{l=0}^{L_p-1} \alpha_l^2 \tag{7.18a}$$

$$\Delta_N = \sum_{l=0}^{L_p-1} \alpha_l n_l \tag{7.18b}$$

$$\Delta_I = \sum_{l=0}^{L_p-1} \alpha_l I_l \tag{7.18c}$$

Apparently the variance of noise component Δ_N is $\sigma_N^2 = \theta\frac{N_0}{2}$ if we define $\theta = \sum_{l=0}^{L_p-1} \alpha_l^2$. Conditioned on both θ and Δ_I, the BER expression of a binary PAM signal is given by

$$P(\theta, \Delta_I) = \frac{1}{\sqrt{2\pi\sigma_N^2}} \int_{-\infty}^{0} exp\left[-\frac{(\lambda - (\sqrt{E_b}\theta + \Delta_I))^2}{2\sigma_N^2}\right] d\lambda = Q\left(\frac{\sqrt{E_b}\theta + \Delta_I}{\sigma_N}\right) \tag{7.19}$$

The average BER can be calculated by averaging the conditional BER $P(\theta, \Delta_I)$ over the probability density function $f(\theta)$ and $f(\Delta_I)$ (which will be derived later) as

$$P_{rake} = \int_{-\infty}^{\infty} \int_{0}^{\infty} P(\theta, \Delta_I) f(\Delta_I) f(\theta) d\theta d\Delta_I. \tag{7.20}$$

7.5.2. Prerake Receiver

With perfect path resolution (no IPI) and $b(i) = 1$, Eq. (7.15) can be simplified as

$$\Delta' = \Delta'_S + n' + I' \tag{7.21}$$

where

$$\Delta'_S = \sqrt{E_b \sum_{l=0}^{L_p-1} \alpha_l^2} = \sqrt{E_b\theta}. \tag{7.22}$$

The single noise component n' has a simple variance of $\sigma_{n'}^2 = \frac{N_0}{2}$ and the distribution of single NBI component I' can be evaluated via Monte Carlo simulations.

Similar to the case of rake receivers in the previous subsection, conditioned on both θ and I', the BER expression of a binary PAM signal is given by

$$P(\theta, I') = \frac{1}{\sqrt{2\pi\sigma_{n'}^2}} \int_{-\infty}^{0} exp\left[-\frac{(\lambda - (\sqrt{E_b\theta} + I'))^2}{2\sigma_{n'}^2}\right] d\lambda = Q\left(\frac{\sqrt{E_b\theta} + I'}{\sigma_{n'}}\right) \tag{7.23}$$

Again, the average BER can be calculated by averaging the conditional BER $P(\theta, I')$ over the probability density function $f(\theta)$ and $f(I')$ as

$$P_{prerake} = \int_{-\infty}^{\infty}\int_{0}^{\infty} P(\theta, I')f(I')f(\theta)d\theta dI'. \tag{7.24}$$

7.5.3. Distribution of θ

Focusing on the UWB indoor channel model in [19], we suppose for simplicity that all channel paths arrive separately in time, i.e., there is no pulse overlapping. Under this assumption, the received sample gain θ can be simplified to $\theta = \sum_{l=0}^{L_p-1} \alpha_l^2$. Apparently, it is the sum of squared multipath fading coefficients, which are independent lognormal random variables (RVs). To evaluate the pdf of θ, one needs to find the pdf of a sum of independent lognormal RVs. Although an exact closed-form expression does not exist, there are a number of methods to approximate this pdf. We will apply the Wilkinson's method [34] to approximate the desired pdf of θ.

As mentioned in Chapter 2.2, the channel coefficient α_l can be modeled as $\alpha_l = \lambda_l\beta_l,$ where $\lambda_l \in \{1, -1\}$ and $\beta_l = |\alpha_l|$ is a lognormal RV. Let $\beta_l := |\alpha_l| = e^{u_l}$, where u_l is a normal RV obeying $u_l \sim \mathcal{N}(\mu_{u_l}, \sigma_{u_l}^2)$, and $\theta_l := \alpha_l^2 = e^{2u_l}$. The k^{th} moment of the lognormal variable β_l is then given by

$$E\{\beta_l^k\} = e^{k\mu_{u_l} + k^2\sigma_{u_l}^2/2}. \tag{7.25}$$

According to Wilkinson's method, we let $\theta = \sum_{l=0}^{L_p-1} \theta_l$ be modeled as a lognormal RV, which implies that $\theta = e^x$ and $x \sim \mathcal{N}(\mu_x, \sigma_x^2)$ is a normal RV. The two parame-

ters μ_x and σ_x can be obtained by matching the first two moments of θ with the first two moments of $\sum_{l=0}^{L_p-1}\theta_l$. Algebraic manipulations lead to the mean $\mu_x = \ln(E_{L1}^2/\sqrt{E_{L2}})$ and the standard deviation $\sigma_x = \sqrt{\ln(E_{L2}/E_{L1}^2)}$, where the two scalars E_{L1} and E_{L2} are related to μ_{u_l} and $\sigma_{u_l}^2$ by

$$E_{L1} = \sum_{l=0}^{L_p-1} e^{(2\mu_{u_l}+2\sigma_{u_l}^2)} \tag{7.26a}$$

$$E_{L2} = \sum_{l=0}^{L_p-1} e^{(4\mu_{u_l}+8\sigma_{u_l}^2)} + 2\sum_{l=1}^{L_p-1}\sum_{m=0}^{l-1} e^{2(\mu_{u_l}+\mu_{u_m}+\sigma_{u_l}^2+\sigma_{u_m}^2)}. \tag{7.26b}$$

Putting all together, the pdf of θ is approximated as

$$f(\theta) = \frac{1}{\theta\sqrt{2\pi\sigma_x^2}} exp\left[-\frac{(\ln(\theta)-\mu_x)^2}{2\sigma_x^2}\right]. \tag{7.27}$$

In a general case, the pdf $f(\theta)$ should be replaced by the actual channel statistic and can be evaluated via Monte Carlo simulations.

7.5.4. Distribution of Δ_I and I'

Same as in Fig. 7.3 and 7.4, the distribution of Δ_I and I' can be evaluated via Monte Carlo simulations. As being used for BER calculation using the analytical method discussed in the previous two subsections, the simulated distribution can be used, or a curve fitting method could be used to obtain an approximate but smoother distribution.

Because $f(\theta)$, $f(\Delta_I)$, and $f(I')$ are all approximations, and perfect path resolution has been assumed, the BER performance obtained in this section is a loose lower bound.

7.6. Simulation Results and Discussion

In obtaining simulation results, a carrier-modulated, truncated RRC pulse with a roll-off factor 0.25 is applied as the UWB pulse shape $p(t)$. This pulse has a width of $T_p = 1ns$ and a 10dB bandwidth of 2GHz. The system data rate is set as 50 Mbps. We adopt the CM3 channel model [19] with a root-mean-square (RMS) delay spread of $15ns$, an average cluster arrival rate of $0.0667/ns$, and an average path arrival rate of $2/ns$. The cluster decay factor applied is $\Gamma = 14ns$, and the ray decay factor applied is $\gamma = 7.9ns$. The standard deviation of the fading coefficients chosen is 3.4dB and the number of fingers is set to be $L_p = 5$. The receiver has perfect knowledge of the channel coefficients and delays.

Fig. 7.5 shows the simulated error performances of prerake and rake systems in the absence of NBI. For comparison, error performances of these systems in the absence and presence of IPI are provided. All parameters of the channel and transmitted signals are the same for the IPI and non-IPI cases, except that the path arrival rate for the non-IPI case is controlled so that no IPI occurs. It is observed that although IPI degrades the performance, both the prerake and rake systems with MRC combining perform the same. When there is no pulse overlapping, the ZF scheme for prerake system is the same as MRC. In the presence of pulse overlapping, however, the ZF optimization for prerake multipath combining performs worse than the MRC scheme for reasons as explained in Section 7.3. Although ZF for prerake combining does not enhance noise in the receiver, it requires a higher transmit signal energy to overcome IPI.

Error performance in the presence of NBI is shown in Figs. 7.6 and 7.7. NBI signals are generated using the method described in Section 7.4. Fig. 7.6 shows the case when there is no pulse overlapping and the received NBI signal power is 6 dB stronger than the data signal, while in Fig. 7.7 both IPI and NBI are present and the

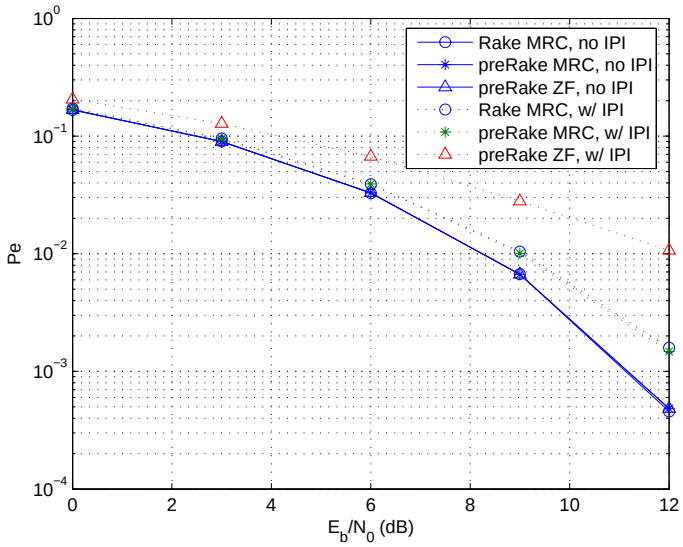

FIGURE 7.5. Simulated BER versus E_b/N_0 curves of the prerake and rake systems with and without IPI, in the absence of NBI.

received NBI signal power is 3 dB stronger. It is observed that in the presence of NBI the prerake scheme always performs better than the conventional rake scheme. This is caused by the different distributions of NBI experienced by the rake and prerake systems as shown in Figs. 7.3 and 7.4.

Generated using the analytical methods developed in Section 7.5, performance curves in the presence of NBI are given in Fig. 7.8 and are compared with the simulated curves. All the system parameters are set as in Fig. 7.6, and the NBI distributions are obtained same as in Figs. 7.3 and 7.4. The comparison shows that the analytical method offers a good approximation to system performance.

Although prerake systems shift the channel estimation to the transmitter side and preprocess the signals there, in a same environment same level of timing offset will be experienced no matter the timing estimation is done at the transmitter side or

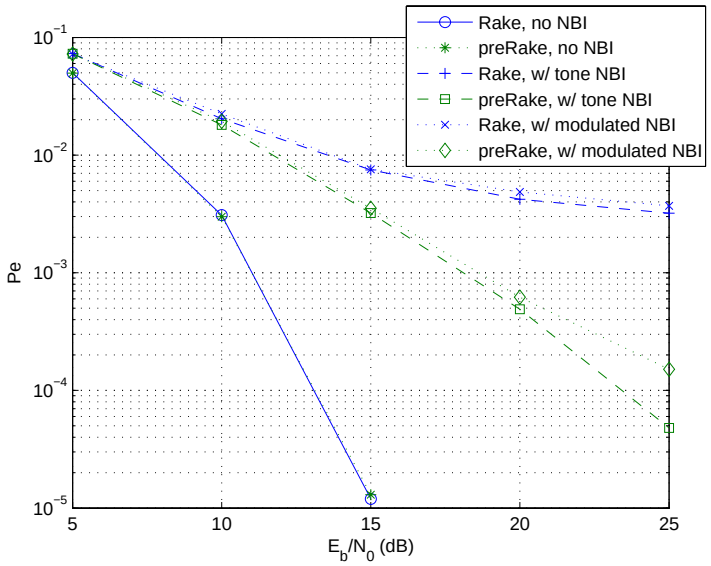

FIGURE 7.6. Simulated BER versus E_b/N_0 curves of the prerake and rake systems with and without NBI, in the absence of IPI.

the receiver side. Fig. 7.9 validates our anticipation. In this simulation, the timing distortion is modelled as Gaussian distributed. A zero mean Gaussian random variable lies between $\pm 3\delta$ in 99.73% cases. By choosing δ to be $0.1T_p$, we model the case where the timing jitter is less than $\pm 0.3T_p$ at most of the time. From the figure, timing jitter does degrade the system performance, but the degradation is same for either rake or prerake system.

7.7. Conclusion

In this chapter, optimization of prerake multipath combining schemes has been discussed for pulsed UWB in the presence of IPI caused by pulse overlapping. MRC is still proved to be the optimum linear multipath combining scheme for prerake systems in the sense of maximum received SNR when the system is distorted by AWGN and

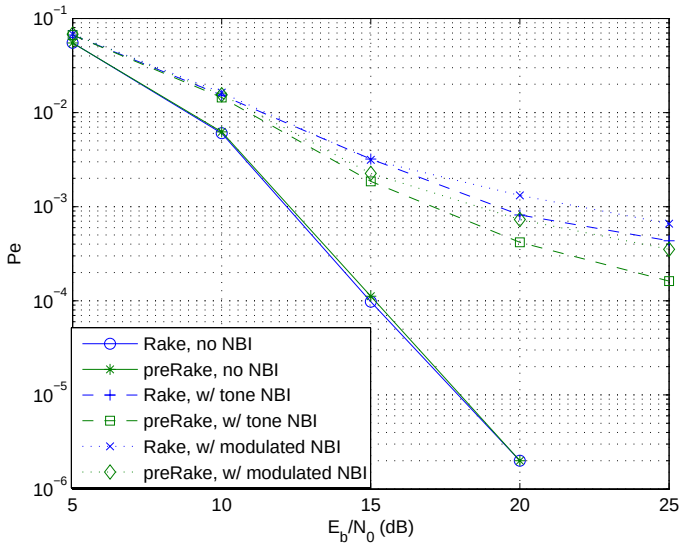

FIGURE 7.7. Simulated BER versus E_b/N_0 curves of the prerake and rake systems with and without NBI, in the presence of IPI.

IPI. We have also assessed the receiver behavior and performance of both the prerake and the traditional rake schemes in the presence of NBI. The prerake scheme has been found to outperform the rake scheme when NBI is present. In the absence of NBI, however, both the rake and prerake schemes with the same set of combining weights have identical performances.

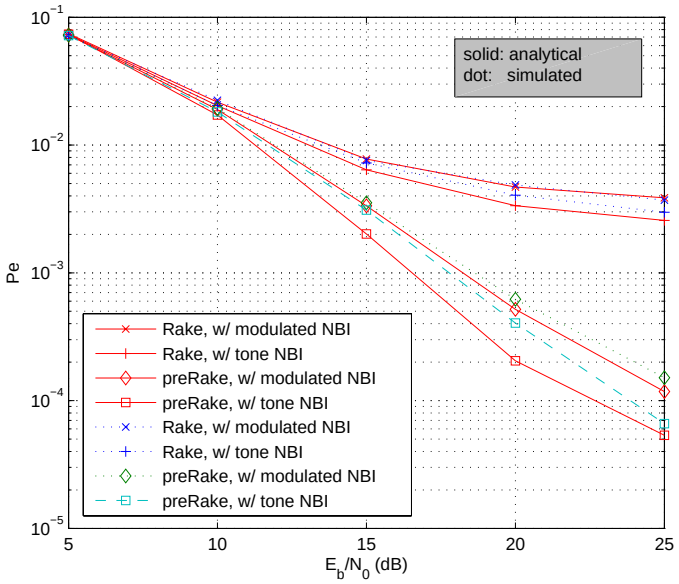

FIGURE 7.8. Analytical and simulated BER performances of the prerake and rake systems in the presence of NBI, but no IPI.

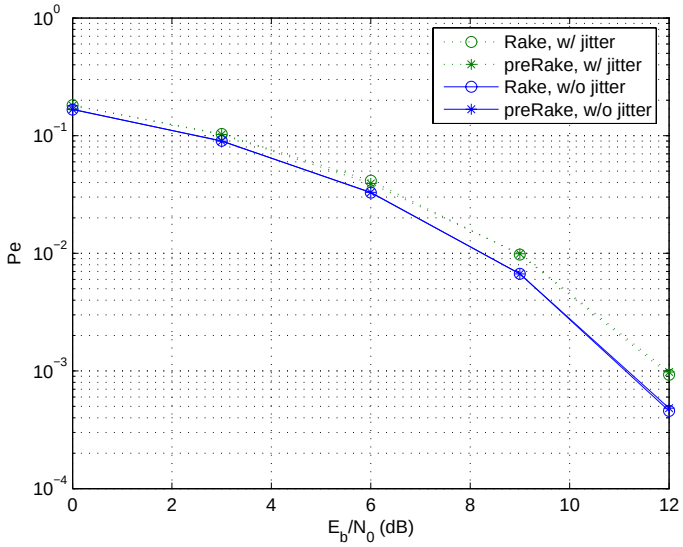

FIGURE 7.9. BER performances of the prerake and rake systems in the presence of timing jitter.

8. CONCLUSIONS

The UWB system designs involve a lot of different aspects from radio frequency circuit designs to digital signal processing, from modulation/demodulation to channel estimation to interference suppression, from the top overview on transceiver structures down to detailed analog/digital components. This thesis cannot cover all of them, but only a small part that was ever investigated during the author's research.

The UWB research has seen a lot of attention and progress, but still faces some challenges as we have discussed throughout. In this thesis we tried to contribute on some topics. As most of published UWB research to date has focused on single-band systems, in Chapter 3 a frequency-hopped multi-band system was proved to provide higher throughput and ISI mitigation. Although all existing research has assumed perfect multipath resolution, i.e. the received adjacent pulses are separated in time, pulse overlapping is common in realistic channel environment and may seriously degrade the system performance. In Chapter 4, optimum linear equalization scheme has been investigated for RAKE receivers experiencing IPI in stringent multipath fading scenarios.

As an effort to avoid the complexity and difficulty in coherent RAKE receiver implementations, innovative decision-directed autocorrelation (DDA) receiver structures was developed in Chapter 5 for effective multipath energy capture at low complexity, while minimizing the energy waste and performance degradation caused by the reference pilots in conventional transmit-reference (TR) receiver structures.

Another option to balance between cost and performance is to allow difference types of systems in a same heterogeneous network. In Chapter 6, we satisfied this goal by an innovative design of modulation method which allows both coherent RAKE receivers and TR receivers to be compatible in a same system. Different users can have the flexibility on choosing devices of different receiver types based on their specific

QoS needs and financial capability. Neither type of receivers need to sacrifice their performance. In addition, coherent RAKE receivers can show great advantages when combined further with forward error correction (FEC) and iterative decoding methods.

Attractive to infrastructure type of TDD system with fixed access points, pre-rake diversity combining scheme was proposed in Chapter 7 to shift signal processing burden from receiver to transmitter side. We are the first to investigate it in a realistic channel environment with IPI and NBI.

BIBLIOGRAPHY

[1] M. Z. Win and R. A. Scholtz, "Impulse radio: how it works," *IEEE Communications Letters*, vol. 2, pp. 36–38, Feb. 1998.

[2] M. G. diBenedetto, T. Kaiser, A. F. Molisch, I. Oppermann, C. Politano, and D. Porcino (eds.), *UWB communications systems: a comprehensive overview*, EURASIP publishing, 2005.

[3] R. C. Qiu, H. Liu, and X. Shen, "Ultra-wideband for multiple access communications," *IEEE Communications Magazine*, vol. 43, pp. 80-87, Feb. 2005.

[4] L. Yang and G. B. Giannakis, "Ultra-wideband communications - An idea whose time has come," *IEEE Signal Processing Magazine*, vol. 21, pp. 26–54, Nov. 2004.

[5] W. Zhuang, X. Shen, and Q. Bi, "Ultra-wideband wireless communications," *Wireless communications and mobile computing*, vol. 3, pp. 663–685, 2003.

[6] J. R. Foerster, E. Green, S. Somayazulu, and D. Leeper, "Ultra-Wideband Technology for Short- or Medium-Range Wireless Communications," *Intel Technology Journal, 2001Q2*.

[7] Assessment of Ultra-Wideband (UWB) Technology, OSD/DARPA, *Ultra-wideband Radar Review Panel*, R-6280, July 1990.

[8] FCC Notice of Proposed Rule Making, "Revision of part 15 of the commission's rules regarding ultra-wideband transmission systems," *ET-Docket 98-153*, 1998.

[9] FCC First Report and Order, "In the matter of revision of part 15 of the commission's rules regarding ultra-wideband transmission systems," *FCC 02-48*, Apr. 2002.

[10] S. Gezici, Z. Tian, G. B. Giannakis, H. Kobayashi, A. F. Molisch, H. V. Poor, and Z. Sahinoglu, "Localization via ultra-wideband radios: a look at positioning aspects for future sensor networks," *IEEE Signal Processing Magazine*, vol. 22, pp. 70–84, July 2005.

[11] S. Zhao, H. Liu, and S. Mo, "Performance of a multi-band ultra-wideband system over indoor wireless channels," *Proc. of IEEE CCNC'04*, Jan. 2004.

[12] S. Zhao, H. Liu, and Z. Tian, "A decision-feedback authcorrelation receiver for pulsed ultra-wideband systems," *Proc. of IEEE 2004 Radio and Wireless Conference (Rawcon'04)*, pp. 251-254, Sep. 2004.

[13] S. Zhao, H. Liu, and Z. Tian, "Decision directed autocorrelation receivers for pulsed ultra-wideband systems," to appear in *IEEE Trans. on Wireless Comm.*

[14] S. Zhao and H. Liu, “On the optimum linear receiver for impulse radio system in the presence of pulse overlapping,” *IEEE Communication Letters*, vol. 9, no. 3, Mar. 2005.

[15] P. Orlik, S. Zhao, and A. Molisch, “A hybrid UWB modulation design compatible for both coherent and transmit-reference receivers,” *Proc. of IEEE ICC’06*, June 2006.

[16] S. Zhao, P. Orlik, A. F. Molisch, H. Liu, and J. Zhang, “Hybrid Ultrawideband Modulations Compatible for Both Coherent and Transmit-Reference Receivers,” to appear in *IEEE Trans. on Wireless Comm.*

[17] S. Zhao and H. Liu, “Prerake diversity combining for pulsed UWB systems considering realistic channels with pulse overlapping and narrow-band interference,” *Proc. of IEEE Globecom’05*, Nov. 2005.

[18] S. Zhao and H. Liu, “Transmitter-Side Multipath Preprocessing for Pulsed UWB Systems Considering Pulse Overlapping and Narrow-Band Interference,” submitted to *IEEE Trans. on Vehi. Tech.*

[19] A. F. Molisch, J. R. Foerster, and M. Pendergrass, “Channel models for ultrawideband personal area networks,” *IEEE Wireless Communications*, vol. 10, No. 6, pp. 14–21, Dec. 2003.

[20] A. F. Molisch, K. Balakrishnan, C.-C. Chong, S. Emami, A. Fort, J. Karedal, J. Kunisch, H. Schantz, U. Schuster, and K. Siwiak, “IEEE 802.15.4a channel model - final report,” *Document IEEE 802.15-04-0662-02-004a*, 2005.

[21] A. F. Molisch, K. Balakrishnan, C. C. Chong, D. Cassioli, S. Emami, A. Fort, J. Karedal, J. Kunisch, H. Schantz, and K. Siwiak, “A comprehensive model for ultrawideband propagation channels,” submitted to *IEEE Trans. Antennas Prop.*, 2006.

[22] H. Hasmemi, “Inpulse response modeling of indoor radio propagation channels,” *IEEE Journal on Selected Areas in Communications*, vol. 11, pp. 967-978, Sept. 1993.

[23] H. Hashemi, “The indoor radio propagation channel,” *Proceedings of the IEEE*, vol. 81, No. 7, pp. 943-968, July 1993.

[24] J. R. Foerster, V. Somayzulu, and S. Roy, “A multi-banded system architecture for ultra-wideband communications,” *Proc. of 2003 IEEE Military Communications Conference*, vol. 2, pp. 903–908, Oct. 2003.

[25] A. Batra, J. Balakrishnan, G. R. Aiello, J. R. Foerster, A. Dabak, “Design of a multiband OFDM system for realistic UWB channel environments,” *IEEE Trans. on Microwave Theory and Techniques*, vol. 52, no. 9, pp. 2123–2138, Sept. 2004.

[26] J. Balakrishnan, A. Batra, and A. Dabak, “A multi-band OFDM system for UWB communication,” *Proc. of 2003 IEEE Conference on Ultra-wideband Systems and Technologies*, Nov. 2003.

[27] M. Z. Win and R. A. Scholtz, “On the energy capture of ultrawide bandwidth signals in dense multipath environments,” *IEEE Communications Letters*, vol. 2, no. 9, pp. 245–247, Sep. 1998.

[28] S. Gaur and A. Annamalai, “Improving the range of UWB transmission using RAKE receivers,” *Proc. of the 53rd IEEE VTC*, vol. 1, pp. 597–601, Oct. 2003.

[29] D. Cassioli, M. Z. Win, A. F. Molisch, and F. Vatelaro, “Performance of selective Rake reception in a realistic UWB channel,” *Proc. ICC 2002*, pp. 763–767, 2002.

[30] [V. S. Somayazulu, “Multiple access performance in UWB systems using time hopping vs. direct sequence spreading,” *IEEE WCNC 2002*.

[31] J. R. Foerster, “The performance of a direct-sequence spread ultra-wideband system in the presence of multipath, narrowband interference and multiuser interference,” *Proc. of 2002 IEEE Conference on Ultra-Wideband Systems and Technologies*, pp. 87–91, 2002.

[32] J. R. Foerster, “The effects of multipath interference on the performance of UWB systems in an indoor wireless channel,” *Proc. of the 53rd IEEE Vehicular Technology Conference, VTC 2001 Spring*, vol. 2, pp. 1176–1180, 2001.

[33] M. Patzold, F. Laue, and U. Killat “A frequency hopping Rayleigh fading channel simulator with given correlation properties,” *Proc. of the 1997 IEEE International Workshop on Intelligent Signal Processing and Communication System, ISPACS’97*, pp. S811–S816, Malaysia, 1997.

[34] N. C. Beaulieu, A. A. Abu-Dayya, and P. J. Mclane, “Estimating the distribution of a sum of independent lognormal random variable,” *IEEE Trans. on Communications*, vol. 43, pp. 2869-2873, Dec. 1995.

[35] M. Hamalainen, V. Hovinen, R. Tesi, J. H. J. Iinatti, M. Latva-aho, “On the UWB system coexistence with GSM900, UMTS/WCDMA, and GPS,” *IEEE Journal on Selected Areas in Communications*, vol. 20, No. 9, pp. 1712–1721, Dec. 2002.

[36] A. Klein, G. K. Kaleh, and P. W. Baier, “Zero forcing and minimum mean-square-error equalization for multiuser detection in code-division multiple-access chan-

nels," *IEEE Transactions on Vehicular Technology*, vol. 45, No. 2, pp. 276-287, May 1996.

[37] D. A. Gore, R. W., Heath Jr., and A. J. Paulraj, "Transmit selection in Spatial multiplexing systems," *IEEE Communications Letters*, vol. 6, pp. 491-493, Nov. 2002.

[38] R. T. Hoctor and H. W. Tomlinson, "An overview of delay-hopped, transmitted-reference RF communications," in *Technical Information Series*, G.E. Research and Development Center, pp. 1-29, Jan. 2002.

[39] K. Witrisal, G. Leus, M. Pausini, and C. Krall, "Equivalent system model and equalization of differential impulse radio UWB systems," *IEEE J. Selected Areas Comm.*, vol. 23, pp. 1851–1862, 2005.

[40] T. Q. S. Quek and M. Z. Win, "Analysis of UWB transmitted-reference communication systems in dense multipath channels," *IEEE J. Selected Areas Comm.*, vol. 23, pp. 1863–1874, 2005.

[41] J. D. Choi and W. E. Stark, "Performance of ultra-wideband communications with suboptimal receiver in multipath channels," *IEEE Journal on Selected Areas in Communications*, vol. 20, No. 9, pp. 1754-1766, Dec. 2002.

[42] S. Gezici, F. Tufvesson, and A. F. Molisch, "On the performance of transmitted-reference impulse radio," *Proc. of IEEE Globecom'04*, vol. 5, pp. 2874-2879, Nov. 2004.

[43] L. Yang and G. B. Giannakis, "Optimal pilot waveform assisted modulation for ultra-wideband communications," *IEEE Transactions on Wireless Communications*, vol.3, no. 4, pp. 1236-1249, July 2004.

[44] H. Zhang and D. L. Goeckel, "Generalized transmitted-reference UWB systems," *Proc. of IEEE UWBST'03*, pp. 147–151, Nov. 2003.

[45] A. Trindade, Q. H. Dang, and A. *van der* Veen, "Signal processing model for a transmit-reference UWB wireless communication system," *Proc. of IEEE UWBST'03*, pp. 270–274, Nov. 2003.

[46] G. Leus, and A. *van der* Veen, "Noise suppression in UWB transmitted reference systems," *Proc. Signal Processing Advances in Wireless Communications* (SPAWC'04), Lisbon, Portugal, July 2004.

[47] Y.-L. Chao and R. Scholtz, "Optimal and suboptimal receivers for ultra-wideband transmitted reference systems," *Proc. of IEEE Glboecom'03*, pp. 759–763, Dec. 2003.

[48] G. Durisi and S. Benedetto, "Performance of coherent and non-coherent receivers for UWB communications," *Proc. of IEEE ICC'04*, pp. 3429–3433, June 2004.

[49] L. Yang and G. B. Giannakis, "A general model and SINR analysis of low duty-cycle UWB access through multipath with narrowband interference and Rake reception," *IEEE Trans. Wireless Comm.*, vol. 4, pp. 1818–1833, July 2005.

[50] M. Z. Win and R. A. Scholtz, "Ultra-wide bandwidth time-hopping spread-spectrum impulse radio for wireless multiple-access communications," *IEEE Trans. Comm.*, vol. 48, pp. 679–691, Apr. 2000.

[51] Y. P. Nakache and A. F. Molisch, "Spectral shape of UWB signals : influence of modulation format, multiple access scheme and pulse shape," *Proc. VTC 2003 spring*, pp. 2510–2514, 2003.

[52] L. R. Bahl, J. Cocke, F. Jelinek, J. Raviv, "Optimal decoding of linear codes for minimizing symbol error rate," *IEEE Trans. On Info. Theory*, vol. 20, no. 2, pp. 284 – 287, Mar. 1974.

[53] S. Benedetto, D. Divsalar, G. Montorsi, and F. Pollara, "Serial concatenation of interleaved codes: performance analysis, design, and iterative decoding," *IEEE Trans. on Info. Theory*, vol. 44, no. 3, pp. 909–926, May 1998.

[54] C. Berrou and A. Glavieux, "Near optimum error correcting coding and decoding: Turbo-codes," *IEEE Trans. Commun.*, vol. 44, pp. 1261–1271, Oct. 1996.

[55] Stephan ten Brink, "Convergence behavior of iteratively decoded parallel concatenated codes," *IEEE Trans. on Comm.*, vol. 49, no. 10, pp. 1727–1737, Oct. 2001.

[56] Stephan ten Brink, "Design of serially concatenated codes based on iterative decoding convergence," *Proc. Int. Symp. on Turbo Codes and Related Topics*, Brest, France, pp. 319-322, Sep. 2000.

[57] R. A. Scholtz, P. V. Kumar, and C. J. Corrada-Bravo, "Signal design for ultra-wideband radio," *Proc. of Sequences and Their Applications (SETA'01)*, 2001.

[58] J. H. Park, "On binary DPSK detection," *IEEE Trans. on Communications*, vol. COM-26, pp. 484-486, Apr. 1978.

[59] R. Esmailzadeh, E. Sourour, and M. Nakagawa, "Prerake diversity combining in time-division duplex CDMA mobile communications," *IEEE Transactions on Vehicular Technology*, vol. 48, no. 3, pp. 795-801, May 1999.

[60] K. Usuda, H. Zhang, and M. Nakagawa, "Pre-Rake performance for pulse based UWB system in a standardized UWB short-range channel," *Proc. of IEEE WCNC'04*, vol. 2, Mar. 2004.

[61] T. Strohmer, M. Emami, J. Hansen, G. Papanicolaou, A. J. Paulraj, "Application of time-reversal with MMSE equalizer to UWB communications," *Proc. of IEEE GLOBECOM '04*, Nov. 2004.

[62] Z. Xu, B. Sadler, and J. Tang, "Data detection for UWB transmitted reference systems with inter-pulse interference," in *Proc. IEEE ICASSP'05*, Mar. 2005.

[63] X. Chu and R. Murch, "Performance analysis of DS-MA impulse radio communications incorporating channel-induced pulse overlap," to appear in *IEEE Trans. on Wireless Communications*, 2006.

[64] L. Zhao and A. M. Haimovich, "Performance of ultra-wideband communications in the presence of interference," *IEEE Journal on Selected Areas in Communications*, vol. 20, no. 9, pp. 1684–1691, Dec. 2002.

[65] J. R. Foerster, "The performance of a direct-sequence spread ultra-wideband system in the presence of multipath, narrowband interference and multiuser interference," *Proc. of IEEE UWBST'02*, pp. 87–91, 2002.

[66] IEEE 802.15.3a Technical Editors, "IEEE P802.15.3a alternative PHY selection criteria," *Document IEEE P802.15-03/031r5*, Dec. 2002.

[67] IEEE 802.15.4a Technical Editors, "IEEE P802.15.4a alternative PHY selection criteria," *Document IEEE P802.15-04-0232-16-004a*, Nov. 2004.

[68] A. F. Molisch, *Wireless Communications*, New Jersey: Wiley-IEEE Press, 2005.

[69] R. V. Nee, R. Prasad, *OFDM for Wireless Multimedia Communications*, Norwood, MA: Artech House Publishers, 2000.

[70] S. Haykin, *Adaptive Filter Theory*, New Jersey: Prentice Hall, 1996.

[71] M. K. Simon, S. M. Hinedi, and W. C. Lindsey, *Digital communication techniques*. New Jersey: Prentice-Hall, 1995.

[72] J. G. Proakis, *Digital communications*. New York, NY: McGraw-Hill, 4th ed., 2001.

[73] T. S. Rappaport, *Wireless communications: principles & practice*. New Jersey: Prentice Hall, 1996.